ION BEAM IRRADIATION INDUCED FABRICATION OF SILICON PHOTONICS

–FROM 2D TO 3D

LIANG HAIDONG

(B.Sc.), Nanjing University

A THESIS SUBMITTED

FOR THE DEGREE OF DOCTOR OF PHILOSOPHY

DEPARTMENT OF PHYSICS,

NATIONAL UNIVERSITY OF SINGAPORE

2013

DECLARATION

I hereby declare that the thesis is my original work and it has been written by me in its entirety.

I have duly acknowledged all the sources of the information which have been used in the thesis.

This thesis has also not been submitted for any degree in any university previously.

_____

Liang Haidong
5 August 2013

Acknowledgements

First and foremost I would like to express my sincere gratitude to my supervisor, Prof Mark B. H. Breese. I appreciate all his contributions of time, ideas, and funding during my Ph. D period. His advices are always valuable and meaningful. His passion for research and ability of excellent time arrangement are something I look up to. Despite his constant busy schedules, he always finds time for every one of the seven students under his supervision, never turning any away whenever any one of us has questions or need his help for whatever reason. It has been a fortune and honor to have such a good supervisor. So here, I also want to thank Yuanjun, who recommended Mark to me at the beginning of my PhD, and he is also the one who picked me up at the airport when I first came to Singapore.

Some senior CIBA members also helped me a lot, especially Isaac. Most of my experimental skills were taught by Isaac. He is smart and also hardworking. He is always very kind to us new students and willing to help us. I have learned a lot beyond experimental skills from him. Great thanks to Isaac!

Thanks to Aky, Eejin and Shao who taught me a lot at the start of my PhD. Thanks to TK, Armin, Chammika for their help on the accelerator operation. Thanks to Sara for her help in the experiments. Thanks to Jianfeng with his help in the UV lithography in IMRE. Thanks to Sudheer for his help in the optical simulations and characterizations. Thanks to Eric for his help in RIE in IMRE.

Thanks to all CIBA members. The professors are kind and encouraging to us students. All the students are kind to each other. We usually had meals together, gym and jogging together. CIBA is like another big warm family to me.

Thanks to my friends, friends I met in NJU, especially guys from Room 408, and friends I met in my high school. Friends give me nice and

great vacations and make me never alone during my PhD life and to my whole life. I am really grateful and proud to have you friends. I love you guys.

最后，我要感谢我的家人，我的爸爸妈妈，弟弟以及他的小家庭，我的三叔一家，还有很多我的兄弟姐妹，以及他们的家庭。感谢他们对我的鼓励和支持。一个和睦美好的家庭永远给我力量去笑着面对一切困难。

Table of Contents

Abstract ..... **iii**

List of Figures ..... **v**

Chapter 1 Introduction **1**

1.1 Photonics and Si photonics 2

1.2 Different devices in Si photonic structures 3

1.2.1 Waveguides 3

1.2.2 Couplers and splitters 4

1.2.3 Resonators 4

1.3 Fabrication of Si photonic devices 5

1.4 Objectives 8

Chapter 2 Background **11**

2.1 Introducing porous silicon 11

2.2 Ion irradiation induced Si machining 13

2.3 Centre for ion beam applications (CIBA) 17

2.3.1 Proton Beam Writing (PBW) 19

2.3.2 Large area irradiation 21

Chapter 3 High and Low Energy Ion Irradiation Effects on Etching **25**

3.1 Anodization setups 25

3.2 PSi formation rate 27

3.3 Effect of high energy ion beam irradiation 28

3.4 Effect of low energy ion beam irradiation 32

3.5 Difference between high and low energy ion beam irradiation 36

Chapter 4 Optical Micro-resonators **39**

4.1 Introduction to optical microresonators 39

4.2 Fabrication of Microdisk resonators 41

4.3 Integrated waveguide-resonators 47

4.3.1 Achieving small gap 47

4.3.2 Lithography 53

4.3.3 Results 56

4.3.4 E-beam patterns 59
Chapter 5 Flexible Polarization Y-shape Splitters 63
5.1 Introduction 63
5.2 Y-shape splitter simulations 64
5.2.1 TE and TM oscillations 66
5.2.2 Different wavelengths 67
5.2.3 Different waveguide width and arm angles 69
5.2.4 Summary 72
5.3 Fabrication of Y-shape splitter 72
5.4 Characterization of Y-shape splitter 75
5.4.1 Characterization of Y-shape splitters with short arms 76
5.4.2 Characterization of Y-shape splitters with long arms 79
5.5 3D beam splitters 81
Chapter 6 Vertical Coupling Photonics 87
6.1 Introduction 87
6.2 Vertical coupling waveguide-resonators 88
6.2.1 Development of the fabrication process with a thin device layer 90
6.2.2 Details of the fabrication process with an epitaxially grown device layer 95
6.3 Vertical coupling waveguide-to-waveguide 100
6.3.1 First attempt 101
6.3.2 Simulations 105
6.3.3 Further optimization and simulations 108
6.4 Summary 114
Chapter 7 Conclusion and Discussions 115
References 118

Abstract

Silicon photonics is very important in future computer technology as it is able to integrate electronic and optical components on the same silicon chip, and to perform ultrafast data transfer within microchips. At present, most people are using SOI platforms to make 2D photonic structures. However, SOI is much more expensive compared to bulk silicon, and it is limited to 2D structures. In this thesis, a newly developed micro and nano silicon machining process via ion beam irradiation will be applied to fabrications of silicon photonics in 2D and 3D on bulk silicon and SOI platforms.

The ion beam irradiation induced silicon machining process is further developed. Different fluences of high (MeV) and low (100 keV) energy ion beams were irradiated on p-type silicon wafers. After etching, it was found that while high energy ion beam irradiation would reduce the etching rate, low energy ion beam irradiation would give out an undercut limit during electrochemical etching.

Fabrications of microdisk and microring resonators with or without waveguides integrated and Y-shape beam splitters, using a direct proton beam writing or a large area irradiation with a photoresist mask on top, followed by a single electrochemical etching step on bulk silicon wafers were demonstrated. Resonances were measured in microdisk resonators. Efficient integrated waveguide-and-resonators were not successful because of the gap limitation via this process. Y-shape splitters could give out tunable polarized outputs based on multimode-interference. These may provide an easier and cheaper way to obtain 2D silicon photonic devices on bulk silicon. Furthermore, with an additional irradiation step with a different energy to 2D Y-shape splitters, a 3D beam splitter was also achieved on bulk silicon. This extends the scope to 3D silicon photonic structures on bulk silicon.

Applying this process to SOI platforms, vertically coupled waveguides and waveguide-resonators were fabricated by a normally used RIE combined with an aligned ion beam irradiation followed by electrochemical etching on SOI wafers. Optical characterizations showed a typical coupling efficiency of 26% in vertical coupled waveguides. This coupling efficiency is similar with a typically used grating coupler. Thus it could be an alternative of the grating couplers, which would allow side coupling light from the optical fiber to make the system more stable. Simulations show that the coupling efficiency depends on the gap between the two layer waveguides, the thicknesses, widths of the waveguides, and the wavelength and polarization of the incident light. Theoretically, the maximum coupling efficiency could be up to over 90% which is much higher than 26% achieved at present. The experimental coupling efficiency is now mainly limited by the accuracy of UV lithography.

In conclusion, this study may have provided an easier and cheaper machining process to obtain 2D and 3D silicon photonic structures on bulk silicon. The process can also be applied to SOI platforms, and it is compatible with normally used 2D photonic fabrications and able to help achieving vertically coupled structures.

List of Figures

Fig 1. 1 *(a) Total internal reflection at two interfaces in a planar waveguide, (b) Definition of a rib waveguide in terms of some normalising parameters.*.....3

Fig 1. 2 *SIMOX process, (a) oxygen implantation, (b) a rich oxygen layer formed, (c) high temperature annealing, (d) SOI wafer formed.*.....6

Fig 1. 3 *A simplified schematic of Smart Cut process, (a) surface thermal oxidation, (b) H implantation, (c) flip and bond to handle wafer, (d) bubble formation, (e) break, (f) polishing.*.....7

Fig 2. 1 *Chemical processes of PSi formation. From [57]*.....13

Fig 2. 2 *SRIM plots showing the defect density distribution in silicon by 10,000 (a) 2MeV helium ions and (b) 2 MeV protons.*.....14

Fig 2. 3 *(a) Plot showing the relationship of between resistivity and the amount of ion irradiation for highly doped (0.02 Ω.cm) and moderately doped (0.1-1 Ω.cm) silicon samples. (b) I-V plot for the anodization process. With increased irradiation fluence, the whole I-V curve will shift to the right, implying that with constant bias applied, the current owing through the irradiated regions is lower than the current owing through unirradiated regions. From [60]*.....15

Fig 2. 4 *MEDICI plots of current density J across a region containing a single irradiated line (gray area) for different fluences. The curves are normalized to the same J in the background for easier comparison. From [62]*.....16

Fig 2. 5 *(Left) Top down schematic diagram of the ion beam setup in CIBA; (Right) Actual image of the facilities. (1) the accelerator, (2) 90 ˚ magnet, (3) switching magnet, (4) end-station chambers*.....17

Fig 2. 6 *Top down schematic of 2 MeV proton beam selection by 90 ˚ magnet*.....18

Fig 2. 7 *Cross-sectional schematic of a quadrupole lens. The magnetic poles are created electromagnetically by coils. Red arrows indicates the direction of current flow in the coils to result in the desired magnetic polarity at the ends.....20*

Fig 2. 8 *Schematic of the ion beam defocusing for large area irradiation.....22*

Fig 3. 1 *Schematic of etching setup.....25*

Fig 3. 2 *Prepared silicon sample for anodization.....26*

Fig 3. 3 *Cross-section images of irradiated areas (1 MeV protons on medium resistivity wafer) with 6 different fluences ($1\times10^{16}/cm^2$ to $5\times10^{13}/cm^2$ as marked) in (a-f). (d) the white dotted line is the original surface of the wafer, h is the etched height of the irradiated areas, H is the height of the whole defect region.....29*

Fig 3. 4 *Defect distribution created by 1MeV protons.....30*

Fig 3. 5 *Etched percentage at the defect regions of low resistivity wafers irradiated by different energy protons (1, 1.5, 2 MeV) with different fluences. 30*

Fig 3. 6 *Etched percentage at the defect regions of low and medium resistivity wafers irradiated by 1.5 MeV protons with different fluences. 31*

Fig 3. 7 *Defect distributions created by (a) high energy 2 MeV protons, with a long trajectory (>50 µm), low density from the surface, high defect at the end of range, and (b) low energy 50 keV protons, only distributed within a shallow depth close to the surface.....32*

Fig 3. 8 *Etching behavior after irradiation by 100 keV protons on a medium resistivity wafer: (a) showing a undercut lateral limit of ~20µm at fluence of 1×1016/cm2, the central part of the disk is partially etched through; (b) normal undercutting at fluence of 2×1016/cm2, (c) the central part is totally etched through, and the disk is lift off, at fluence of 2×1015/cm2.....34*

Fig 3. 9 *Cross sectional SEM image showing the undercutting limit and etching through the irradiated region, a wide line irradiated with 1×1014/cm2 100 keV H2+, which has a undercutting limit of ~10 µm. 35*

Fig 3. 10 *A schematic showing the etching behavior of (a) High energy ion irradiation, a gradual process with the irradiated layer partially etched from the top; and (b) Low energy ion irradiation, an abrupt process with some etching through points at the irradiated area. The red arrow shows the current flow. 37*

Fig 4. 1 *SEM images of the microdisk fabricated via ion irradiation for the first time, (a) a tilted overview, (b) side view.* 42

Fig 4. 2 *SEM images of the microdisk fabricated by lower energy ion beam and higher irradiation fluence.* 43

Fig 4. 3 *Microdisk smoothened after thermal oxidation and annealing.* 44
Fig 4. 4 *Schematic of the measurement setup, the tapered optical fiber is positioned on two stages S1 and S2, the sample is also on a stage S3. The stages can move freely with a 20-nm-resolution, so to tune the coupling between the fiber and the disks.* 45

Fig 4. 5 *Top view image of the light coupling, (a) under coupling, (b) critical coupling.* 45

Fig 4. 6 *Transmission spectrum of the silicon microdisk.* 46

Fig 4. 7 *Left: SEM images of proton irradiated lines in a 3 Ω·cm wafer, all 5 µm wide, separated by gaps of (a) 10 µm, (b) 5 µm, (c) 2.5 µm, and (d) 1.5 µm. Fluence of 1015/cm2, etched at J =100 mA/cm2 for 5 min, then PSi removed; and right: Schematic of the E-field lines around two irradiated lines with decreasing gap size. Note the behavior of the dotted E-field line, which moves from inside to outside the gap with decreasing gap size. From [110]* 47

Fig 4. 8 *Schematic of the forced current approach to achieving high resolution structures, the black areas are irradiated defect regions, the light blue lines are the E-field lines.* 48

Fig 4. 9 *Schematic of the forced current fabrication process, (a) UV lithography for a small area covered with photoresist (PR), (b) large area irradiation, (c) surrounding defect region formed, (d) proton beam writing to write the fine lines with small gaps, (e) final etching and annealing step.* 49

Fig 4. 10 *SEMs of the forced current result, surrounding large area: 1×1016 protons/cm2,1 MeV protons, square area: 1×1015 protons/cm2, 500 keV protons, proton beam writing with 0.5 µm line width and 1 µm and 2 µm gaps, (a) overview, (b,c,d) fine views.* 50

Fig 4. 11 *Schematic and SEM results of (a,b) the partially force current, (c,d) lines without force current.* 51

Fig 4. 12 *SRIM results showing the ion beam lateral scattering in silicon, (a) 1MeV protons with huge lateral scattering, (b) 50 keV protons with small scattering.* 52

Fig 4. 13 *Sub-micron gap achieved with low energy ion beam irradiation.* 52

Fig 4. 14 *Microscope image of the mask. 53*

Fig 4. 15 *SEM images of the lines on the photoresist, (a) partially developed thin lines, (b,c) fully developed lines, but not smooth, (d) fully developed and smooth wide line. 55*

Fig 4. 16 *Optimized lithography process to improve the conditions of side walls. 55*
Fig 4. 17 *SEMs of the coupled waveguides-and-microdisk resonators, top inset is the fine view of the coupling region, bottom inset is the cross section of the waveguide. 56*

Fig 4. 18 *SEMs of the coupled waveguides-and-microdisk resonators, insets show a fine view of the coupling regions, (a) with one of the gaps not fully etched (the right gap in the inset), (b) both gaps fully etched. 57*

Fig 4. 19 *Tilted view of the structure and the waveguide cross section in the inset... 58*

Fig 4. 20 *(a) Integrated waveguides and micro-ring, the radius of the inner circle support r=20 µm, the outer radius of the ring R=40 µm, (b) support of the waveguide. 59*

Fig 4. 21 *Integrated waveguides and microdisk patterned by e-beam lithography.... 60*

Fig 4. 22 *Integrated waveguides and microdisk patterned by e-beam lithography, (a) waveguide and microdisk totally connected (in the red square), (b) the gap is not fully etched. 61*

Fig 4. 23 *Gaps in high magnification, (a) gap fully etched, (b) not fully etched. 61*

Fig 5. 1 *Simulation results of a Y-shape splitter with width 5µm, arm angle 5 ˚, the incident light is 1.55µm wavelength, TE mode: left shows a schematic of the splitter and color map of the power distribution; the center is the monitor value along the right arm; the right is a color scale bar of the power strength. 66*

Fig 5. 2 *Simulation results of a Y-shape splitter with width 5µm, arm angle 5 ˚, the incident light is 1.55µm wavelength, red for TE mode, blue for TM mode. 67*

Fig 5. 3 *Simulation results of a Y-shape splitter with width 5µm, arm angle 5 ˚, length 930µm, the incident light is TE mode, (a) 1.55µm wavelength gives a maximum output; (b) 1.65µm wavelength gives a minimum output. 67*

Fig 5. 4 *Simulation results of a Y-shape splitter with width 5µm, arm angle 5 ˚, within a length of 100-700 µm, the incident light is TE mode, with a series of wavelengths: 1.54, 1.542, 1.544, 1.55, 1.65 µm. The splitting starts at Z=100 µm. 68*

Fig 5. 5 *Simulation results of a Y-shape splitter with the same settings as in last figure, showing Z axis from 3300-4000 µm.....69*

Fig 5. 6 *Simulation results of a Y-shape splitter with width 5 µm in blue, 5.15 µm in red, arm angle 5˚, the incident light is 1.55µm wavelength, TE mode. 70*

Fig 5. 7 *Simulation results of a Y-shape splitter with width 2µm, arm angle 5˚, the incident light is 1.55µm wavelength, TE mode.....71*

Fig 5. 8 *Simulation results of a Y-shape splitter with width 1 µm, arm angle 20˚, the incident light is 1.55µm wavelength, TE mode in red, TM in blue.....71*

Fig 5. 9 *Schematic of the fabrication process: (a) the first UV lithography step to make the splitter pattern on photoresist (PR); (b,c) the second ion beam irradiation step to transfer the pattern in PR into silicon wafer, (c) is the cross section view cut from the yellow dashed line in (b); (d,e) cross section view of the last etching step, (d) the first etching step with porous Si (PSi) removed, (e) the second etching step with PSi remaining as the support, and the defects annealed. 73*

Fig 5. 10 *SEMs of the Y-shape splitters: (a) overview of two splitters; (b) the two arms, shorter for TM mode output, longer for TE mode; (c) the splitting point; (d) cross section of the input waveguide. 74*

Fig 5. 11 *Characterization setup. 75*

Fig 5. 12 *IR images of the splitters from the top: (a) equally splitting with a normal light input without polarization; (b) TE mode input gives a stronger splitting into the lower arm; (c) TM mode gives a stronger splitting into the upper arm. 76*

Fig 5. 13 *IR images of the outputs from the side (top) and scans of light density: (a) with TE mode input; (b) with TM mode input.....77*

Fig 5. 14 *Incident angle variation changes the polarization ratio: four different incident angles (A1, A2, A3, A4) gives different outputs at TE and TM modes.....78*

Fig 5. 15 *The output oscillation along the wavelength of the incident light.....79*

Fig 5. 16 *A comparison of (a) output power oscillation along the arm length in simulation with (b) that along the incident light wavelength in experiment.....80*

Fig 5. 17 *The output oscillation along the wavelength of the incident light, with waveguide width of ~ 7.5 µm.....81*

Fig 5. 18 *SEM image of the splitter on top, and schematic of the ion beam irradiation patterning process: I1, the first irradiation to pattern the two upper arms; I2, the second irradiation to pattern the lower arm.* *82*

Fig 5. 19 *SEM images of the splitter: (a) an over view, (b) magnified splitting region, (c) high magnification cross section of the lower waveguide, (d) cross section of the upper waveguide.* *84*
Fig 5. 20 *SEM images of the cross section of the lower waveguides with fluence : (a) 2×1014 ions/cm2, (b) 5×1013 ions/cm2* *84*

Fig 5. 21 *IR images of the light coupling into the 3D splitter from the top: (a) with , and (b) without a side light shining on the sample. The background is dark, because the light is confined in the waveguide.* *85*

Fig 6. 1 *Schematic of the fabrication process. (a) SOI wafer; (b) RIE to fabricate the microdisk, (c) aligned proton beam irradiation to make the defect region for the waveguide in the substrate layer, (d) oxide layer removing and Porous Si formation, (e) another etching step to undercut the bottom waveguide.* *89*

Fig 6. 2 *Optical micrographs of the disk pattern, (a) before and (b) after RIE.* *89*

Fig 6. 3 *SEM images of the first attempt, (a) overview of the vertically coupled waveguide and microdisk, (b) a magnified view at the coupling region.* *91*

Fig 6. 4 *Schematic of the positioning process.* *92*

Fig 6. 5 *SEM images of the first time result, (a) before and (b) after annealing.* *92*

Fig 6. 6 *SEM images of the result using UV alignment followed by a large area irradiation, (a) overview and (b) high magnification of the coupling region.* *93*

Fig 6. 7 *8 inch SOI wafer after epitaxial growth, device layer from 55 nm to 230 nm.* *94*

Fig 6. 8 *Microscope images of the UV alignment: (a) waveguides with a microdisk, (b) with a microring, (c,d) magnified images at the coupling region.* *96*

Fig 6. 9 *SEM images of the structures: with (a-d) fully developed waveguides to undeveloped central part.* *98*

Fig 6. 10 *High magnification of SEM images of the structures: (a-c) at the coupling region; (d) out of the coupling region.* *98*

Fig 6. 11 *Reduced surface and edge roughness: (a,b) over view, (c,d) fine view at the coupling regions. 99*

Fig 6. 12 *(a) Optical micrograph showing an overview of the structure. (b-f) show a schematic of the fabrication process viewed along a cross section at the dashed white line in (a). (b) SOI wafer dimensions, (c) RIE to fabricate the top Si waveguide (WG), (d) proton beam irradiation to create a high defect density (HDD) region for the lower waveguide in the substrate, (e) anodization resulting in oxide layer partial removal and PSi formation, (f) final anodization step to undercut the lower waveguide, followed by annealing to remove the lattice damage..... 100*

Fig 6. 13 *SEM images of the first attempt of vertical coupling waveguides (a) over view of the structures, (b) high magnification view of the coupling region, (c) cross section view of the two waveguides. 102*

Fig 6. 14 *Schematic of the light coupling between the two layer waveguides..... 102*

Fig 6. 15 *IR images of the light coupling from the lower waveguide to the upper waveguide. 103*

Fig 6. 16 *IR images of the light coupling for different coupling lengths and incident light polarizations. 104*

Fig 6. 17 *Schematic of the simulation structures. The substrate width and thickness: 10um, porous Si thickness: 5um, waveguides width: 5um. The thicknesses of the two waveguides and the gap varied..... 105*

Fig 6. 18 *Different lower waveguide thicknesses result in different coupling efficiencies. 106*

Fig 6. 19 *Simulation results: upper shows a schematic of the simulated structure, the waveguides width W and the upper waveguide thickness Tu are fixed. The two waveguides are attached, the lower waveguide thickness TL is varied; lower: plots the coupling efficiency for different TL along a coupling length of 11µm..... 107*

Fig 6. 20 *SEM images of the structure, showing low magnification views of (a) the full structure and (b) the coupling region, (c) high magnification cross section of the thick lower waveguide (~5.4 µm×2.5 µm), (d) plan view of the tapered portion of the lower waveguide. 108*

Fig 6. 21 *Thinner lower waveguide gives out higher coupling efficiency..... 109*

Fig 6. 22 *IR image and scan of the scattering light intensity along the waveguides. 110*

Fig 6. 23 *Simulation results: upper shows the actual triangular profile of the lower waveguide and simplified triangular profile used in the simulation; lower: plots the coupling efficiency of this profile*.....112

Fig 6. 24 *One lower waveguide coupling light into two upper waveguides. Arrow shows location of incident light in the lower waveguide.* 113

Chapter 1

Introduction

The word ‘photonics’ is derived from the Greek word ‘photos’ which means light. The science of photonics[1, 2] includes the generation, emission, transmission, modulation, signal processing, switching, amplification and detection/sensing of light. The term photonics emphasizes that photons are neither particles nor waves, but they have both particle and wave nature. Also, it more specially conveys the particle properties of light, the potential of creating signal processing device technologies using photons, the practical application of optics, and an analogy to electronics. Photonics covers all technical applications of light over the electromagnetic spectrum from ultraviolet over the visible to the infrared, with most applications in the range of the visible and near infrared light.

Many materials can be used for photonic structures, from polymers to semiconductors. Silicon has many excellent properties, such as its natural abundance, well-developed Si processing technology over decades and a broadband transmission spectrum, especially near-perfect transmission at a wavelength of 1.55 μm which is used by most fiber optic telecommunication systems. Because of these advantages, many scientists and engineers are working on Si photonics[3-5] using silicon as the optical medium. Silicon is usually patterned with sub-micron precision, into microphotonics components, which operate in the infrared, most commonly at 1.55μm.

Silicon photonic devices are typically fabricated on a silicon on insulator (SOI) platform,[4, 6, 7] and usually achieved by a lithography step followed by removal process such as reactive ion etching. This process is now quite well developed, and the devices fabricated using it can achieve very high performance. However, this Si machining process and some other typical processes can only fabricate two dimensional (2D), planar structures. To make the devices more condensed integrated and more functional, three dimensional (3D) structures are necessary. To achieve 3D structures, other additional processes are needed, such as wafer bonding[8-11], chemical vapor deposition (CVD)[12] and epitaxial growth[13, 14]. Such processes can help to achieve three dimensional photonic structures, but the processes are very complicated, time- and material-consuming. Moreover, the latter two are not applicable for Si devices. So a new Si machining process for fabricating Si photonic structures is desirable.

The following section gives a general introduction on the history of photonics and silicon photonics, followed by a brief review of some typical devices in Si photonics. A review of other studies on the fabrication of Si photonic devices is also presented.

1.1 Photonics and Si photonics

The word ‘photonics’ appeared in the late 1960s to describe a research field which uses light to perform various functions. Photonics as a field began with the invention of the laser in 1960, [15] which was then followed by other developments including the laser diode in the 1970s, [16, 17] optical fibers using for communication, and the erbium-doped fiber amplifier. These inventions form the basis of the telecommunications revolution of the late 20th century and provide the infrastructure for the internet. In the 1980s, fiber-optic data transmission was adopted by telecommunications network operators, and the term photonics came into common use. The establishment of a journal named Photonic Technology Letters by the IEEE Laser and Electro-Optics Society in the 1980s further indicated its importance.

Many materials can be used for photonic structures: from polymers to semiconductors. Photonics using silicon as the optical medium is called Si photonics. Because of the many outstanding properties of silicon, scientists and engineers have invested much effort in the field of Si photonics, which is a new technology platform to enable low cost and high performance photonic devices and communications. There are many different components in Si photonic systems, such as waveguides, beam splitters, couplers, resonators, etc.

1.2 Different devices in Si photonic structures

1.2.1 Waveguides

Waveguides are the fundamental component in photonics. There are several different types of waveguides: planar waveguides, rib and ridge waveguides, strip waveguides, etc. In planar waveguides [18], light is confined within two interfaces by total internal reflection, as shown in Fig 1.1(a). A rib waveguide [19, 20] can be defined with some normalizing parameters, Fig 1.1(b). Soref et al [20] firstly made this definition and limited the parameters as $0.5 \leqslant r < 1.0$, $\frac{a}{b} \leq 0.3 + \frac{r}{\sqrt{1-r^2}}$.

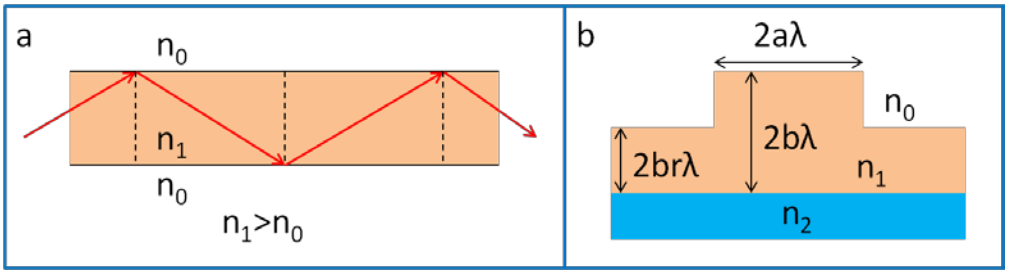

Fig 1. 1 (a) Total internal reflection at two interfaces in a planar waveguide, (b) Definition of a rib waveguide in terms of some normalising parameters.

A strip waveguide usually has a small dimension of ~500nm × 220 nm[21-25], so it allows a small bending radius of several micrometers[21, 24], which brings ultra-dense photonic circuits closer to reality. Strip waveguides provide an effective way to reduce the cost because of the simple fabrication process.

However, a major limitation is that the coupling is problematic since the dimension is so small.

A waveguide is a passive device which does not require a source of energy for its operation. There are some other types of passive devices, such as directional couplers [26, 27], multimode interference couplers[28], and beam splitters etc.

1.2.2 Couplers and splitters

When two waveguides are close together, the evanescent field of one waveguide can "feel" the other one, resulting in a gradual coupling of light between the two waveguides. The two waveguides make a directional coupler in which the coupling strength can be controlled by tuning the gap between the two waveguides, or the coupling length, etc. Identical waveguides can achieve full coupling, since they can confine electromagnetic waves with the same modes otherwise, partial coupling occurs. A directional coupler has many important applications. For example, it can work as a variable splitter, a polarization convertor or a base component for ring resonators. Using microelectromechanical systems (MEMS) it is possible to tune the coupling by tuning the gap between the two waveguides.[29]. A multimode interference (MMI) coupler has a central section which is a broad waveguide. It is a multimodal device, and allows multiple access waveguides.

A Y-junction is a typical beam splitter, featuring a straight waveguide and tapering portion followed by two branches. Here the aperture angle θ should be sufficiently small to make an adiabatic Y-junction with no splitting loss. A standard Y-junction usually has a large loss. Fukazawa et al. improved the design, and demonstrated an experiment result with a low excess loss of 0.3 dB. [30] However, this design requires very high lithographic resolution, so it is not achievable with most fabrication processes and conditions.

1.2.3 Resonators

Optical resonators are another important component in photonic structures. A photonic resonant structure is a particular material configuration of space in

which specific photonic resonances can be formed. It provides accurate control over photons in the temporal/spectral and spatial domains, or in other words, it provides the ability to harness the light. High index contrast structures can help to achieve strong photon confinement. The material from which they are made can be a dielectric or metal (plasmonics).

In dielectric materials, there are two strategies for photon confinement: refraction [31, 32] which makes use of total internal reflection; and diffraction [33, 34] where photonic crystals are used. Silicon is an ideal photonic material for confining resonant structures, since it is an excellent photonic conductor, and the silicon-on-insulator (SOI) high refractive index contrast provides an excellent combination of materials. Micro-disk and micro-ring resonators are two main typical resonators which use refraction effects, while photonic crystals use diffraction effects. Compared to micro-disks or micro-rings, photonic crystals usually have a lower Q factor, which means a worse spectral confinement of light, but they have a much smaller volume, which means that they allow denser integration. Hence photonic crystals are becoming more popular and have already entered the realm of practical devices.

1.3 Fabrication of Si photonic devices

Since the Si photonic devices are so important, many research scientists and engineers are working hard on processes to fabricate them in a variety of ways.

Waveguides are the most fundamental and simple devices, which is why some of the early experimental fabrication processes and studies were based on fabricating waveguides. Silicon waveguides were first reported by Soref and Lorenzo in 1985 and 1986.[19, 20] They used plasma-etching of an intrinsic epitaxially grown Si layer on a heavily doped Si substrate. They fabricated rib and ridge waveguides with losses reported as 15 dB/cm. They further developed this kind of waveguide on different platforms: Si-on-Al_2O_3 [35] and SOI [36] platforms. However, the loss still remained relatively high, which is a drawback in photonic devices.

SOI technology uses a layered silicon-insulator-silicon substrate other than conventional silicon substrates in semiconductor manufacturing. The

insulator layer could be silicon dioxide or sapphire, depending largely on intended application. Sapphire used is mainly for high performance radio frequency and radiation-sensitive applications. In photonics, researchers mainly use SiO_2-base SOI wafers. This kind of SOI wafer can be produced via Separation by Implantation of Oxygen (SIMOX),[37, 38] wafer bonding [39, 40], or seed methods[41].

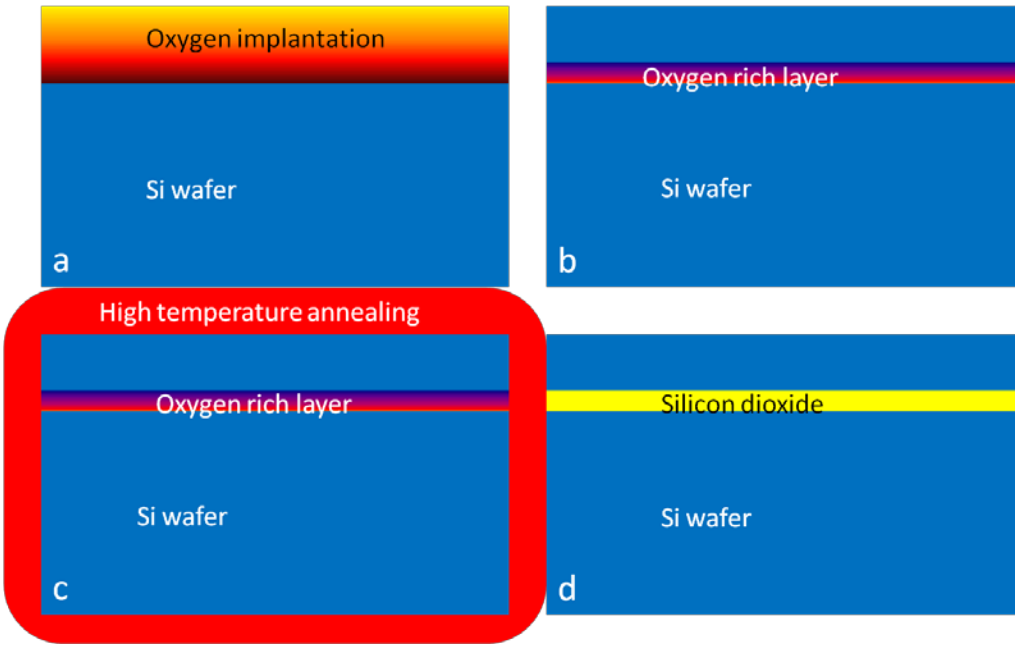

Fig 1. 2 SIMOX process, (a) oxygen implantation, (b) a rich oxygen layer formed, (c) high temperature annealing, (d) SOI wafer formed.

Two most popular ways are SIMOX and Smart Cut method (wafer bonding). SIMOX uses an oxygen ion beam implantation process followed by high temperature annealing to create the buried insulator layer. The process is shown in Fig 1.2, oxygen implantation is to form a rich oxygen layer at the end range of the ions. Then high temperature is applied to anneal the sample and to form a buried silicon dioxide layer in the wafer. This process is quite simple, but it is difficult to accurately control the buried oxide layer because of the uncertainty of the ion distributions in the wafer during oxygen implantation. The Smart Cut method is a prominent example of the wafer bonding process. It was developed by the French firm Soitec, using ion implantation followed by controlled exfoliation to determine the thickness of

the device layer. The schematic of the process is shown in Fig 1.3. It is a little more complicated than SIMOX, but it can achieve smooth surface and interfaces and accurate control over the thicknesses of device layer and oxide layer via polishing and thermal oxidation.

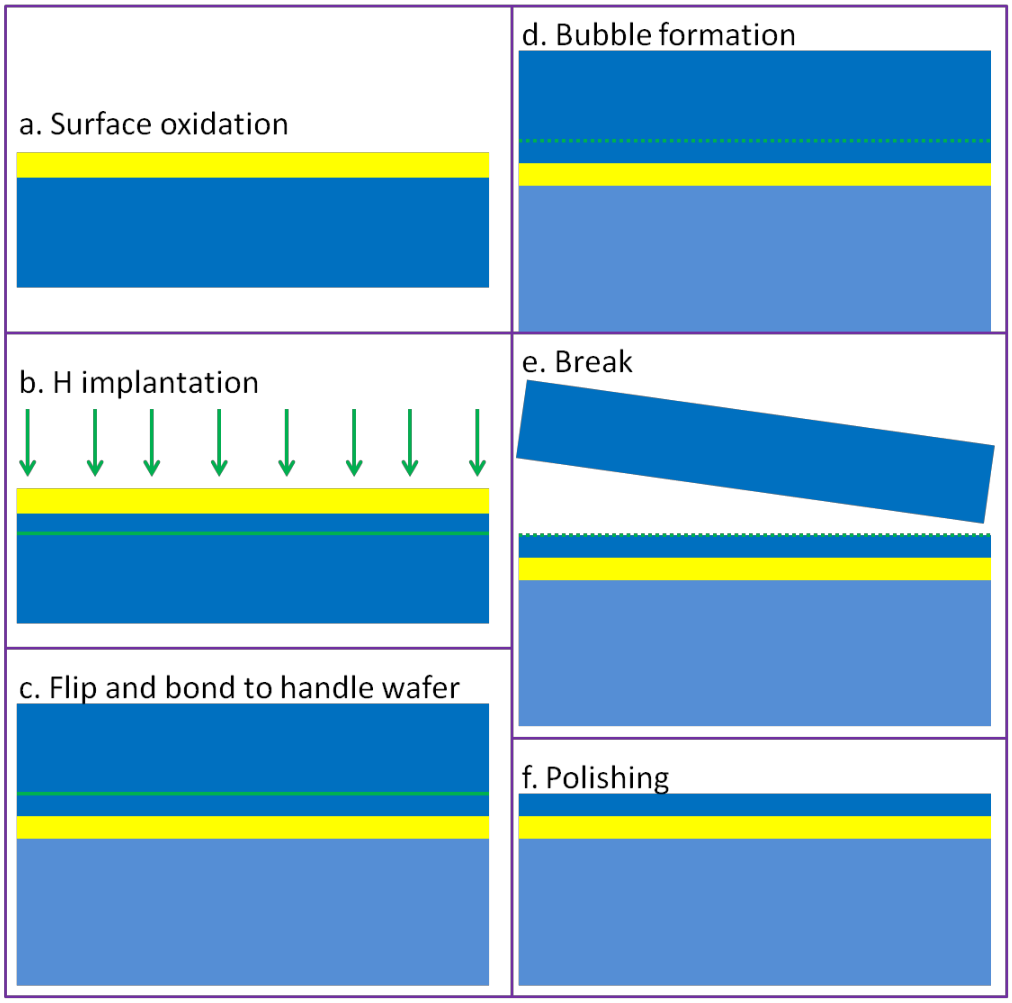

Fig 1. 3 A simplified schematic of Smart Cut process, (a) surface thermal oxidation, (b) H implantation, (c) flip and bond to handle wafer, (d) bubble formation, (e) break, (f) polishing.

SOI wafers were found to be an excellent platform for Si photonics, with work ongoing to the present day to fabricate low loss waveguides and other components on SOI platforms. Pafchek et al.[42] reported a propagation loss of 0.36 dB/cm for TE and 0.94 dB/cm for TM polarization in 2009. In their experiment, the waveguides were formed using thermal oxidation on a SOI platform. In the same year, Cardenas et al.[43] demonstrated silicon

waveguides with an even lower loss of 0.3 dB/cm, which were defined by selective oxidation. An even lower loss of 0.1 dB/cm for TE polarization was reported by Gardes et al. in 2008.[44] All these studies demonstrated that low-loss silicon waveguides could be achieved, however, the processes used are not widely applied in the fabrication of photonic devices since they are complicated.

The use of SOI platform provides a major breakthrough in the development of silicon photonics. At present, the most commonly-used process is dry or wet etching following a lithography process on a SOI wafer. [22, 24, 31, 32] This process is quite simple and direct and many good results have been achieved. However, SOI wafers are very costly compared to bulk Si wafers and their use only provides a means to fabricate 2D structures. To fabricate 3D structures in SOI, additional processes such as wafer bonding, CVD or epitaxial growth, would be necessary which would make the fabrication complicated and expensive. Therefore a cheap, simple fabrication process which is capable of making both 2D and 3D photonic structures is highly desirable in the drive for densely integrated devices.

1.4 Objectives

As discussed above, there are excellent existing processes to fabricate 2D photonic structures. Although they can achieve very good results, they are mainly based on SOI wafers which are expensive. Furthermore, to fabricate 3D photonic structures, some additional processes are necessary which make the fabrication process complicated, time-consuming and material-consuming.

This thesis presents a possible solution to these limitations using a silicon micromachining process which uses ion beam irradiation followed by electrochemical anodization (refer to 2.2). As this silicon machining process is still being developed, several important aspects need to be further investigated, so the objectives of this thesis are to:

- Further develop this Si machining process in two particular aspects, which are to investigate the etching rates after irradiation by different

ion energies with different fluences, and study the conditions under which high resolution structures can be fabricated.

- Apply this machining process to fabricate some 2D photonic structures, especially for microdisk and microring resonators, isolated and coupled with waveguides, also Y-shape splitters, and optically characterize them.
- Further apply this machining process to achieve 3D photonic structures such as 3D beam splitters on bulk silicon wafers, vertically-coupled waveguides and waveguide-resonators on a SOI platform. Suitable simulations and device characterization.

The results of this study are aimed at improving our understanding of, and extending the capability of our silicon machining process via ion beam irradiation. It may also provide an alternative and cheaper way of fabricating 2D Si photonic devices. Moreover, it may help to achieve an easier and cheaper way to fabricate 3D Si photonic structures.

Si photonics is now well developed and many studies of different aspects are being carried out. However, this thesis does not cover the range all of the studies, instead it mainly focuses on demonstrating a way of fabricating 2D and 3D photonic structures with some important components in Si photonics as examples. The main discussion is focused on the fabrication processes, along with some simulation and characterization studies to show how the fabricated devices work.

In the next chapter, relevant background information on various topics will be presented for better understanding of the experimental work which will be discussed in later chapters.

Chapter 2

Background

This chapter provides relevant background information on various topics essential for better understanding of the experimental work which will be discussed in later chapters. Firstly, the formation mechanism of porous silicon will be discussed, followed by the effect of ion irradiation on this process. Previous work on silicon micro-machining via ion beam irradiation will also be discussed. A short introduction of the facilities we have used during the experiment, mainly in CIBA, also some in IMRE are then presented.

2.1 Introducing porous silicon

Porous silicon (PSi) was discovered by Uhlir [45] at the Bell Laboratories in 1956 when he was doing electropolishing experiments on silicon with an electrolyte containing hydrofluoric acid (HF). When the applied bias is low, the etching of silicon would result in a system of disordered pores with nanocrystals remaining in the inter-pore regions. PSi studies were further developed for its use on developing silicon on insulator (SOI) technologies [46, 47], and its photoluminescence at room temperature [48, 49]. Recently, it has found applications in many areas like photonics [50, 51], silicon micromachining via sacrificial PSi [52, 53], and biosensors in biotechnology [54-56]. The work in this thesis revolves around silicon machining mainly for photonic applications as well as using PSi as a sacrificial material for the machining of silicon structures.

PSi is created by electrochemical anodization in a HF solution. Platinum is used as the cathode as it does not react with HF. The formation of PSi is an electrochemical process which proceeds only in the presence of

electrical holes. There are 3 categories of pores according to their geometries: micropores (<10nm), mesopores (10-50nm) and macropores (>50nm) [57]. The type of pores which are formed depends mainly on the resistivity and type of the silicon wafers. Low resistivity silicon wafers (<0.1Ω·cm) form mesopores; moderate resistivity wafers (0.1-50Ω·cm) form micropores; while high resistivity wafers (>50Ω·cm) for macropores. HF alone is unsuitable for the electrochemical etching process as the silicon surface is hydrophobic. An ethanoic solution is used as it increases the wettability of silicon and allows for better surface penetration by HF, so to make the porous layer more structurally uniform. An ethanoic solution also acts as a surfactant and reduces the hydrogen bubbles created during the anodization.

PSi is formed on bringing electrical holes to the surface. This is achieved differently for different doping types of the wafers. For p-type silicon wafers, when an electrical bias is applied, with the back surface of the wafer connected to the anode by electrical Ohmic contact, and a platinum grid in front of the sample as the cathode, an electric field in the solution causes the electric holes to drift to the surface of the silicon sample, enabling pore formation to proceed. The holes are abundantly available within the sample. For the n-type samples, holes are created by illuminating the sample with a halogen light during the anodization. The light breaks electron-holes pairs, allowing liberated holes to reach the wafer surface [57]. In this thesis, the various work and experiments use only p-type silicon wafers, since n-type silicon is not applicable for the ion beam irradiation induced silicon machining process used in this thesis.

There have been many proposed explanations for the formation of PSi, however, the most commonly accepted explanation is described in Ref [57-59]. When the electrical circuit is connected, hydrogen atoms bind to the silicon atoms at the surface, and the electron holes travel to the surface due to the applied bias. This facilitates a nucleophile attack on silicon atoms by fluoride ions and releases H^+ during the process. Electronegative fluorine polarizes the bonds by attracting electrons from the silicon atoms, and weakens the other silicon bonds as well. The weakened bonds are subsequently attacked by other

fluoride ions, until a SiF_4 molecule is released into the HF solution. The SiF_4 then reacts with 2 HF molecules to form H_2SiF_6 which will then ionize. This chain of reactions then occurs to other surrounding silicon atoms, breaking down the silicon structure on the surface of the wafer and pores start to form. The overall process for formation is as follows:

$$Si + 6HF \rightarrow H_2SiF_6 + H_2 + 2H^+ + 2e^-$$

A schematic of the chemical processes during PSi formation according to this model is shown in Fig 2.1.

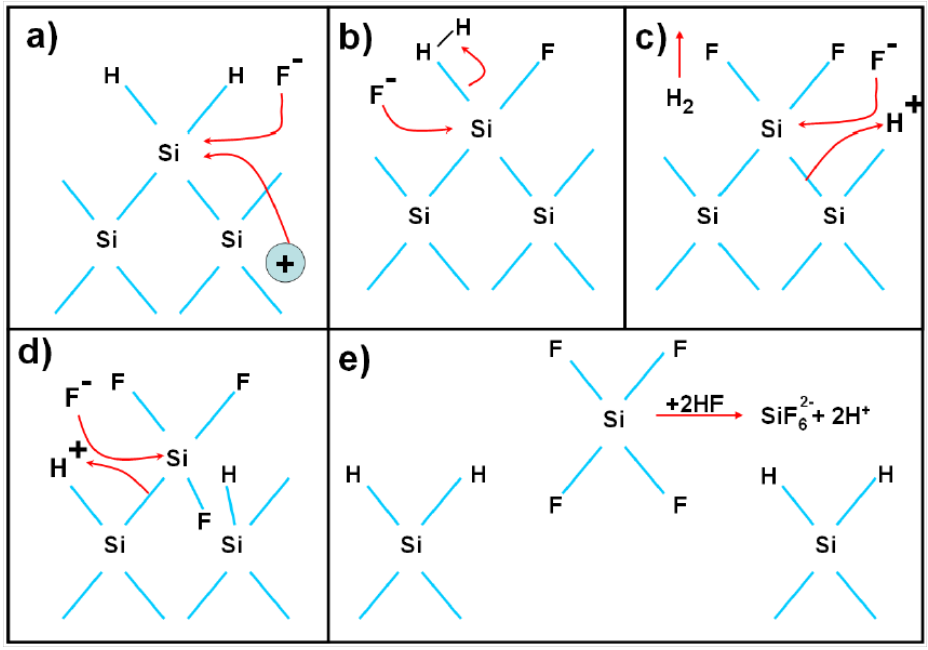

Fig 2. 1 Chemical processes of PSi formation. From [57]

2.2 Ion irradiation induced Si machining

Proton and helium ion beam irradiation of silicon result in damage to the crystal lattice, which can be used in many different ways. Protons lose energy as they penetrate the silicon wafer and stop at a well-defined end-of-range depth. The stopping process damages the silicon crystal by producing additional vacancies/defects in the silicon lattice [60]. Different ion beam fluences (number of ions/cm^2) produce different defect concentrations. Hence,

a localized pattern of damage can be introduced to the wafer by irradiating the silicon wafer with different fluences at different locations. In p-type silicon wafers, higher localized damage effectively means higher localized resistivities experienced during the followed electrochemical anodization process to form PSi in HF.

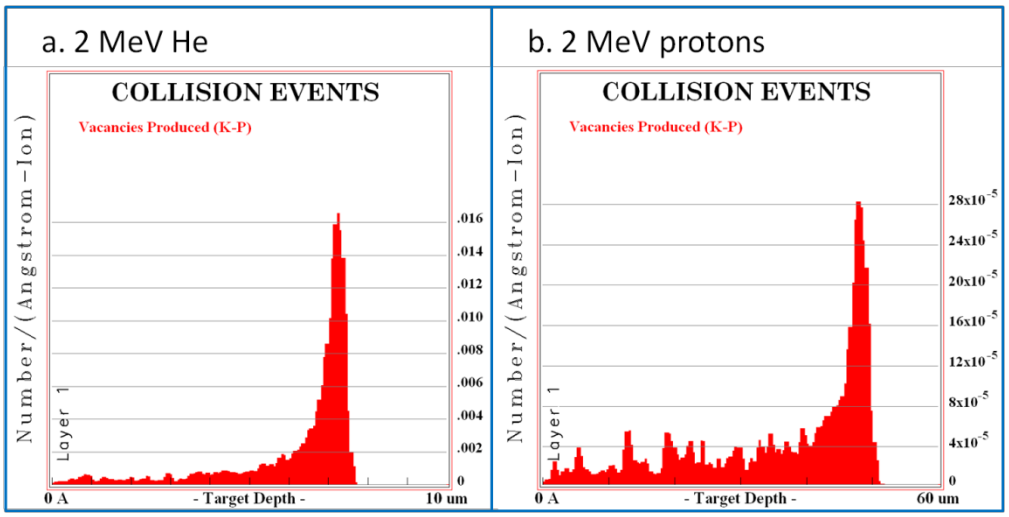

Fig 2. 2 SRIM plots showing the defect density distribution in silicon by 10,000 (a) 2MeV helium ions and (b) 2 MeV protons.

Proton and helium beams irradiating a silicon wafer have similar effect in terms of their damage to the crystal structure, producing defects in the silicon lattice. However, there are two main differences to using the same energy of proton and helium beams. As shown in Fig 2.2, using the SRIM software [61], the difference in the number of defects generated by 10,000 2MeV protons and 10,000 2MeV helium ions per ion per Angstrom are plotted. From the two plots, it can be seen that the range of the helium beam is much less than the proton beam at the same energy of 2 MeV. In addition, after integrating the total number of defects for each plot respectively, it is found that each helium ion generates approximately 20 times more defects than each proton.

From Fig 2.2, it can also be clearly observed that the defect density increases significantly at the end of range for both proton and helium beams.

SRIM is also able to generate tables of stopping ranges for different energies of ions in different materials.

The localized increased resistivity of silicon from the ion irradiation has two main effects on the formation of PSi:

1. The irradiated regions with higher fluences have higher defect concentrations hence higher resistivities.
2. With this increased resistivity, the hole current is reduced at irradiated regions during anodization causing the PSi formation rate to slow down compared to the unirradiated regions, producing a thinner layer of PSi.
3. When the ion fluence is large enough, the hole current is deflected away from these irradiated regions entirely due to the high localized resistivity and there is no PSi formation at these regions.

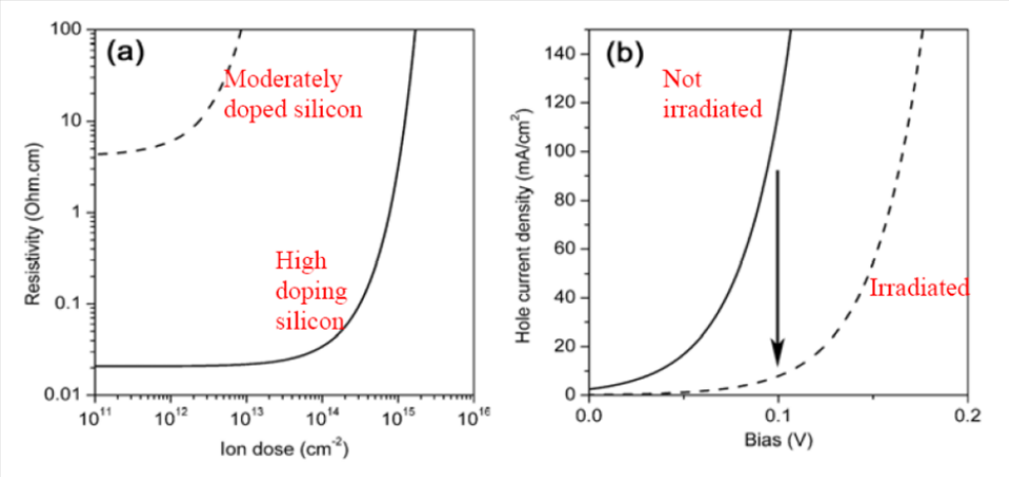

Fig 2. 3 (a) Plot showing the relationship of between resistivity and the amount of ion irradiation for highly doped (0.02 Ω.cm) and moderately doped (0.1-1 Ω.cm) silicon samples. (b) I-V plot for the anodization process. With increased irradiation fluence, the whole I-V curve will shift to the right, implying that with constant bias applied, the current flowing through the irradiated regions is lower than the current owing through unirradiated regions. From [60]

The resistivity of p-type silicon as a function of 2MeV helium ion irradiation fluence is plotted in Fig 2.3(a). Fig 2.3(b) shows current density versus applied bias curves for p-type silicon being anodized in a HF

electrolyte. The curve representing a certain fluence of ion irradiated area shifts to the right with respect to unirradiated regions. This means that, with a fixed applied bias, the local current density through the irradiated region is smaller as compared to unirradiated areas. For example, with a bias of ~0.1V, the current density is ~80 mA/cm^2 through a low resistivity wafer (0.02 Ω·cm), while it is ~8 mA/cm^2 through the irradiated region. The reduction of current density flowing through the irradiated regions results from the fact that localized resistivity has changed. Meanwhile, the pore sizes and the type of PSi (mesoporous, microporous or macroporous) change as well since the type of PSi formed depends mainly on the resistivity of the silicon wafer [57]. This influence on the type of PSi formed was studied in Ref [60].

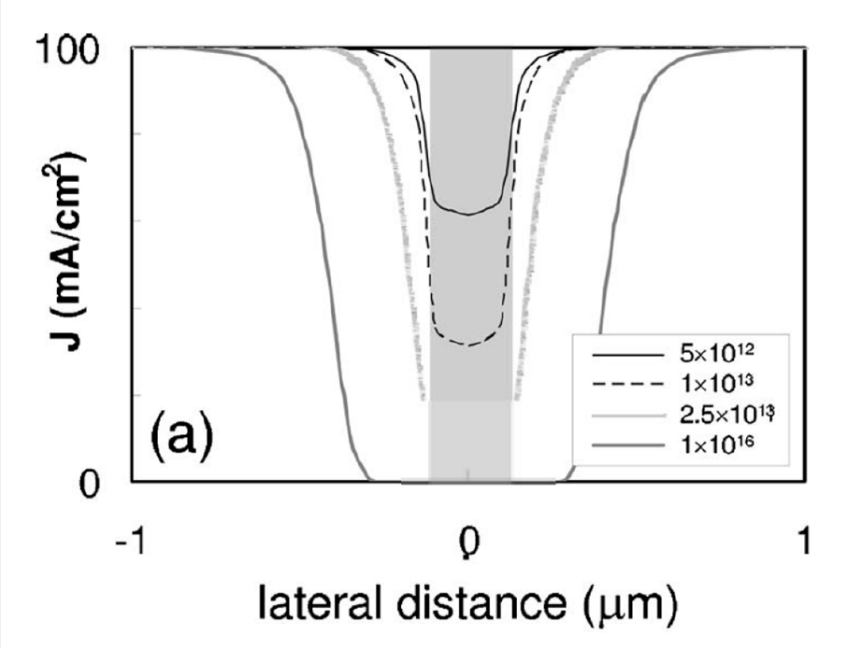

Fig 2. 4 MEDICI plots of current density J across a region containing a single irradiated line (gray area) for different fluences. The curves are normalized to the same J in the background for easier comparison. From [62]

Fig 2.4 shows the current density J across a region of a 3 Ω·cm wafer containing a line irradiated with different proton fluences[62]. At low fluences, J through the irradiated line remains significant, which means that PSi will still form at the irradiated line but at a lower rate than the unirradiated background. In the low-fluence range, J, and hence the physical and electronic

properties of the PSi in the irradiated line vary rapidly with fluence. PSi and silicon with a variable height of the machined features can be produced with accurate control over the fluence. When the fluence is high enough (10^{16}/cm^2), J reduces to zero across the irradiated line, so little or no PSi is expected to be formed.

The effects of ion irradiation on PSi formation was described above. This is the fundamental principle underlying all the fabrication work presented in this thesis.

2.3 Centre for ion beam applications (CIBA)

At CIBA, energetic ions are produced by a 3.5 MV high brightness High Voltage Engineering Europa Singletron^{TM} ion accelerator [63, 64]. Ions are created by exciting a gas with a radio frequency source. Various types of ions can be created from gases using this process. In this thesis, those used are primarily protons (H^+ and H_2^+) and singly-charged helium ions (He^+). After the ions are created, they are gradually accelerated along the electric field gradient of the accelerator tube (Fig 2.5) to the desired energy. The energies used for this thesis ranges from 100 keV to 2 MeV, and for Si photonic work, the energies mainly ranges from 100 keV to 500 keV.

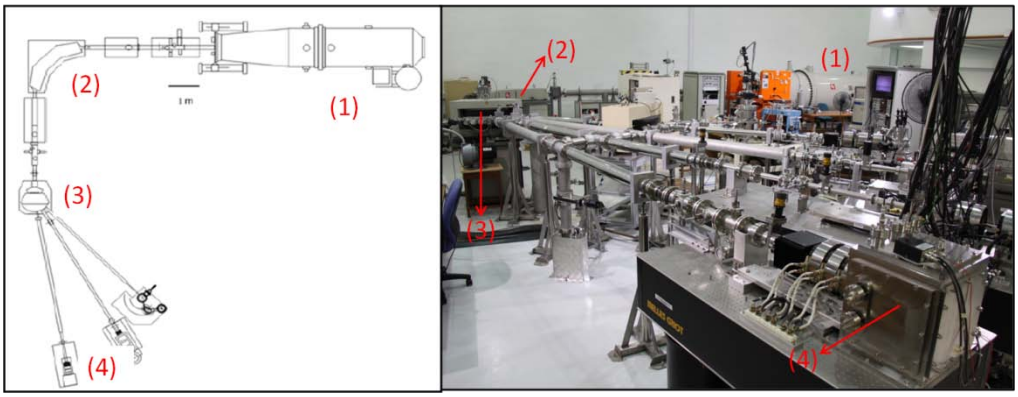

Fig 2. 5 (Left) Top down schematic diagram of the ion beam setup in CIBA; (Right) Actual image of the facilities. (1) the accelerator, (2) 90° magnet, (3) switching magnet, (4) end-station chambers.

After acceleration, the ion beam passes round a 90° bending magnet (Fig 2.5 (2)), which precisely selects the desired ion type and energy. When

the beam passes through a magnetic field, it will be curved at an amount depending on the charge and mass of the ions as well as the energy they possess. Fig 2.6 shows a schematic of the 90° magnet. A strong magnetic field is pointing out of the page. As the positively charged ions pass through it, a Lorentz force is induced. According to the left hand rule, the induced Lorentz force is to the left, so to curve the trajectory of the beam towards the left. For ions with different charges, masses and energies, the curvatures of their trajectories are different as they pass through a fixed magnet field. (Fig 2.6) There is only a small opening for the beam to exit, which means that only the ions curved with a certain angle can pass through this aperture. Thus to adjust the strength of the magnetic field, we can select exactly the desired ions with a certain charge, mass and energy to exit, while others are trapped.

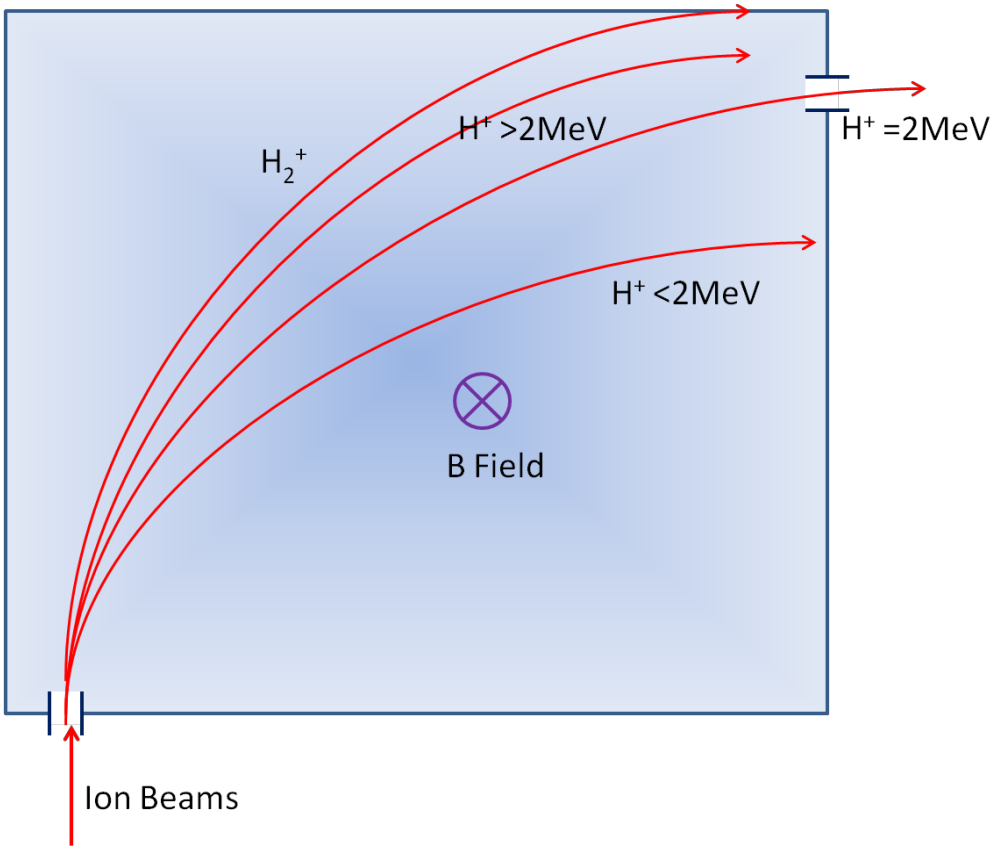

Fig 2. 6 Top down schematic of 2 MeV proton beam selection by 90° magnet.

An additional switching magnet (Fig 2.5 (3)) then guides the beam to a certain beam line and then to the desired chamber where the samples are

located. At present, there are beam lines located at 10, 20˚, 30˚, 45˚ and 90˚ with respect to the switcher magnet. (Fig 2.5). The 10˚and 20˚ beam lines are both designed for proton beam writing (PBW), which use a focused ion beam of MeV protons or helium ions to pattern a photoresist at nano to micron dimensions [65-73]. It is a direct-writing lithographic process, very similar to electron beam lithography which is using electrons to write patterns. The 30˚ beam line is designed for biomedical applications, such as nuclear microscopy[74, 75] and whole cell nano-imaging.[76, 77] The 45˚ beam line is designed for large area irradiation.[78] This will be further discussed in the later chapter. The 90˚ beam line is a high-resolution RBS facility.[79]

2.3.1 PBW

Magnetic focusing

Proton beam writing (PBW) is performed at the 10˚ and 20˚ beam lines. The 20˚ beam line is the new generation machine designed to improve on the performance of the first generation 10˚ PBW beam line. Work in this thesis was carried out only at the first generation PBW at 10˚beam line. It is called proton beam writing though, both protons and helium ions are used.

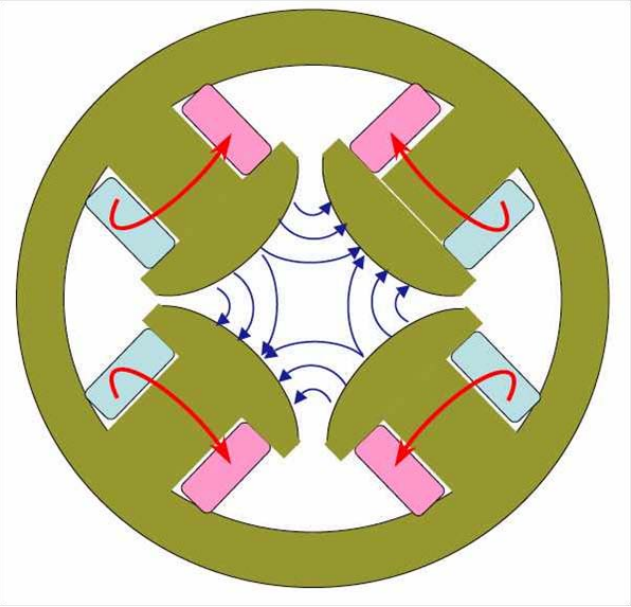

Fig 2. 7 Cross-sectional schematic of a quadrupole lens. The magnetic poles are created electromagnetically by coils. Red arrows indicates the direction of current flow in the coils to result in the desired magnetic polarity at the ends.

After passing through the switching magnet (Fig 2.9 (3)) and into the 10˚ chamber, MeV protons are focused by high demagnification OM52 magnetic quadrupole lenses from Oxford Microbeams. There are three lenses being utilized in the Oxford Triplet configuration [80-82]. Each quadrupole consists of four magnetic poles arranged in N-S-N-S configuration perpendicular to the ion beam (Fig 2.7).

Each lens focuses the beam into a line, thus two or more lenses are required to focus the beam into a spot. Three lenses are used on the 10˚ beam line. The lenses then form a demagnified image of an object aperture located just after the 90˚ magnet. The lens system presently on the 10˚ beam line has an object distance of 7 m and an image distance of 70 mm which enables a demagnification of 228 in the horizontal and 60 in the vertical directions. A resolution of 50 × 50 nm^2 [65] was achieved on this 10˚ beam line. Recently, better resolutions were achieved at 20˚ (19.0 × 29.9 nm^2)[73] and 30˚ (31 × 39 nm^2)[77]. Currently, this focusing system has the best proton beam focus in the world.

Beam scanning and blanking beam scanning

PBW is carried out by scanning pre-defined patterns over the surface of a sample. This is achieved using a scan amplifier, which deflects the beam in a fashion similar to an electron beam being deflected in a TV cathode ray monitor. The scan size can be set at the scan amplifier, along with the X to Y axis ratio of the area to scan. This allows the irradiation of simple patterns such as squares and rectangles. For complex patterns, the scan amplifier is controlled by a computer running IONSCAN [83, 84], a software package developed at CIBA. This software allows any scanning modification within the area fixed by the scan amplifier. IONSCAN reads the designed scan pattern in a pixel format and each pixel is treated as a point of irradiation. The designed scan pattern is usually designated as a bmp file. IONSCAN is able to control the shape of the scanned pattern and as well as the dwell time the ion beam spends at each location. The dwell time is a parameter which can control the fluence of the irradiation. To achieve a required fluence, the dwell time can be calculated based on the measured ion beam current during irradiation.

IONSCAN also controls a blanking system which can deflect the beam away from the original beam axis. The blanking system is installed before the switching magnet (Fig 2.9(3)). When blanking is on, an additional bias is applied, so the beam is deflected away from its original direction and out of the chamber. It is used to blank the beam when no irradiation is needed. With this, more complicated patterns can be irradiated within the same area fixed by the scan amplifier, the beam being blanked when moving from one figure to another.

2.3.2 Large area irradiation

The large area irradiation work is carried out using the 45˚ beam line. It was developed because there are several limitations of PBW especially for irradiating large area patterns on silicon wafers.

1. The maximum scan size which may be achieved using PBW is about 500 × 500 μm^2. So to achieve large area patterned irradiations, many smaller scanned areas would be necessary and stitched together. This needs very accurate alignment, thus has extreme requirement on the stage.
2. The current within the focused ion beam spot is only of the order of picoamperes, which is inefficient for large area irradiations.
3. Focused ion beam irradiation requires the beam to be extremely stable. Because any small fluctuation of the beam energy results in beam current variations, this results in a non-uniform fluence at the different irradiated positions. This would result in rougher machined silicon structures[85].

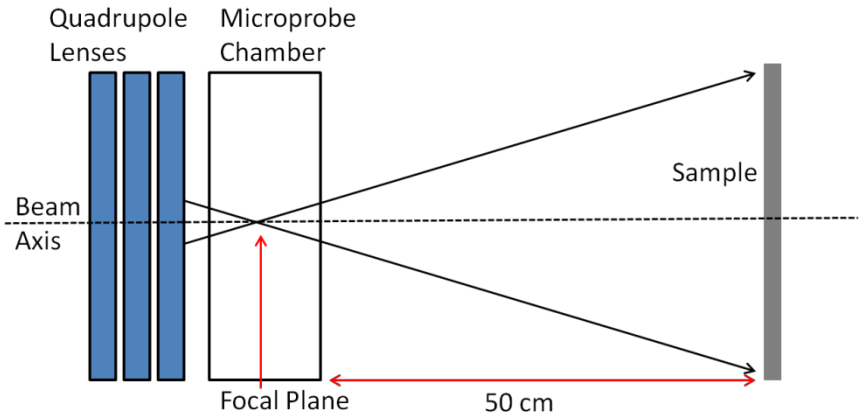

Fig 2. 8 Schematic of the ion beam defocusing for large area irradiation.

To overcome these limitations, the idea of using a large area irradiation geometry was conceived. The structures are firstly patterned on a thick photoresist (PR) prepared on the silicon wafer. Then a projected large area ion beam irradiates the whole surface of the sample to transfer the pattern from the PR into the silicon. The pre-patterned PR thus works as a mask for the irradiation.

The 45° beam line forms a demagnified image of the object aperture using several quadrupole lenses in the same way as the beam is focused. Fig 2.8 shows a schematic of the defocusing of the ion beam.

The large area irradiation facility uses the same focusing system but allows a beam current up to microamperes within the chamber as the collimator and object apertures are wide open. For a beam divergence angle into the quadrupole lenses of ± 0.4 mrad, the beam convergence at the focal plane is ± 32 mrad (about 2°) for a microprobe demagnification of 80. The wafer is positioned at a distance of 50 cm after the focal plane with an extension pipe. At such a distance, the beam is able to be divergent to distribute uniformly over an area of more than 30 × 30 mm^2, which is sufficient for most of the large area irradiation applications. If necessary, only a longer extension pipe is needed to obtain a even larger area.

A fluorescent screen is placed at the end of the extension pipe, with which we can view the beam to check its uniformity and location and to measure its area. Samples are mounted on a movable ladder and irradiation is carried out by moving the sample into the path of the beam in the extension pipe. The shadows of the samples on the fluorescent screen is often used to check if the sample is aligned at the right position so that it is fully or partially irradiated. We can adjust the quadrupole lens strengths to change the area of the beam.

Chapter 3

High and Low Energy Ion Irradiation Effects on Etching

This chapter introduces the equipment and setups used for the electrochemical anodization process as well as some important parameters for characterizing the anodization. Different anodization behavior after irradiation by high and low energy ion beams are then presented and discussed.

3.1 Anodization setups

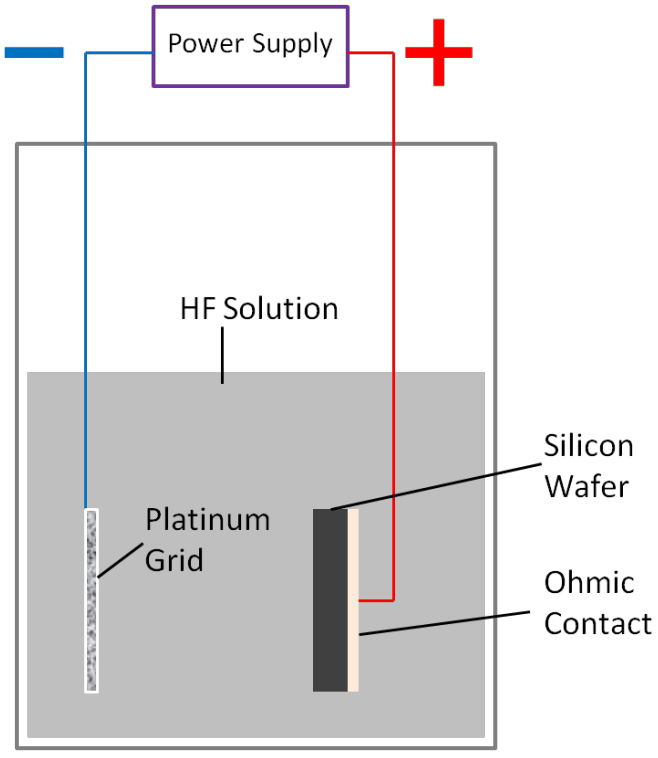

Fig 3. 1 Schematic of etching setup.

The electrochemical anodization setup includes a power supply, insulated electrical wires, a platinum grid, the prepared silicon sample, hydrofluoric acid (HF) solution and a Teflon beaker, as shown in Fig 3.1. The power supply is used to supply either a constant voltage or current. To keep a constant etch rate during anodization, we mainly used a constant current in this study. The silicon sample and platinum grid work as the two electrodes. Platinum is used because it does not react with HF during the anodization. As HF is highly aggressive to metals and glass, a Teflon beaker is used to carry out the anodization.

A piece of copper wire is used to conduct the electrical current to the sample. The sample is first dipped into diluted HF acid (2%) for 5-10 minutes and then rinsed in ethanol to remove native oxide at the back surface to improve the Ohmic contact between the sample and the copper wire. Gallium-Indium eutectic paint is applied uniformly at the back surface of the sample to create the Ohmic contact between the wire and the sample. This conductive paint enables the wire to stick to the sample as well as promote uniform current flow the between the wafer and the wire. Epoxy is then applied over the wire and the eutectic paint for protection against HF during anodization. When the epoxy dries, the sample is fixed and anodization may be carried out. Fig 3.2 shows a prepared sample.

Fig 3. 2 Prepared silicon sample for anodization.

Typically, a 12.5 % or 24.5 % concentration HF electrolyte is used. Usually, 25 mL of HF (49%, Fisher Chemicals), 25 mL of distilled water, and 50 mL of ethanol are mixed to obtain 100 mL of HF electrolyte of a 12.5% concentration. 24.5% concentration can be obtained by mixing half HF (49%, Fisher Chemicals) and half ethanol. The two electrodes are connected to a power supply and immersed into the electrolyte, Fig 3.1. The power supply used here is a programmable power supply (Model: Keithley 224 programmable current source) controlled by Labview software. This is particularly useful when it comes to the fabrication of multilayered structures in PSi as one need not manually tune the current density.

The platinum electrode is connected to the negative bias, and the sample to the positive. The two electrodes are oriented so that they are parallel to, and facing each other at a separation distance of ~1 cm. When there is no bias applied, the etching of silicon is negligible. Only when a bias is applied, the sample is anodized. The current and time of anodization depend on the experimental requirements. When the bias is applied, the anodization process begins and H_2 bubbles may be observed at the surface of the sample. Immediately after anodization, the sample is taken out of the HF solution and rinsed thoroughly with ethanol.

3.2 PSi formation rate

To fabricate any structure using this process, it is very important to know the PSi formation rate, so to be able to control the specific thickness of the PSi layer which is formed. The PSi formation rate is mainly determined by the applied current density, the resistivity type of the silicon wafer and the concentration of the HF used during the anodization.

For commonly-used p-type silicon wafers, there are three important different regimes of resistivity: 0.02Ω·cm, 0.1-1Ω·cm and 1-10Ω·cm. For convenience of distinguishing them in this work, we usually define them as low, medium and high resistivity respectively. Different resistivities of silicon wafers are used for different purposes. Low resistivity wafers are able to

provide fine structures.[86] However, the light transmission loss through it is high, arising from the heavy doping. High resistivity wafers are lightly doped, and too sensitive to ion irradiation, which results in a bad structure resolution during fabrication. For photonic structures, normally medium resistivity wafers are preferred [85, 87] since light transmission loss is not high and good resolution can be achieved during electrochemical etching after irradiation.

Wafers were anodized at different current densities J mA/cm^2 for time t and then cleaved for analysis. The cross sections of the samples were imaged and the cross sectional thickness d of the porous layer measured by SEM. The PSi formation rate is then obtained by dividing d by t. For medium resistivity wafers in 12.5% HF with a current density of 60 mA/cm^2, the PSi formation rate is ~2.6 μm/min. We also measured the PSi formation rate in 24% HF at current densities of 60 mA/cm^2, and 40 mA/cm^2. The result showed a ~2.4 μm/min rate at 60 mA/cm^2, and a ~1.9 μm/min rate at 40 mA/cm^2.

3.3 Effect of high energy ion beam irradiation

As discussed in Chapter 2.2, ion beam irradiation creates defects in silicon, so changing the electronic properties of the irradiated regions. Thus it also changes the etching behavior during electrochemical anodization afterwards. Generally, high-fluence, high energy ion beam irradiation decreases the etching rate or fully stop the etching with a high enough fluence.

Selected areas of medium and low resistivity wafers were irradiated with different fluences and anodized to a certain depth greater than the ion range. The PSi was then removed with KOH, revealing steps of various heights. As shown in Fig 3.3, areas irradiated with different fluences are etched to different depths. The low fluence irradiated areas (1×10^{14}/cm^2) were also etched, but with a reduced etching rate, which makes the area partially

etched, while the high fluence ($1\times10^{16}/cm^2$) irradiated area remains almost unetched.

According to SRIM, the defects are not uniformly distributed along the trajectory, Fig 3.4. This makes the longitudinal resistivity of the defect region not uniform, and thus the etching rate not constant. So we did not define and measure etching rate for defect region. Instead, we etched the sample to a depth much more than that of the whole defect region, and see how much of the defect region is etched. For example, as shown in Fig 3.3, we etched the sample to a depth of ~4 times of the defect region depth. Then we can measure the etched depth at the defect regions, h as shown in Fig 3.3 (d), and calculate the etched percentage of the whole defect region as $\frac{h}{H}\times100\%$.

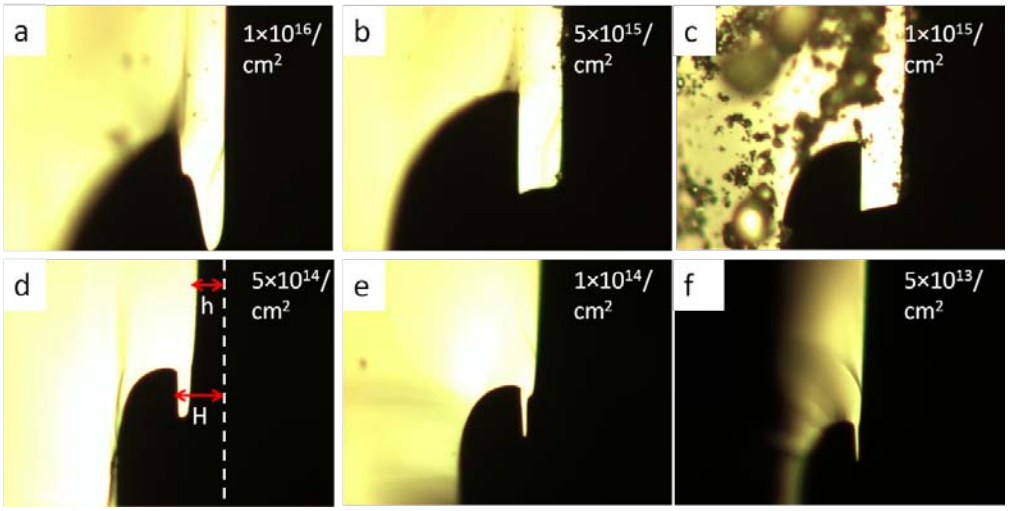

Fig 3. 3 Cross-section images of irradiated areas (1 MeV protons on medium resistivity wafer) with 6 different fluences ($1\times10^{16}/cm^2$ to $5\times10^{13}/cm^2$ as marked) in (a-f). (d) the white dotted line is the original surface of the wafer, h is the etched height of the irradiated areas, H is the height of the whole defect region.

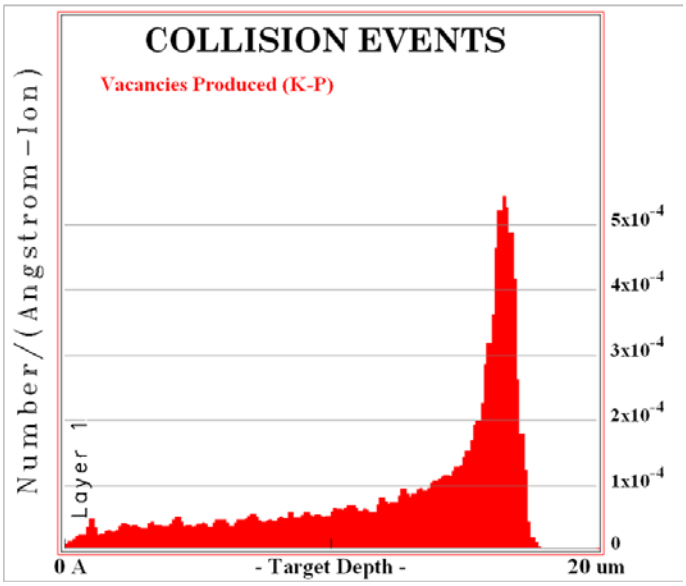

Fig 3. 4 Defect distribution created by 1MeV protons.

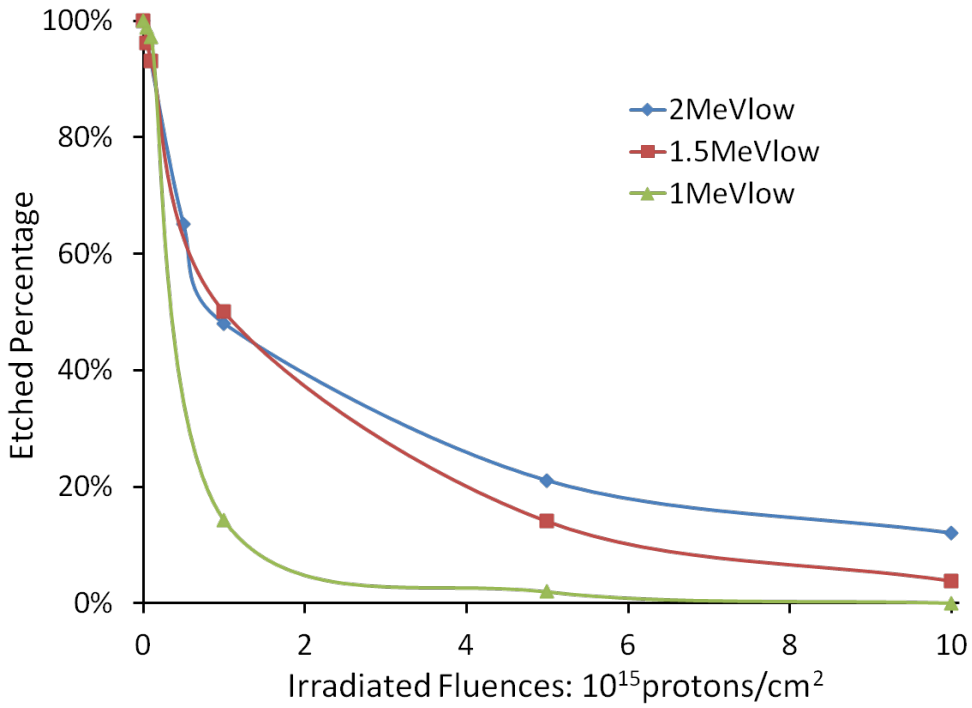

Fig 3. 5 Etched percentage at the defect regions of low resistivity wafers irradiated by different energy protons (1, 1.5, 2 MeV) with different fluences.

We tried three different energies of proton beams irradiating medium and low resistivity wafers. For low resistivity wafers, three different proton energies (1, 1.5, 2 MeV) were used to irradiate each of them with 6 different

fluences at 6 discrete areas. After etching and measuring the etching depth from the cross sections, we obtained a plot shown in Fig 3.5. According to the plot, lower energy ion beam reduces the etching more significantly. For example, in the plot, we see that for the same fluence of $5\times10^{15}/cm^2$, at 2MeV proton irradiated areas, 21% of the defect region was etched, and 14% for 1.5MeV protons. For 1MeV protons, with the same fluence of $5\times10^{15}/cm^2$, only 2% was etched. To explain this, we refer to Fig 3.4. We can see that along the longitudinal distribution of the defects along the ion trajectory, there is a high defect density peak at the end of range. Lower energy ion beam penetrated shallower in the material, thus the defect density peak at the end of range comes closer to the surface, and defects become more concentrated also owing to the lower depth straggling.

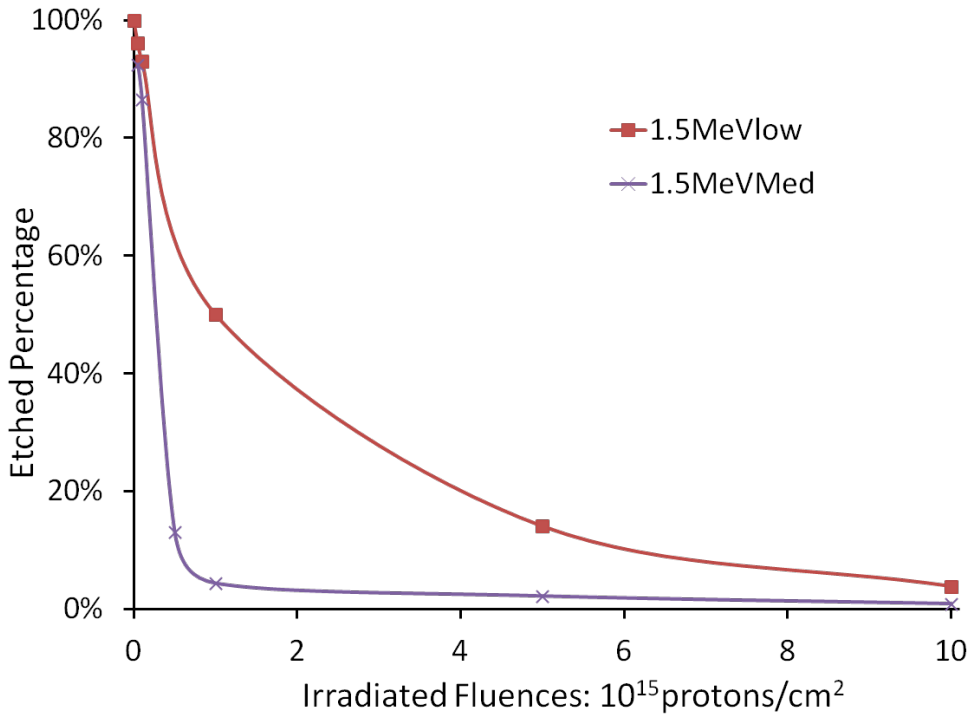

Fig 3. 6 Etched percentage at the defect regions of low and medium resistivity wafers irradiated by 1.5 MeV protons with different fluences.

Fig 3.6 shows the etched percentage of 1.5 MeV proton irradiation on low and medium resistivity silicon wafers. From the plot, we observe that the etched percentage is reduced rapidly with irradiation fluence from 0- to $1\times10^{15}/cm^2$ on medium resistivity wafers, from 100% to 4%. At a fluence of

$1\times10^{15}/cm^2$, only a very small amount 4% was etched, which means that anodization is almost stopped by irradiation with that fluence. While for low resistivity wafers, there is still significant etching, ~50%, at a fluence of $1\times10^{15}/cm^2$, and the value reduces much slower than for medium resistivity wafers. Thus it is easier to control the etching behavior with different fluences of ion beams on low resistivity wafers, and so to fabricate structures with fine-scale differences in feature height on it.

3.4 Effect of low energy ion beam irradiation.

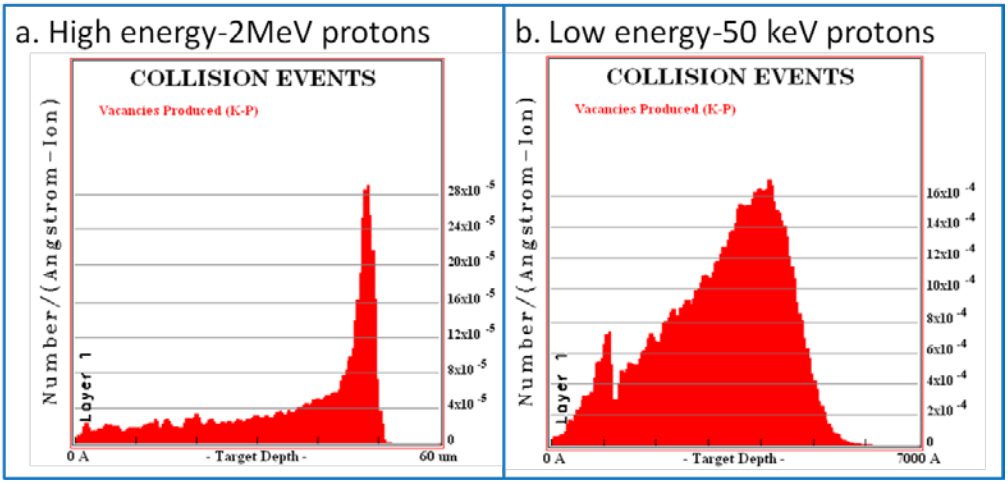

Fig 3. 7 SRIM simulations of defect distributions created by (a) high energy 2 MeV protons, with a long trajectory (>50 μm), low density from the surface, high defect at the end of range, and (b) low energy 50 keV protons, only distributed within a shallow depth close to the surface.

A high energy ion beam can penetrate deep into the material and form a deep defect region with a high defect density peak at the end of range, Fig 3.7 (a). When the energy of the ion beam reduces, the penetration depth decreases, till ~100 keV or even less, the significant density peak at the end of range disappears, Fig 3.7 (b), though there is still a small Bragg peak. We call such ion beam without a significant defect density peak at the end of range as low energy ion beam.

While a reduced etching rate occurs after irradiation by high energy ion beams, a totally different etching behavior is observed after irradiation by low energy ion beams. For example, as shown in Fig 3.8(a), when the irradiation fluence is not high enough, and the wafer is etched deeply, the irradiation volume is first undercut at its outer edges, as occurs for higher energies, but after a certain depth, it is more likely that etching will proceed through the central part of the irradiated disk. The disk area was irradiated by 100keV protons with a fluence of $1\times10^{16}/cm^2$, and the wafer was etched in 24% HF with a current density of $60mA/cm^2$ for 11min to an etching depth of ~26μm. We observe that it exhibits a normal undercut etching behavior from the edge towards the center of the disk till a distance of ~20μm. After that, the current passes through the central part of the irradiated disk area, leading to this region being very pitted and rough.

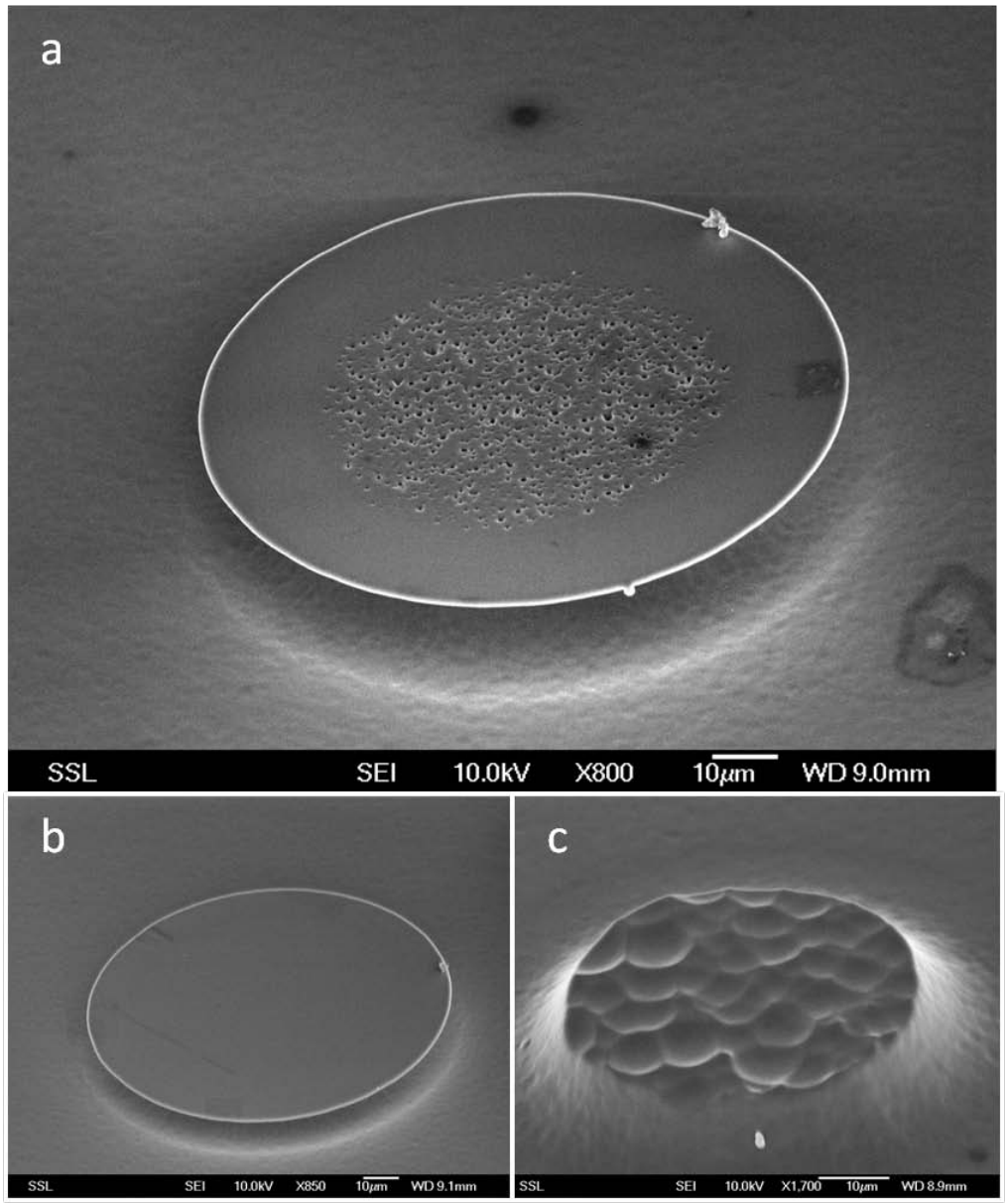

Fig 3. 8 Etching behavior after irradiation by 100 keV protons on a medium resistivity wafer: (a) showing a undercut lateral limit of ~20μm at fluence of $1\times10^{16}/cm^2$, the central part of the disk is partially etched through; (b) normal undercutting at fluence of $2\times10^{16}/cm^2$, (c) the central part is totally etched through, and the disk is lift off, at fluence of $2\times10^{15}/cm^2$.

When the wafer is irradiated by a low energy ion beam, the defect region is very thin as the penetration depth of the beam into the silicon is very shallow. During electrochemical etching, PSi formation soon reaches the end of range depth and starts undercutting the irradiation region. Undercutting

means that most of the current flow is deflected to the edge of the irradiated area.

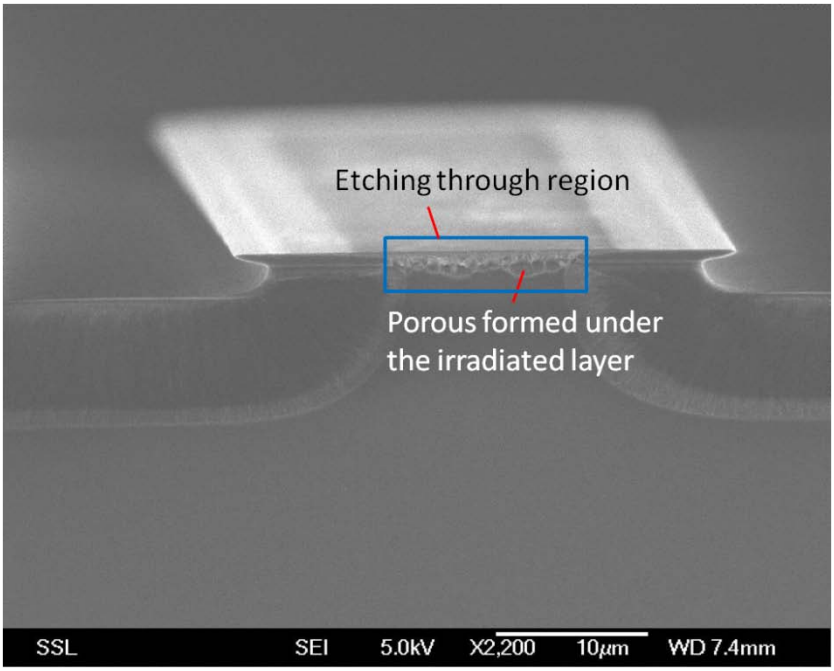

Fig 3. 9 Cross sectional SEM image showing the undercutting limit and etching through the irradiated region, a wide line irradiated with $1\times10^{14}/cm^2$ 100 keV H_2^+, which has a undercutting limit of ~10 μm.

This is because the defect region has a much higher resistivity than the surrounding unirradiated area, causing the hole current to preferentially be deflected around the bottom surface, rather than the direct short path to the surface through the defect region. However, there is still some current flowing through the defect region, as it accumulates to some point, macroporous silicon is formed at that region. Once macroporous silicon is formed, there are holes through the whole defect region since it is so thin that its thickness is the same dimension as the pore size, and the hole current can pass through them freely, rather than being deflected away.

The SEM image in Fig 3.9 provides proof for this assumption. A 30 μm wide line was irradiated with 100 keV H_2^+ ions to a fluence of 1×10^{14}

ions/cm^2. It was then etched to a depth of ~13 μm. From the cross-section shown in the figure, we see that, while the two sides of the line are normally undercut, the central part is etched through because macroporous silicon is formed. Once macroporous silicon is formed, and there are free path ways for the hole current, the region beneath the irradiated layer also starts to form porous silicon, Fig 3.9.

3.5 Difference between high and low energy ion beam irradiation

According to the above description, the etching behavior is different between high and low energy ion beam irradiation. High energy ion beams induce a decreased etching rate at the irradiated regions. The decreased rate depends on the ion energy and irradiation fluence. Low energy ion beam irradiations do not have such a clear effect, rather they induce an undercutting effect rather than a decreased etching rate.

To explain this phenomenon, we can firstly refer to Fig 3.7. It shows the defect distributions in silicon created by 2 MeV and 50 keV protons. A 2 MeV proton beam has a 50 μm penetration depth and creates defects along the trajectory, Fig 3.7(a). The depth distribution extends over a long distance from the silicon surface to the end of range. Most defects are created at the end of range, shown as the peak in Fig 3.7(a); above this end-of-range region the defect production rate is about one tenth of the peak value. Defects result in increased resistivity of the irradiated region. So long as the fluence is not high enough to fully stop the etching, it results in a decreased etching rate arising from an increased resistivity. Since the defect distribution created by a high energy ion beam extends over large depth and has gradual distribution, the decrease of the etching rate is a gradual effect.

The defects created by a low energy (50 keV) proton beam are confined to within only a ~500 nm region close to the surface. Any gradual change in etch rate is too difficult to observe within such a small depth, so the observed overall effect is that the irradiated region remains intact at a high fluence, leading to undercutting, or is etched through at a low fluence.

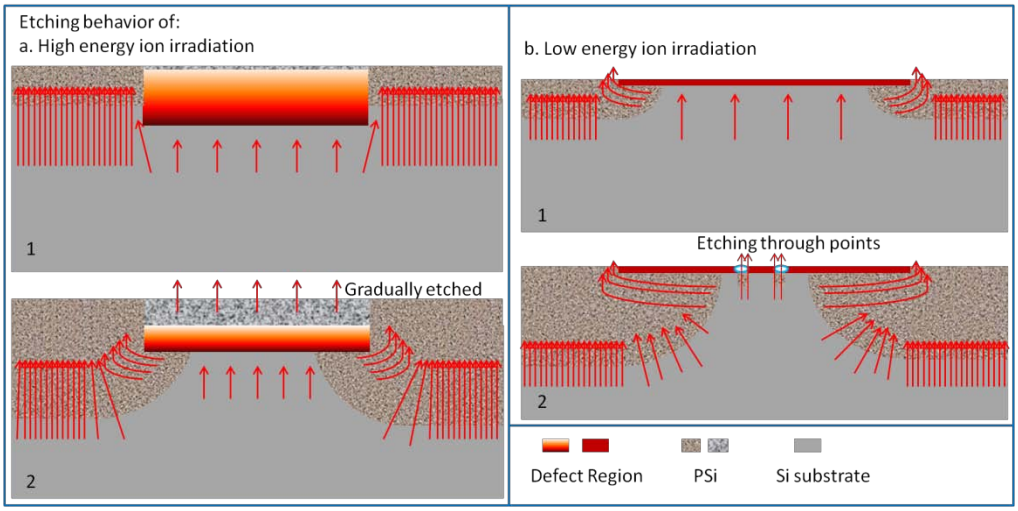

Fig 3. 10 A schematic showing the etching behavior of (a) High energy ion irradiation, a gradual process with the irradiated layer partially etched from the top; and (b) Low energy ion irradiation, an abrupt process with some etching through points at the irradiated area. The red arrow shows the current flow.

Fig 3.10 shows a schematic of the different etching behaviors of silicon after high and low energy ion irradiations. High energy ions penetrate deep into silicon, and form a thick defect layer with a high density peak at the end of range and much lower density distributed near the surface. During electrochemical etching, while most of the hole current goes through unirradiated areas, there is also some that goes through the irradiated, though much less than unirradiated areas, and porous silicon will also form from the surface of that region but with a much lower formation rate. It is a continuous and gradual process. Different from this, low energy ions form a very thin defect layer (~1 μm or less) without any significant longitudinal distribution. After irradiation, as the electrochemical etching goes, porous silicon formation will soon reach the end of defect region and start to undercut. Same as the high energy ion irradiation case, while most of the current goes through or being

deflected to the unirradiated areas, there is also some current which goes through the defect region. At the beginning, there may also be a very thin layer at that region which becomes normal porous silicon, which is so thin that it can hardly be observed. As the etching process continues, at some point, macroporous silicon is formed in that region with some big pores on the surface, Fig 3.8 (a), which are through the whole defect region from the unirradiated substrate under the defect region to the surface. Then there are many free path ways for the hole current through the defect region. So undercutting process stops, and porous silicon starts to form directly under the defect region.

Chapter 4

Optical Micro-resonators

This chapter mainly describes the fabrication of optical microdisk resonators using our micromachining process, and their integration with waveguides.

4.1 Introduction to optical microresonators

Optical microresonators (or microcavities) can confine light at resonant frequencies by light circulation within micro-sized dielectric volumes to enable storage of optical power and are important in a wide range of fields [88, 89]including photonics[90, 91], cavity quantum electrodynamics[92, 93],nonlinear optics[94-96], and biosensing[97, 98]. For example, they control laser emission spectra to enable long-distance transmission, or ensure narrow spot-size laser read/write beams in CD and DVD players.

An ideal resonator would confine light without loss and resonate at precise frequencies. In practice, a quality factor Q is used to describe the performance of a resonator.

$$Q = \omega\tau = \frac{\lambda}{\delta\lambda}$$

Q expresses the life time τ of the resonance normalized to the period of oscillation $T = \frac{2\pi}{\omega}$. It also describes the spectral confinement $\delta\lambda$ of the resonance at an operating wavelength λ.

The lifetime τ is the time interval of a coherent resonance oscillation confined within the volume of the resonator. In experiments, this can be measured by repeatedly scanning a laser into resonance with a critically

coupled mode until the power transfer increases to maximal 'charging' of the resonator, then gating off the laser input and observing the resonance ringdown. [88] The spectral confinement $\delta\lambda$ is the bandwidth, and could be directly obtained from the transmission spectrum.

Another property of the resonators is the merit factor F.

$$F = \frac{\tau\lambda^3}{TV}$$

F quantifies the confinement strength of the photonic resonance in the spectral and spatial domains. V is the volume of the resonator, or real space extension of the resonance. Optical microresonators are meant to control photons within the most confined space V ($/\lambda^3$) for the longest duration τ ($/T$).

According to the type of confinement method and their geometries, microresonators can be divided into several types: Fabry-Perot (micropost resonators)[99], whispering gallery (spheres, microrings, microdisks)[88] and photonic crystals[100]. Among these, microdisks and microrings are usually easy to fabricate and have high Q factors. So in this chapter, we mainly focus on the fabrication of microdisks, and also some of microrings.

Up to 2003, many researchers were working on the fabrication of high and ultrahigh Q microdisk resonators.[88, 89] Microdisks were fabricated on the wafer, then optical fiber was used to couple with them and measure the resonances. Ultra high Q values, as high as 10^8, were achieved by silica microdisks using dry etching followed by a selective reflow process. In 2006, Xu at al. [101]combined an unusual effect that occurs when two laser beams interact within an optical material, which is called electromagnetically induced transparency (EIT), and novel techniques of fabrication of microresonators, to demonstrate an on-chip, all-optical analogue of EIT based on the response of coupled optical microresonators. The result offered prospects of smaller, more efficient photonic devices for the manipulation and transmission of light. In 2009-2010, studies of optomechanical device actuation through the optical

gradient force were carried out using microdisk or microring resonators. [102-105] Till now, there are still many studies and applications based on microdisk and microring resonators. [106-109]

In actual use of a microresonator, there should be a waveguide coupled with it. According to the time-domain coupling theory, the optical transfer function of the waveguide is formulated by

$$F_{(\omega)} = \frac{j2t_R(\omega-\omega_0)+(\gamma-\kappa)}{j2t_R(\omega-\omega_0)+(\gamma+\kappa)}$$

t_R is the round-trip propagation time, ω_0 is the resonant frequency, γ is the round-trip resonator propagation loss, κ is the power coupling ratio between the waveguide and the resonator. γ is approximately equal to $2\pi R\alpha$, where R is the radius and α is the propagation loss, which primarily results from optical absorption and radiation in the material. κ is strongly dependent on the gap spacing.

At the resonant frequency, $\omega = \omega_0$, the optical transmission intensity is $T(\omega_0) = |F(\omega_0)|^2 = \left(\frac{\gamma-\kappa}{\gamma+\kappa}\right)^2$. When $\kappa < \gamma$, the system is under-coupled; when $\kappa > \gamma$, it is over-coupled. The critical coupling situation occurs where $\kappa = \gamma$.

4.2 Fabrication of microdisk resonators

The fabrication of microdisk resonators via ion beam irradiation and electrochemical etching on bulk silicon is simple and straight forward. We can directly use proton beam writing to write the disk pattern on the silicon wafer and then electrochemically etch it in HF solution to obtain the structure. For mass production, it is better to use UV lithography to make a photoresist pattern on the wafer, and then use large area ion irradiation to transfer the pattern from the photoresist into the silicon surface. The etching step is the same, directly using a current density of 60 mA/cm^2 for a certain time to form a layer of PSi, then removing the PSi layer in a diluted KOH solution (<10%). The etching time depends on the diameter of the microdisk. A bigger diameter

means the disk could be undercut more, so a longer etching time should be applied.

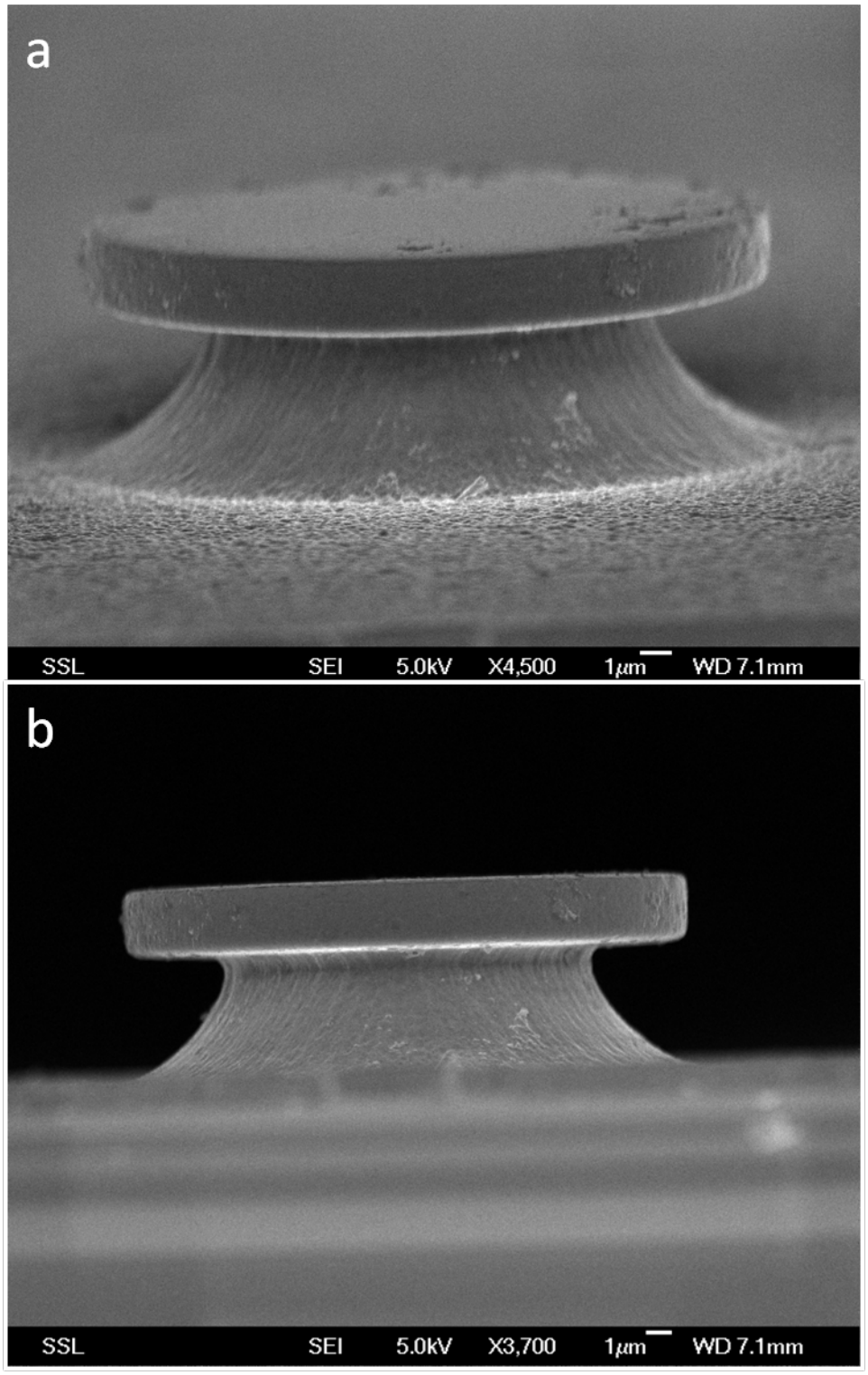

Fig 4. 1 SEM images of the microdisk fabricated via ion irradiation for the first time, (a) a tilted overview, (b) side view.

Fig 4.1 shows a microdisk fabricated using ion beam irradiation on bulk silicon for the first time. The diameter was ~20 μm. It was irradiated by 400 keV protons with a fluence of 1×10^{14} ions/cm^2 on a medium resistivity wafer. After proton beam irradiation and removing the photoresist, the wafer was etched in 12% HF solution with a current density of 60 mA/cm^2 for ~8 minutes to form a layer of PSi with a thickness of ~10 μm. Finally the PSi layer was removed by putting the sample into a diluted KOH solution. According to SRIM, 400 keV protons have a projected range of ~4.5 μm. However, the disk only had a thickness of ~3 μm in this case. That is because the fluence of 1×10^{14} ions/cm^2 was not high enough to fully stop the etching, the irradiated disk region was also partially anodized during the etching step. We can see from the figure that the surface and edge roughness was quite high, also arising from the low irradiation fluence. The 3 μm thickness of the microdisk is too large to obtain a single mode resonance within it. Thus a lower energy ion beam with a higher fluence was required to make a thinner and smoother microdisk.

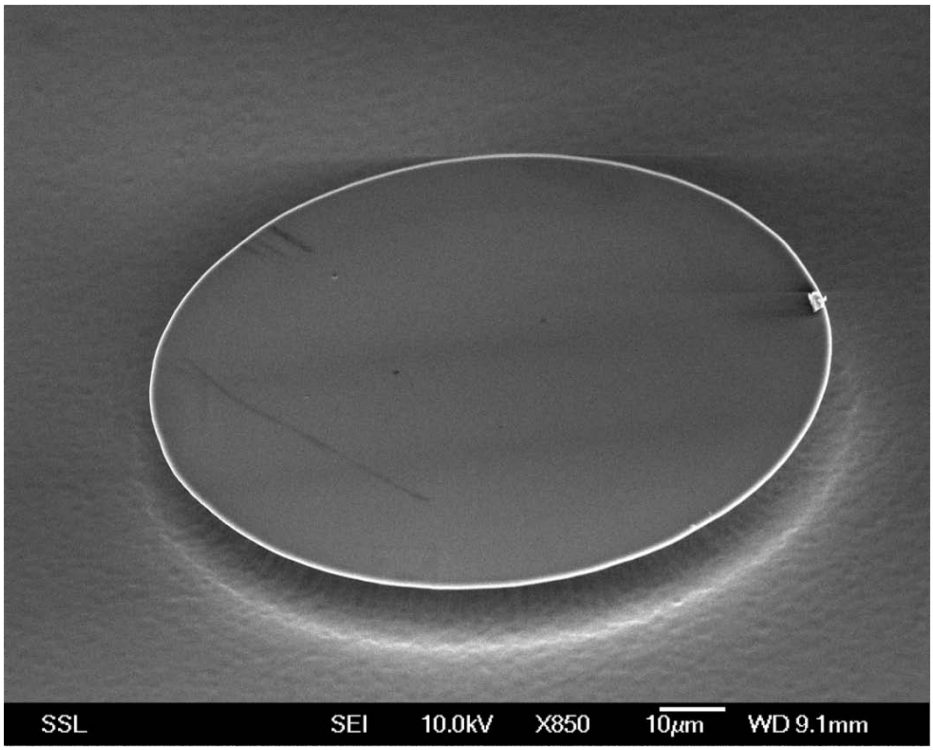

Fig 4. 2 SEM images of the microdisk fabricated by lower energy ion beam and higher irradiation fluence.

According to the problems identified during the above fabrication, we then used a 50 keV proton beam for the irradiation, and the irradiation fluence was increased to 1-2×10^{16} ions/cm^2. Fig 4.2 shows the result. The disk in the figure has a diameter of ~100 μm and a thickness of ~0.5 μm.

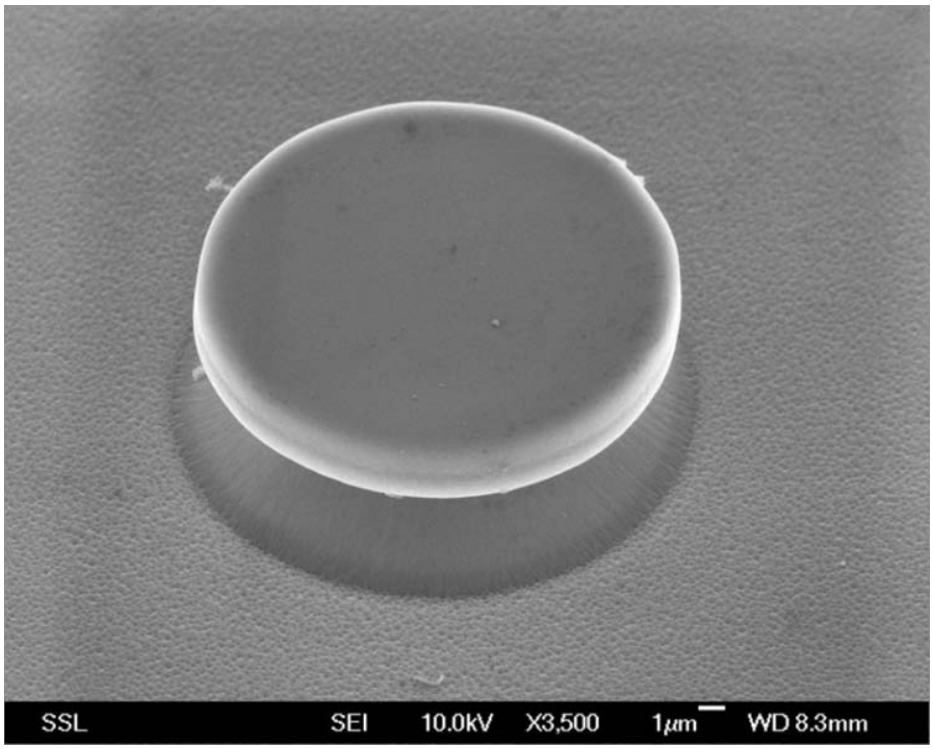

Fig 4. 3 Microdisk smoothened after thermal oxidation and annealing.

Before characterization, the microdisk was annealed at high temperature to remove the defects created by the ion irradiation. The sample was annealed in a high temperature tube in air at 1000 ˚C for 5-10 hours. During thermal annealing, the structures were also oxidized because of the high temperature. The outside oxide layer could be removed by putting the sample into HF solution. The sample was also smoothened by the thermal oxidation, Fig 4.3.

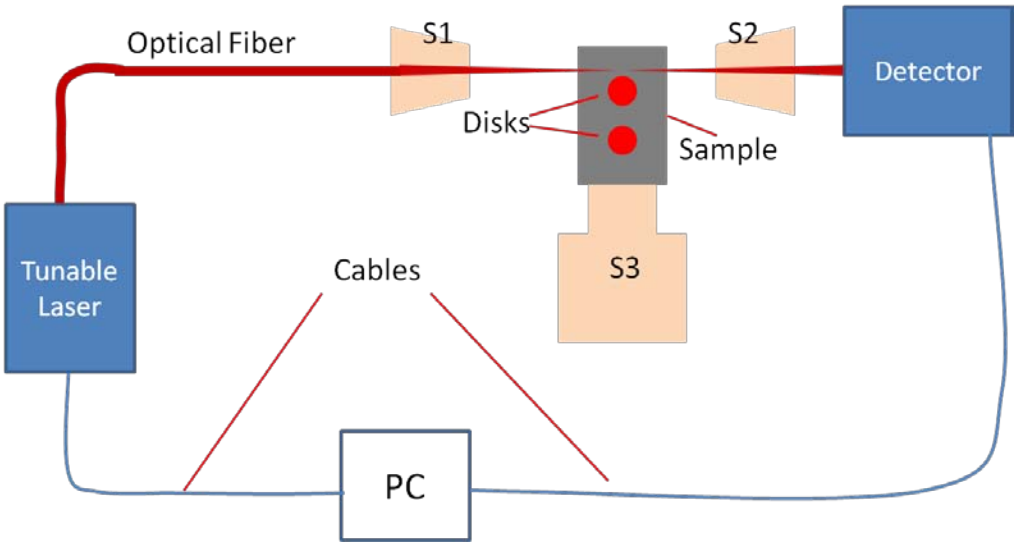

Fig 4. 4 Schematic of the measurement setup, the tapered optical fiber is positioned on two stages S1 and S2, the sample is also on a stage S3. The stages can move freely with a 20-nm-resolution, so to tune the coupling between the fiber and the disks.

To characterize such microdisk resonators, a tunable laser in the infrared range, with a wavelength around 1550 nm, was used as the incident light. Fig 4.4 shows a schematic of the optical setup. A tapered optical fiber was used to couple the light from the laser into the microdisk and then back to the detector. The fiber and sample were positioned on 20-nm-resolution stages and could be moved freely to couple the fiber to each of the microdisk resonators. We were able to find different coupling conditions by fine tuning the fiber position. An infrared camera on top of the sample was used to monitor the light coupling.

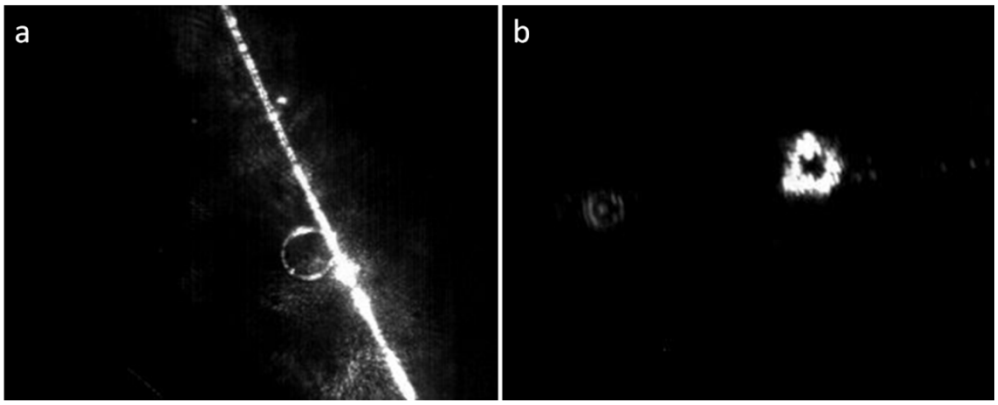

Fig 4. 5 Top view image of the light coupling, (a) under coupling, (b) critical coupling.

Fig 4.5 shows top view images of the light coupling between the fiber and the microdisk. When the light was coupled into the microdisk, we can see the light transmission around the microdisk, Fig 4.5(a). In this coupling situation, most light still stays in the fiber. At critical coupling however, most light is coupled into the microdisk, and circulates within it at resonance, Fig 4.5(b).

At a critical coupling situation, we obtained the transmission spectrum of the silicon microdisk resonator through the free space output of the fiber, as shown in Fig 4.6. The measured free spectral range (FSR) was about 7 nm, the highest Q value was about 1,017 at the third resonance with resonant wavelength at 1545.65 nm, and the merit factor F was 4.7. This result is not good as a Q value of only 10^3 is quite low compared to the mentioned ultra high Q value 10^8.[88] However, it was the first time that a silicon microdisk resonator was fabricated on bulk silicon wafer with a single etching step. The low Q value was probably because of the roughness of the disk edges which could be reduced by further lithography optimization and higher ion irradiation fluence.

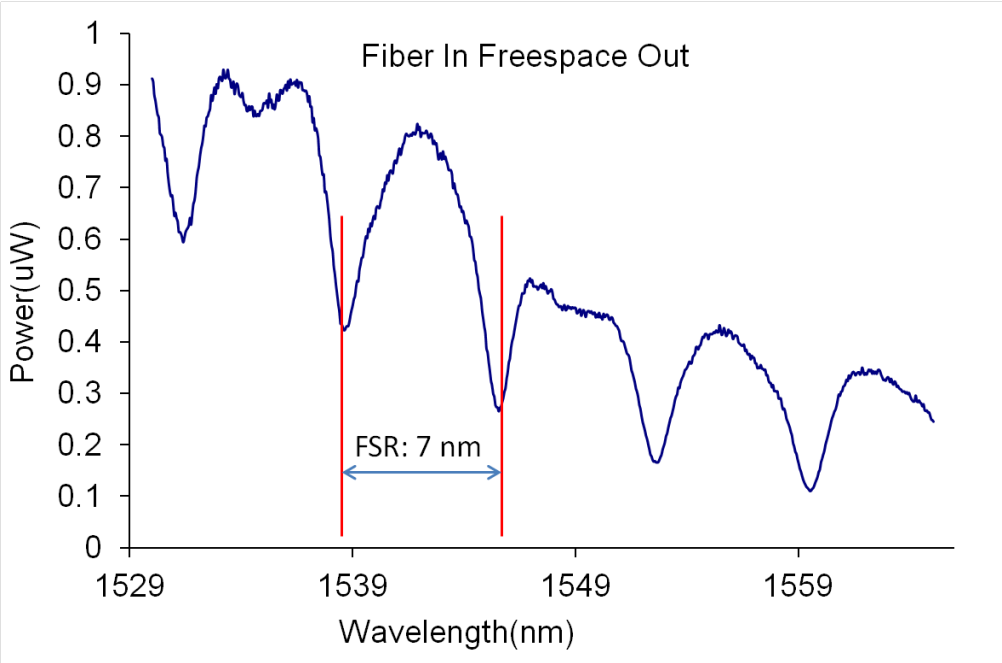

Fig 4. 6 Transmission spectrum of the silicon microdisk.

4.3 Integrated waveguide-resonators

To fabricate integrated waveguide-and-resonators, a critical aspect is the coupling between them. According to simulations, efficient coupling requires the gap between the waveguide and microdisk resonator to be ~100 nm for silicon devices. Achieving such small gap is a major difficulty in the fabrication process.

4.3.1 Achieving small gap

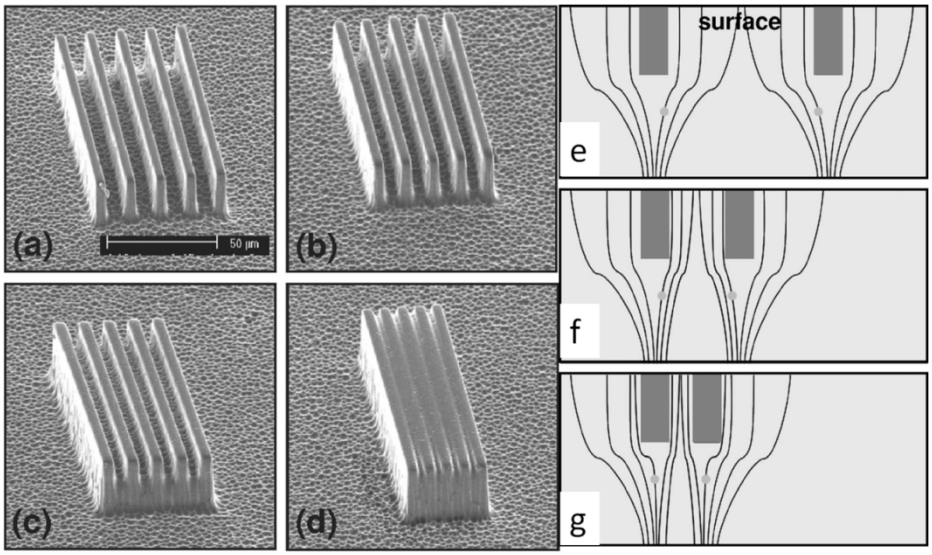

Fig 4. 7 Left: SEM images of proton irradiated lines in a 3 Ω·cm wafer, all 5 µm wide, separated by gaps of (a) 10 µm, (b) 5 µm, (c) 2.5 µm, and (d) 1.5 µm. Fluence of $10^{15}/cm^2$, etched at J =100 mA/cm^2 for 5 min, then PSi removed; and right: Schematic of the E-field lines around two irradiated lines with decreasing gap size. Note the behavior of the dotted E-field line, which moves from inside to outside the gap with decreasing gap size. From [110]

In previous studies, it was found that when the gap between two lines was small, it was not possible to fully etch away the silicon.[110] In Fig. 4.7, the irradiated lines are 5 µm wide and the gaps range from 10 µm to 1.5 µm. The irradiation was done using 2 MeV protons. The large gaps, 10 µm and 5µm, are fully etched, Fig. 4.7(a,b), but the small gaps, 2.5 µm and 1.5 µm, could not be fully etched, Fig. 4.7(c,d). Hence it is difficult to achieve sub-micron gaps. A schematic explanation using the E-field lines is shown in Fig 4.7

(e,f,g). When the gap is big, the E-field lines could easily go through it. As the gap decreases, some of the E-field lines are deflected, and go outside, rather than going though the gap.

To avoid the deflection of the E-field lines, we tried to use a large area irradiation to cover all the surrounding area to prevent the deflection of current, so to force the current to pass through the gaps. Fig 4.8 shows the schematic of this 'forced current' method.

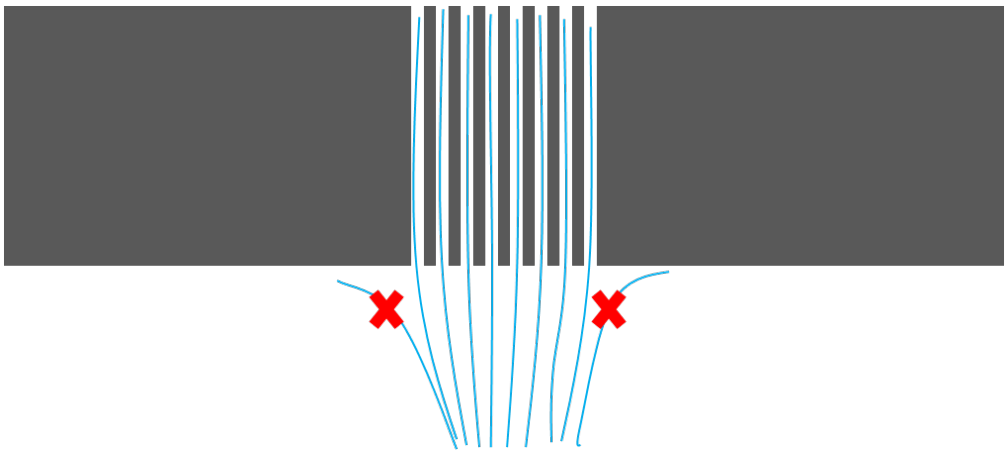

Fig 4. 8 Schematic of the forced current approach to achieving high resolution structures, the black areas are irradiated defect regions, the light blue lines are the E-field lines.

As the surrounding area is overall irradiated, the E-field lines have no other ways to go, but only through the gaps of the irradiated lines.

The supposed fabrication process is schematically shown in Fig 4.9. First, a thick layer (80-160 μm thickness) of SU8 2025 was spin coated on the silicon sample. UV lithography was used to make a square pattern in the center, Fig 4.9(a). The square SU8 pattern stopped the ion beam passing into the silicon at the covered area during large area irradiation, Fig 4.9(b). After that, a thin layer of gold was sputtered on the sample, and then the SU8 was removed in Nano-Stripper. The gold layer was used as an alignment mark to find the square area during subsequent proton beam writing. Proton beam writing should write enough lines to cover the whole square area. After proton beam writing for the fine lines with small gaps, the sample was

electrochemically etched in HF. Finally, the porous silicon was removed in KOH, and the sample annealed in a high temperature tube.

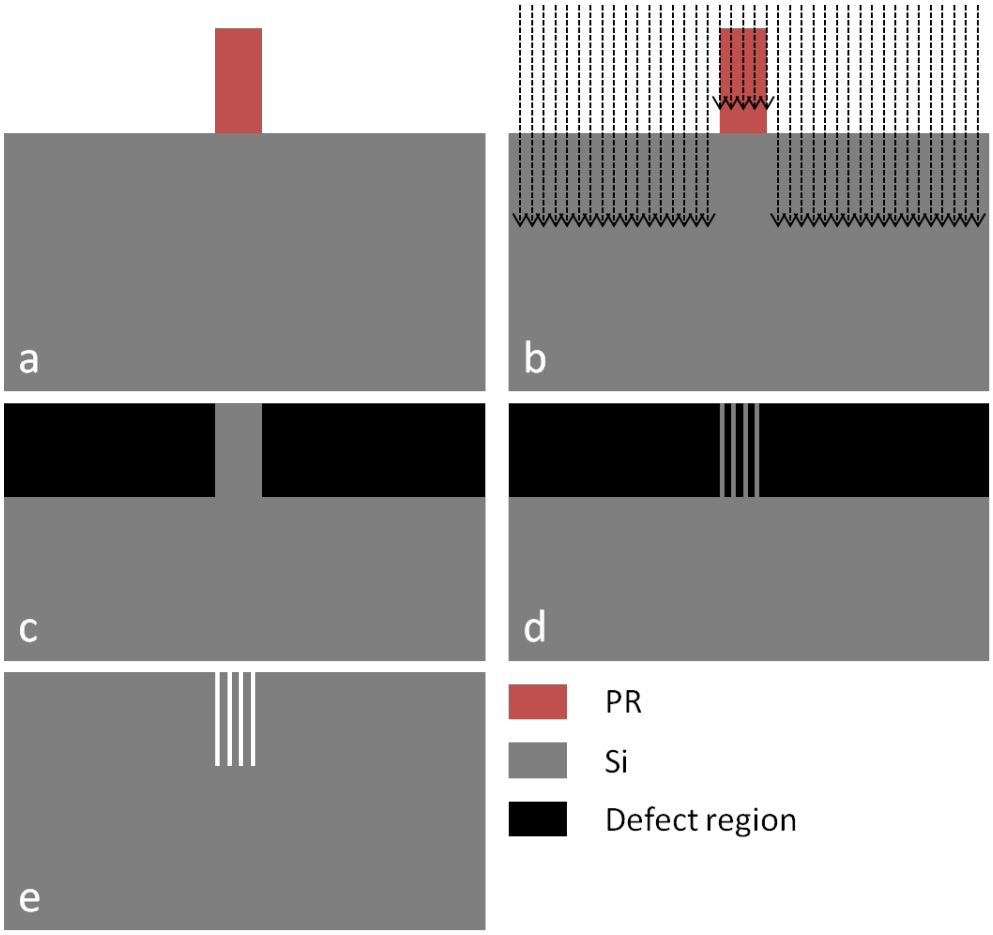

Fig 4. 9 Schematic of the forced current fabrication process, (a) UV lithography for a small area covered with photoresist (PR), (b) large area irradiation, (c) surrounding defect region formed, (d) proton beam writing to write the fine lines with small gaps, (e) final etching and annealing step.

The results, however, were not as predicted, Fig 4.10. The large area irradiation was carried out with 1 MeV protons, and the fluence was 1×10^{16} protons/cm^2. In the 300 µm × 300 µm square, the irradiated lines were with 0.5 µm line width, and the gaps varied from 1 µm to 2 µm. The proton beam writing in the square was carried out with 500 keV protons, and the fluence was 1×10^{15} protons/cm^2. However, after etching, the gaps were not fully etched. This result suggests that, other than the deflection of the E-field lines, there may be some other effect which makes the small gaps unresolvable.

Fig 4. 10 SEMs of the forced current result, surrounding large area: 1×10^{16} protons/cm^2,1 MeV protons, square area: 1×10^{15} protons/cm^2, 500 keV protons, proton beam writing with 0.5 μm line width and 1 μm and 2 μm gaps, (a) overview, (b,c,d) fine views.

We then tried to partially force the current to flow using a modification of this process. Following the same process, during the proton beam writing for the fine lines, we did not write over the whole square area, but only covered a smaller area in the square. In this case, the E-field lines were forced within the square area, Fig 4.11(a). However, the lines did not cover the overall square area, the current was not fully forced through the gaps between the lines, so we called it partially forced current.

The result is shown in Fig 4.11. In Fig 4.11(b), we can see the square area and the fine lines in it. The line width and gaps were the same as described above. Fig 4.11(d) are the same lines with those in (b), but without any force current. Without force current, all the lines were joined together,

only some shallow trace of the 2 µm gaps could be seen from the sidewalls. With a forced current approach, 2 µm gaps were fully etched, but 1 µm ones were still not.

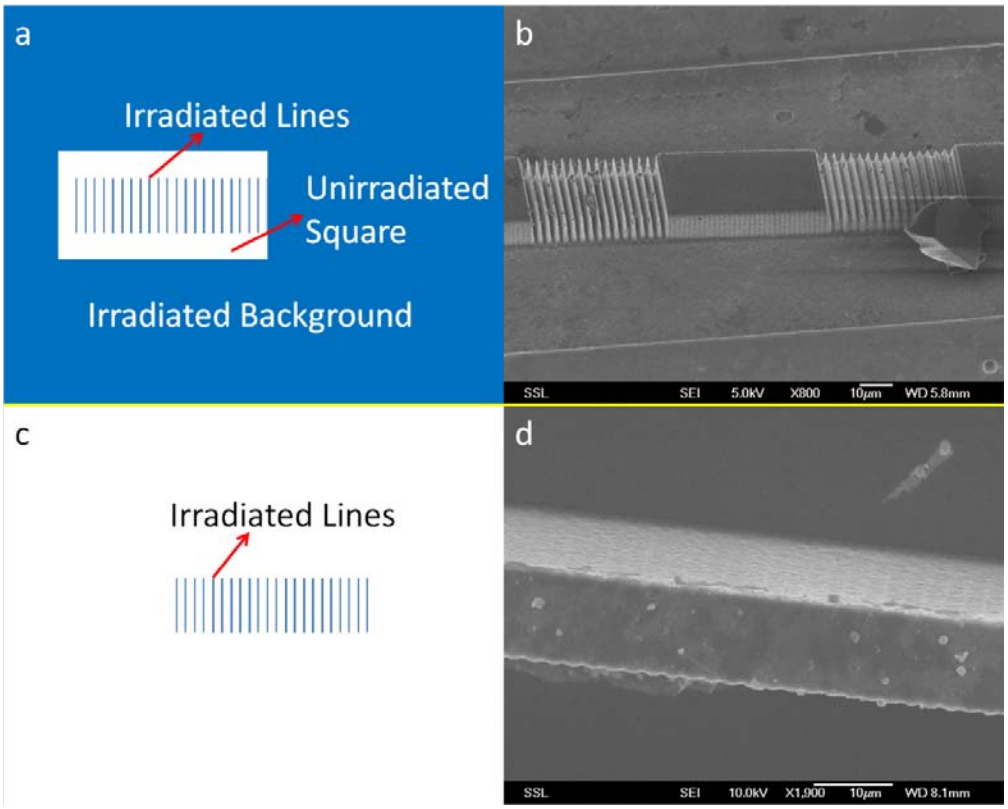

Fig 4. 11 Schematic and SEM results of (a,b) the partially force current, (c,d) lines without force current.

The forced current method should have prevented the deflection of E-field lines, but sub-micron gaps were still not achieved. Therefore, apart from the E-field deflection, there are presumably some other aspects causing the observed behaviour. Another aspect could be the lateral scattering of the ion beam in the material. Fig 4.12(a) shows the huge lateral scattering of 1 MeV protons in silicon. We can see that at the end of range, the lateral scattering has broadened from a point on the surface into ~6-7 µm. In this case, if two irradiated lines were separated by a 1 µm gap at the surface, then their defect

regions would be connected to each other underneath, so the gap could not be etched, which could explain the previous forced current results.

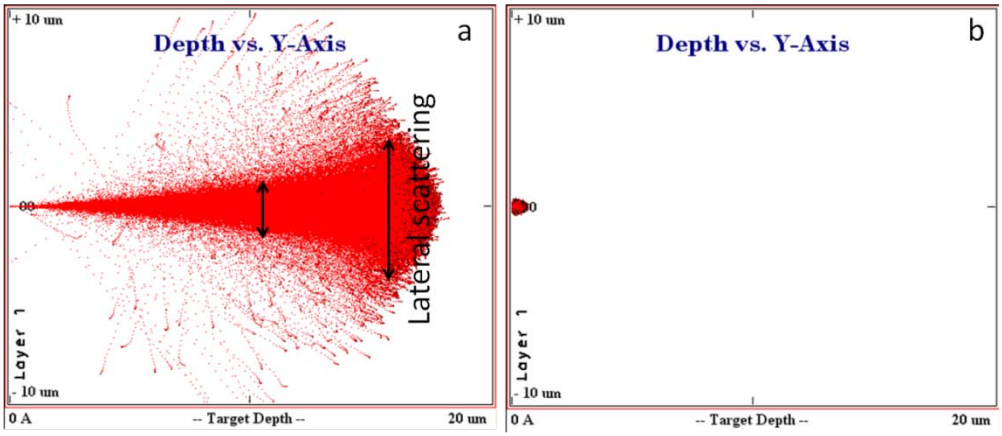

Fig 4. 12 SRIM results showing the ion beam lateral scattering in silicon, (a) 1MeV protons with huge lateral scattering, (b) 50 keV protons with small scattering.

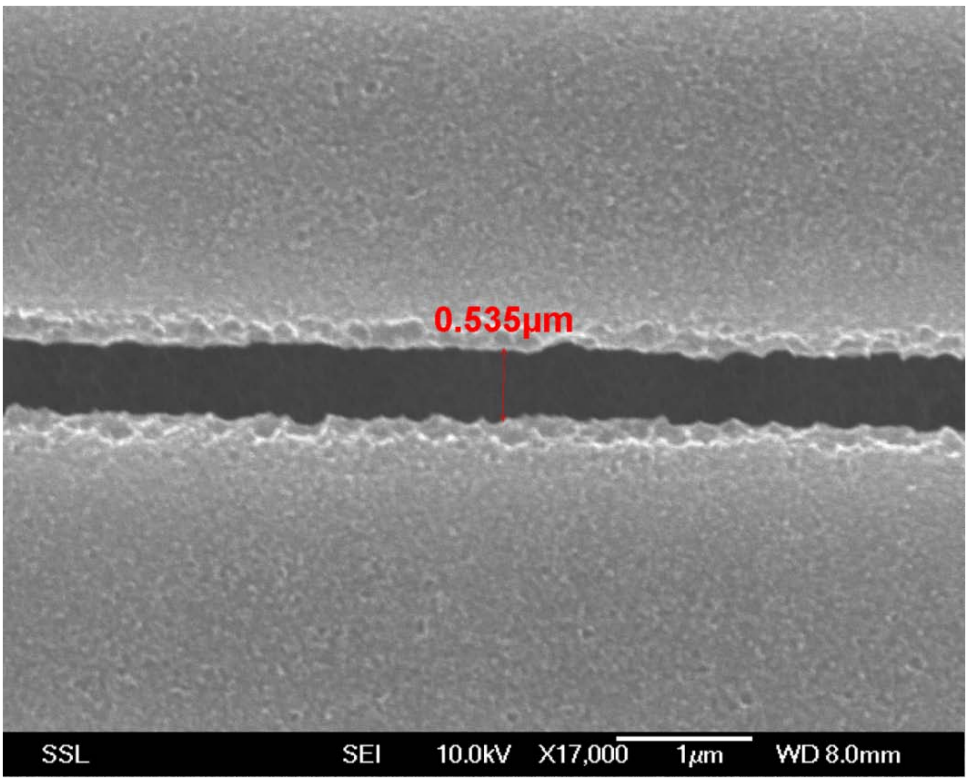

Fig 4. 13 Sub-micron gap achieved with low energy ion beam irradiation.

To avoid the huge lateral scattering of the high energy ion beam, lower energy beam should be used. As shown in Fig 4.12(b), a 50 keV proton beam

has much less scattering, so it can be confined within a sub-micron region. We tried 50 keV protons and had obtained sub-micron gaps as shown in Fig 4.13. UV lithography was used to make photoresist patterns of lines with 2.5 μm width and 1 μm gaps. The large area ion irradiation was carried out with 50 keV protons and a fluence of 1×10^{14} protons/cm^2. After removing the photoresist, and etching, finally, the lines were broadened to ~3 μm wide, and the gaps came out as ~0.5 μm.

In conclusion, to achieve small gaps or fine structures, low energy ion beam should be used for the ion irradiation, since low energy ions have small scattering.

4.3.2 Lithography

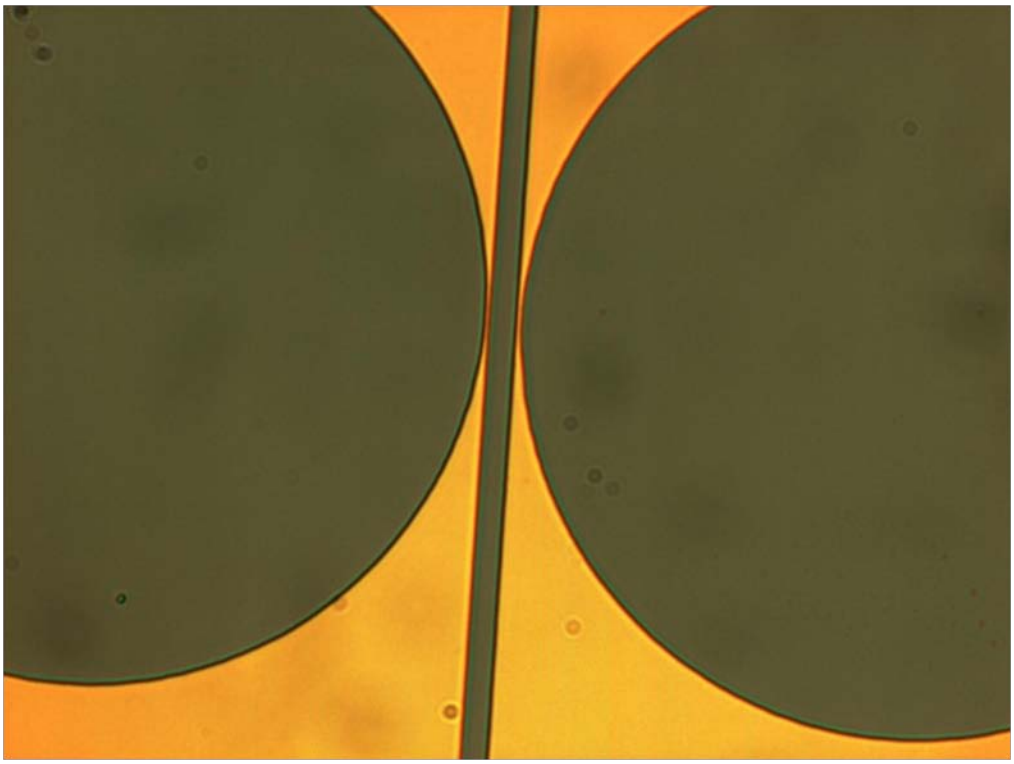

Fig 4. 14 Microscope image of the mask.

There are two ways to pattern silicon via ion beam irradiation, one is to use a focused ion beam to directly write on the sample, the other is to use a UV lithography first to make a photoresist pattern on top of the wafer as an ion irradiation mask, then use a large area ion beam to irradiate the whole surface to transfer the pattern from the photoresist into silicon. As discussed before, to make the waveguide and microdisk single mode, the devices should be thin, thus a low energy ion beam should be used. As a low energy ion beam could produce thin layer structures, it is also beneficial to achieve the small gap between coupled devices. While using low energy ion beam in our accelerator, firstly it is not easy to focus the beam, and then it may not be stable for the focused beam. So, our main aim was to develop the fabrication process using UV lithography combined with the large area irradiation.

Our first attempt used a laser writer to make a chromium mask, then used UV lithography to transfer the pattern onto the photoresist on top of the wafer. Fig 4.14 shows the pattern on the mask. The golden area is the remaining chromium, the grey areas are blank areas. The photoresist used on top of the wafer to be the irradiation mask was AZ 1518. It was spin-coated with a spin rate of 7000 rpm to be ~1.3 μm thick. A thin photoresist was used because it could have a better resolution than thick photoresist in UV lithography, and it was already thick enough to stop a low energy ion beam. However, as the UV light (405 nm) penetrated through the chromium mask, a ~100 nm gap was already beyond the diffraction limit, so not able to be achieved in this way.

To avoid the diffraction limiting the patterned resolution, we then directly used a laser writer to write the pattern on the photoresist. This differs from UV lithography using the mask since direct laser writing writes the disks and waveguides one by one, not as they are exposed at the same time in UV lithography, so diffraction limit was not involved in this case. To optimize the exposure and developing conditions, lines with different widths and gaps were written by the laser writer on the photoresist. Fig 4.15 shows some different conditions of the developed photoresist structures. When the lines were designed very thin (<2 μm), they were difficult to fully develop. Usually, they

could be only partially developed, Fig 4.15(a). As the line width was increased to 2.2 µm, the line was able to be fully developed, Fig 4.15(b,c). However, the lines were not smooth, and their side walls were not straight. The developed bottom width was only ~1.2 µm. The wide lines (>5 µm) could be easily fully developed, and they were smooth and had straight side walls, Fig 4.15(d).

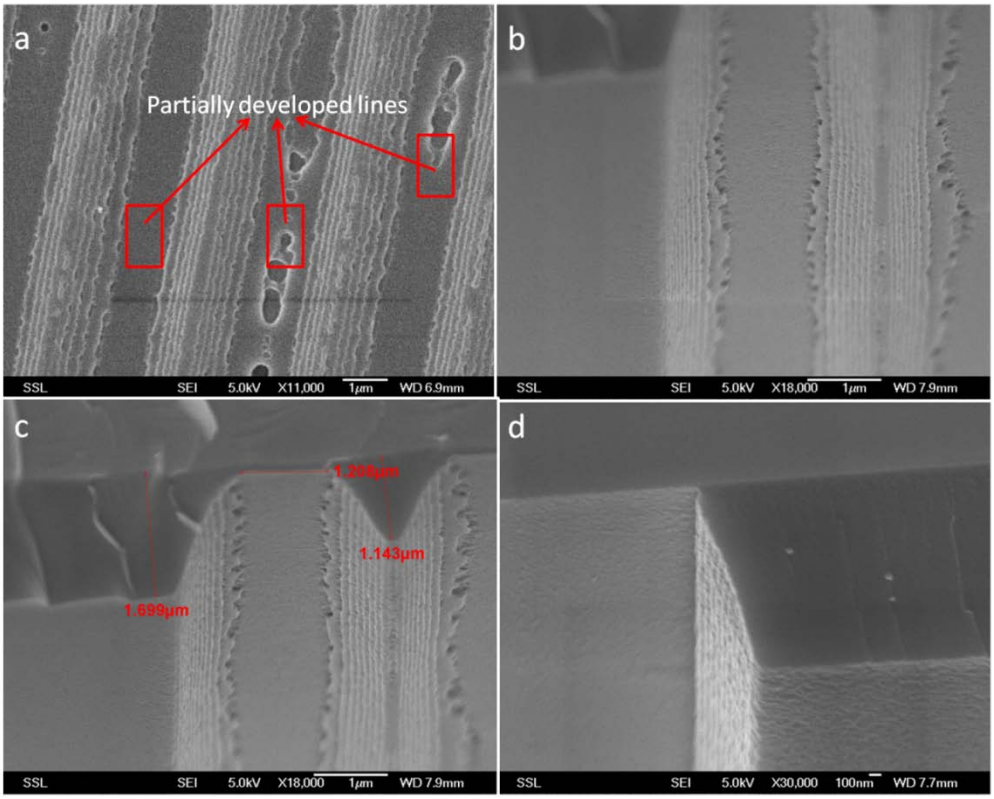

Fig 4. 15 SEM images of the lines on the photoresist, (a) partially developed thin lines, (b,c) fully developed lines, but not smooth, (d) fully developed and smooth wide line.

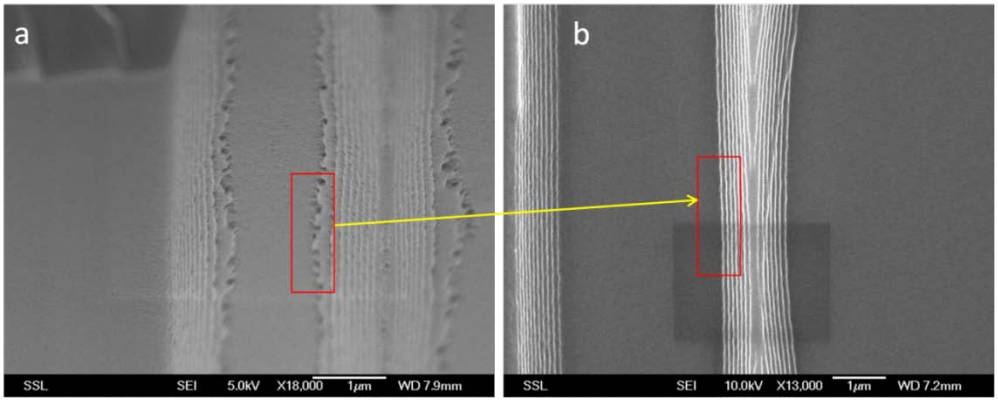

Fig 4. 16 Optimized lithography process to improve the conditions of side walls.

As the lithography conditions were not optimized, the side walls of the structures were very rough, as in Fig 4.16(a). There are three main conditions that can be tuned: exposure conditions of the laser writer, developer proportion, and developing time. For AZ1518, with a spin rate of 7000 rpm for about 1.3 μm thick, an optimized exposure condition was 60 mW × 20%. The developing was carried out in mixture of AZ 400K and de-ionized water with a ratio of 1:2.5 for 20 seconds. With this condition, a much better result shown in Fig 4.16(b) was achieved.

4.3.3 Results

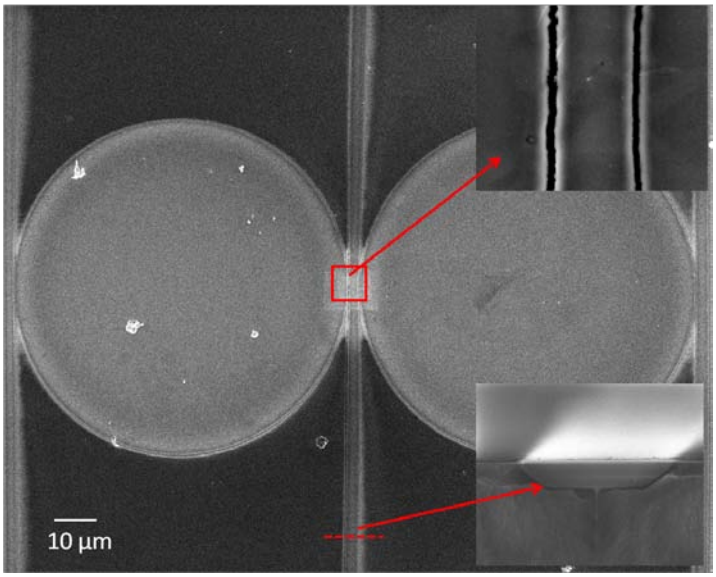

Fig 4. 17 SEMs of the coupled waveguides-and-microdisk resonators, top inset is the fine view of the coupling region, bottom inset is the cross section of the waveguide.

After lithography to produce the photoresist pattern, large area ion irradiation was carried out with 100 keV H_2^+ ions, which is equivalent to 50 keV protons, at the 45° beam line. The irradiation fluence varied from 5×10^{13} to 2×10^{14} proton/cm^2. After irradiation, the sample was electrochemically etched in 24% HF solution for 4 minutes. The porous silicon layer was left in place to provide support for the waveguides. Fig 4.17 shows SEM images of the structure. From the top inset of the figure, we observe a sub-micron gap between the waveguide and micro-disks. The bottom inset is a cross section of the waveguide. The waveguide was designed as 2 μm wide, but in practice its

width came out as about 2.8 µm, probably arising from the broadening during lithography and scattering of the ion beam.

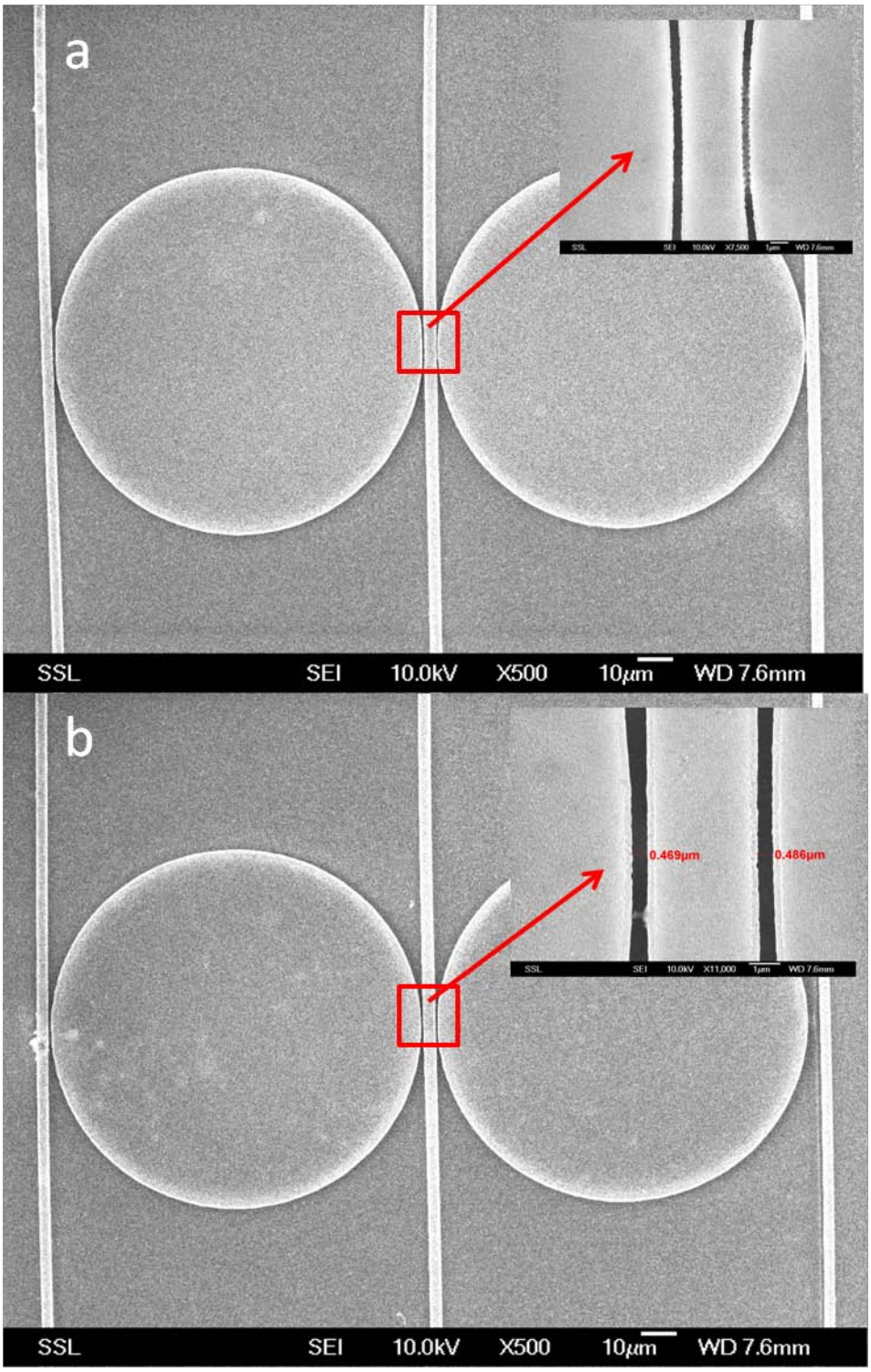

Fig 4. 18 SEMs of the coupled waveguides-and-microdisk resonators, insets show a fine view of the coupling regions, (a) with one of the gaps not fully etched (the right gap in the inset), (b) both gaps fully etched.

We then followed the same process, but during the electrochemical etching step, we carried out two etching steps. The first etching step was one minute to form a layer of ~2.5 μm thick PSi, the sample was then put into diluted KOH solution to remove the porous silicon layer. The second etching step took another 3 minutes for an additional depth of ~7.5 μm. This PSi layer was left in place to support the waveguides. In this case, the waveguides were designed to have a tapered shape with a thin part (2 μm) in the center and wide portions (10 μm) at the ends. Wide waveguide ends may help the waveguides to stand rigidly on the wafer and also make the light coupling from the optical fiber or lens easier. The results are shown in Fig 4.18. When the gap was designed to be small (<0.8 μm), it might not be fully etched, as in Fig 4.18(a). With an increased gap size in the design, the gaps were fully etched, Fig 4.18(b). The actual size was decreased compared to the designed gap of 1 μm, with a measured gap of ~0.48 μm, arising from the scattering of the beam. A tilted view of the structure in Fig 4.19 shows the 3D effect that the waveguides and microdisks are floating over the

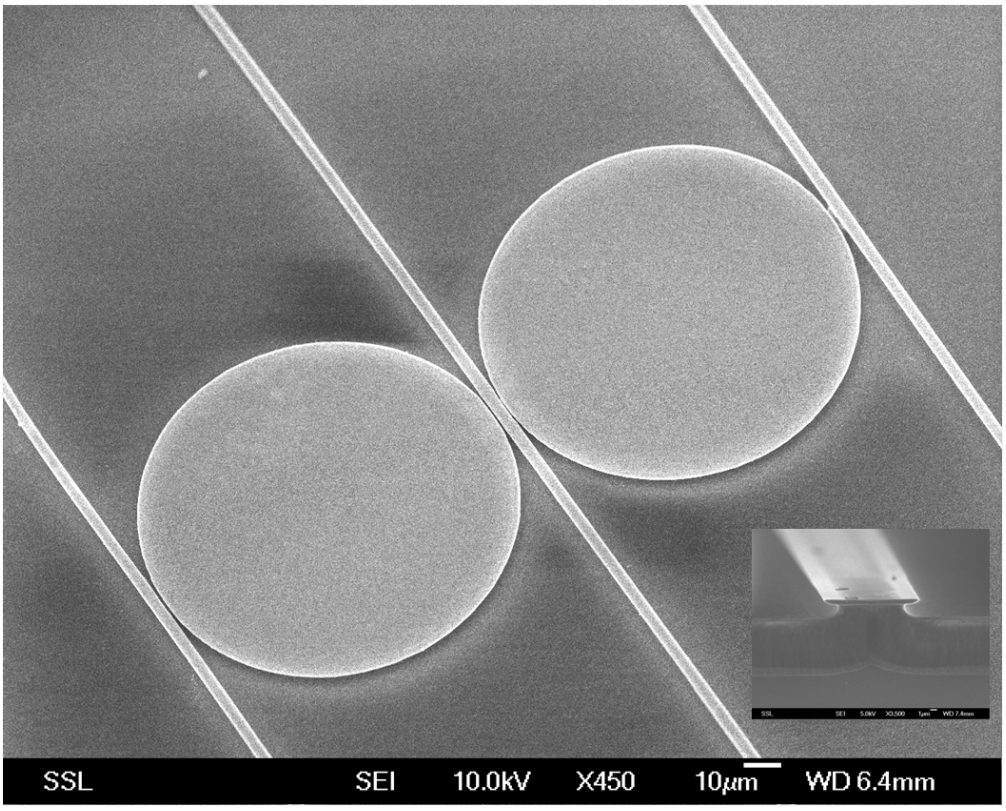

Fig 4. 19 Tilted view of the structure and the waveguide cross section in the inset.

wafer surface.

Besides microdisk resonators, microring resonators were also fabricated. Fig 4.20 shows an integrated waveguide-and-microring. The outer ring was supported by six spokes from an inner circle. The radius of the inner circle support was 20 μm, the outer radius of the ring was 40 μm. The width of the spokes and ring was designed to be 2.5 μm, but in practice was ~4 μm. Irradiation was carried out with 1×10^{14} ions/cm^2, 200 keV He^+ ions. For He^+, this high fluence resulted in the designed gaps of 1.8 μm not being fully etched, as shown in Fig 4.20(a). After ion irradiation, the sample was

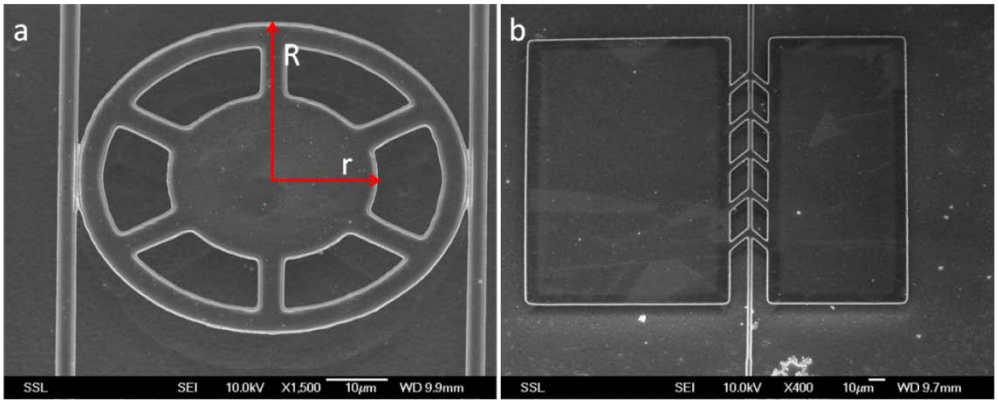

Fig 4. 20 (a) Integrated waveguides and micro-ring, the radius of the inner circle support r=20 μm, the outer radius of the ring R=40 μm, (b) support of the waveguide.

electrochemically etched with current density of 60 mA/cm^2 for 4 minutes, then the PSi layer was removed in diluted KOH solution. As the rings were supported by the spokes from the inner circles, the waveguide were also supported by spokes from additional square supports, as shown in Fig 4.20(b).

4.3.4 E-beam patterns

Because of the limitation of normal UV lithography, it was difficult to obtain fine photoresist patterns using it, especially for achieving small gaps. So e-beam lithography was used to achieve small gaps and thin waveguides. The smallest waveguide width that could be achieved by normal UV lithography

was ~3 μm, which is too thick for single mode light. E-beam lithography can easily achieve submicron line widths and gaps.

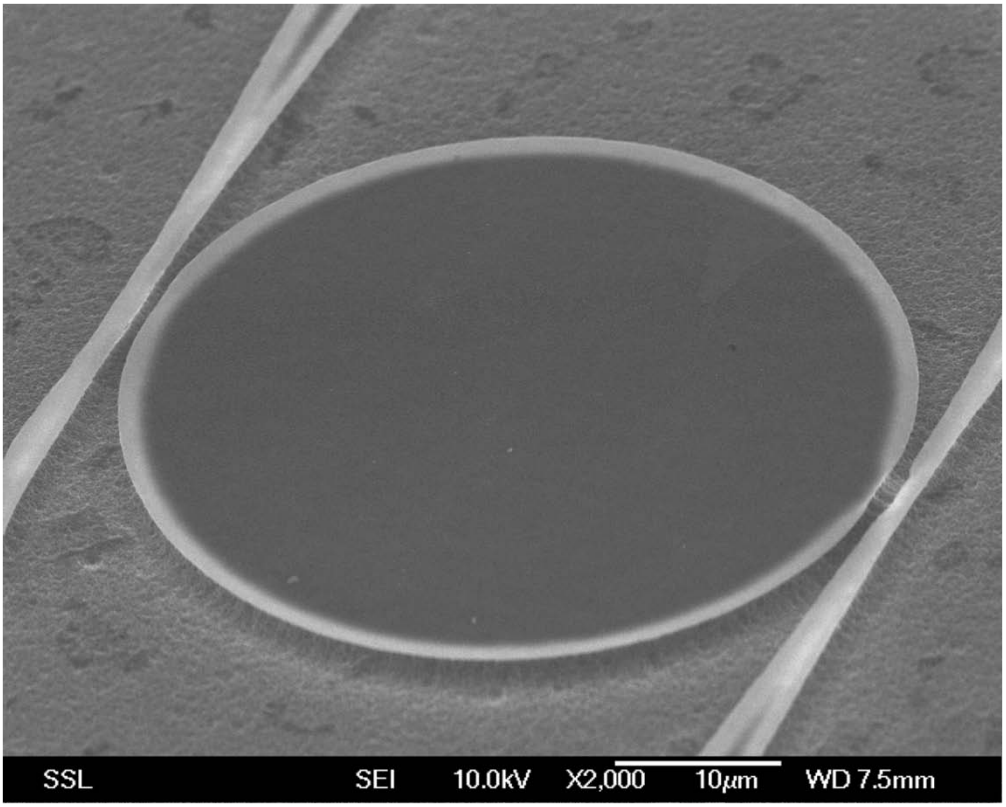

Fig 4. 21 Integrated waveguides and microdisk patterned by e-beam lithography.

Fig 4.21 shows a result of integrated waveguides and a microdisk resonator, which was patterned by e-beam lithography instead of UV lithography, before ion irradiation. The waveguides were designed to have a tapered shape with a thin center part at the coupling region. The center part was designed to be 0.5-1 μm, while the ends were designed to be 10 μm. The gaps between the waveguides and microdisks were designed to be 0.4-0.7 μm. 100 keV H_2^+ ions were used for the ion irradiation to a fluence of 1×10^{14} protons/cm^2. The sample was etched with a current density of 60 mA/cm^2 for 1 minute.

E-beam lithography achieved fine structure patterns on the photoresist, especially for the small waveguide width and gap. However, when the pattern

was transferred from the photoresist into silicon by ion irradiation, the small gaps were not fully etched. As in Fig 4.22, the gap disappeared, Fig 4.22(a) when the designed gap was 0.4 μm. As the gap increased to 0.5 μm in the design, the gap appeared in the silicon structure, but not fully etched, Fig 4.22(b).

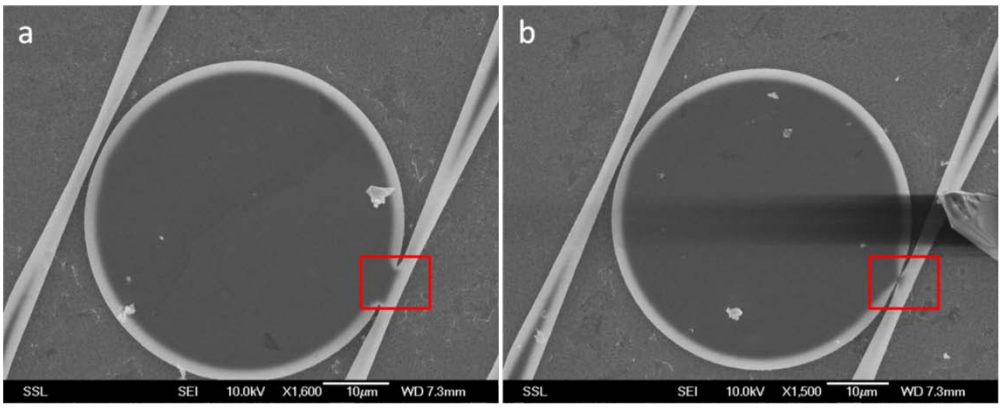

Fig 4. 22 Integrated waveguides and microdisk patterned by e-beam lithography, (a) waveguide and microdisk totally connected (in the red square), (b) the gap is not fully etched.

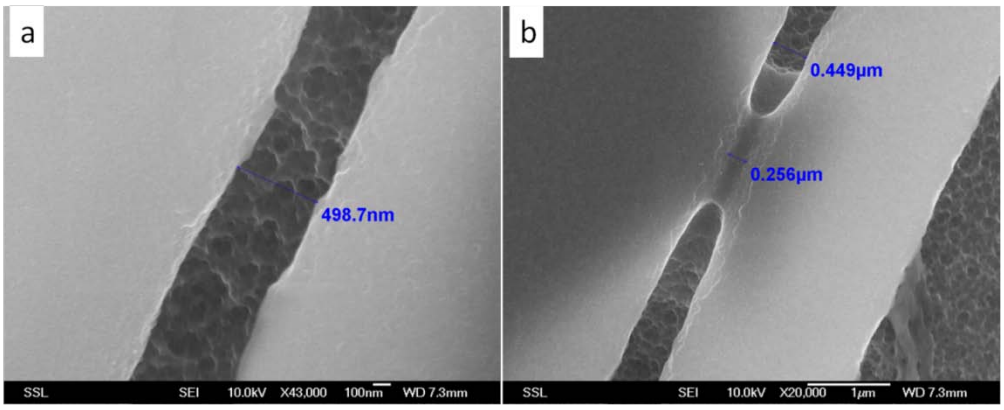

Fig 4. 23 Gaps in high magnification, (a) gap fully etched, (b) not fully etched.

Fig 4.23 shows high magnification views of the coupling regions. When the designed gap was 0.6 μm, it could be fully etched in silicon devices, and came out as ~0.5 μm, Fig 4.23(a). As the gap was decreased to 0.5 μm in the design, it could not be fully etched, Fig 4.23(b). And according to the figure, a minimum gap that could be fully etched was ~0.45 μm, smaller gaps

disappeared. Use of even lower ion energies and fluences may achieve smaller gaps. However, 50 keV protons are the lowest energy we can produce in our accelerator at present, and a fluence of 1×10^{14} protons/cm^2 is already quite low, fluences lower than that would make the structure fragile and rough.

In conclusion, silicon microdisk resonators were fabricated on bulk silicon wafers with ion beam irradiation followed by electrochemical etching. Though the optical characterization result was not good, with a low Q value, it could be further optimized by lithography and ion irradiation with higher fluence.

To achieve integrated waveguide-and-resonator, a forced current method was carried out to obtain the small gap for efficient coupling between waveguide and disk. The result showed that a forced current helped a little in achieving small gaps, but the gap limitation still stayed over 1 μm, which is probably because of the lateral scattering of the ion irradiation in silicon. Instead, the gap could be easily reduced to submicron by using a low energy ion beam, since lower ion beam irradiation has smaller lateral scattering.

E-beam lithography could make much better patterns than normal UV lithography with smaller gaps and smoother photoresist structures. However, the smallest gap which could be achieved using ion beam irradiation patterning on silicon was 400-500 nm, much more than the efficient coupling gap of ~100-200 nm for silicon devices. This is mainly limited by the lateral scattering of the beam. This limitation may be further reduced by using a lower ion beam energy than 50 keV and lower ion irradiation fluence. But they would also make the structures more fragile and rough. Thus this process may not be a good choice to achieve lateral integrated photonic structures.

Chapter 5

Flexible Polarization Y-shape Splitters

5.1 Introduction

A beam splitter is an optical device that splits a beam of light in two. In general optics, its common form could be a cube, a half-silvered mirror, a dichroic mirrored prism. It is the crucial part of most interferometers. Regarding on-chip photonics, a beam splitter is usually a component with one waveguide input and two waveguide outputs. According to their functions, there are mainly two types:

1. Optical power splitters which simply split an incident light beam into two outputs equally; [111] [112]

2. On-chip polarization splitters which can give polarization dependent outputs.[113-116]

Optical power splitters are one of the fundamental components in integrated optical systems[117, 118]. They are critical in creating modulators[119], interferometers[120] and (de)multiplexers[121].

On-chip polarization splitters are key components of integrated photonic circuits that consist of polarization dependent devices[122]. Photonic integrated circuits are usually polarization dependent, while a single-mode fiber does not preserve the polarization. To overcome this problem, one approach is to manipulate the polarization on the chip, in which, components optimized for one certain state of polarization can be used to optimize the performance. Polarization splitters are the key components in this approach. It

is based on modal birefringence: the propagation constants of the higher order modes differ significantly for TE and TM polarizations.

Passive polarization splitting is preferred over active splitting to minimize power consumption and to avoid the need for tuning. There are two categories of passive polarization splitters: mode-evolution-based[123] and interference-based splitters[113, 124]. Interference-based passive polarization splitters provide low-loss operation and high polarization splitting ratio and can be designed for single etch step fabrication[124]. They have been demonstrated utilizing either directional couplers[114] or multimode-interference couplers[113].

There are symmetric and non-symmetric directional couplers. Symmetric directional coupler-based polarization splitters are usually quite long. They can be shortened to ~100μm by reducing the gap between the coupler waveguides.[125] However, this will also degrade the tolerance of the device fabrication. A small variation of the structure size would affect the splitting ratio significantly. Non-symmetric directional couplers can be designed to allow only one of the modes to couple out of the input waveguide, and have an improved fabrication tolerance by tapering the waveguides. However, this also requires a long coupling length (~1500μm) to obtain efficient coupling as it needs a large gap.[124]

Multimode-interference couplers can split TE and TM polarizations into different output waveguides using the difference in their self-imaging beat-lengths, $L_\pi = \pi / (\beta_0 - \beta_1)$, where β_n is the *n*th mode propagation constant supported by the multimode section[126]. In order to reduce the length of the coupler, four-mode, or even further more, two-mode interference couplers can be used.[127, 128] The length can be as short as several microns[128] or even sub-micron[113].

5.2 Y-shape splitter simulations

In multimode-interference based polarization splitters introduced above, the input is usually a single mode waveguide, and multimode-interference only

appears at the connection part, or say, the coupling part. In this chapter, the Y-shape splitters which are studied have similar polarization behavior and also use multimode-interference. However, differing from the multimode-interference based polarization splitters introduced above, the Y-shape splitters have multi-modes through the whole pathway, from the input to outputs.

The RSoft code[129] was used to perform the simulations. To start, we considered a 2D situation for easy simulations. With a multimode waveguide input, the light power stays constant along the straight input waveguide, but when it enters the angled arms, the launch power starts oscillating along the pathway, and then becomes constant when it comes back into a straight end.

Fig 5.1 shows a typical simulation result of a Y-shape silicon splitter with a width of 5 μm along the whole pathway (input and output ports), and an arm angle of 5˚. The incident light is set at a wavelength of 1.55 μm and a TE mode. The left of the figure shows a schematic of the splitter and color map of the power. It is a Y-shape splitter, with one straight input and two outputs both at an angle of 5˚. The splitting starts from a location of 300μm along the Z axis, and the right arm comes back to a straight waveguide at position of 1230μm along the Z axis. So the right arm has a Z axis-length of 930μm. We can see the color variation along the two arms which means the power oscillates along them. We chose the right arm as the monitor pathway, and obtained the monitor value along it. The center of the figure shows the monitor value along the right arm pathway. The value uses the input power as the normalized value 1. So for example, when its value is 0.4, it means it is 40% of the input power. We can clearly see there is a significant periodic oscillation of the power along the pathway which is caused by the multimode interference. An ideal two-port-splitter would give a maximum monitor value of 0.5 along each arm. However, the maximum value in this case is only ~0.45. This is because the angle 5˚ in this case is too big to confine all the light into the two arms at the splitting point. We chose 5˚ since it was able to give us a significant power oscillation from 0 to 0.45 to fulfill a perfect polarization behavior. The monitor value reaches a constant level when the arm comes

back to a straight waveguide end. So we can vary the length of the arm to vary the output.

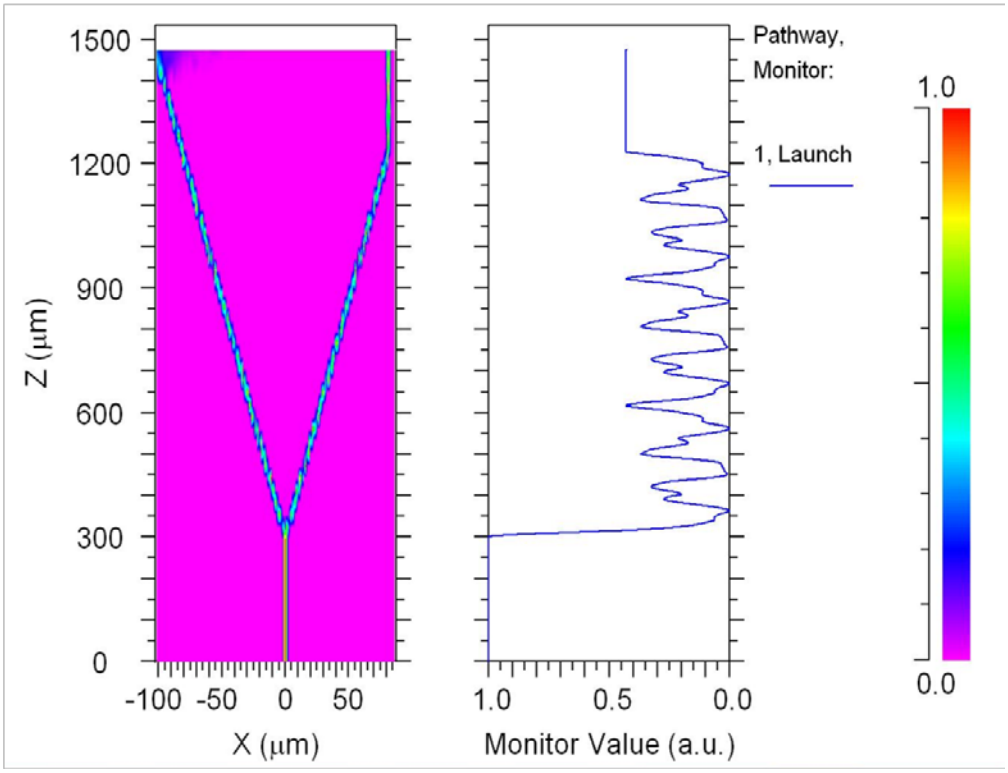

Fig 5. 1 Simulation results of a Y-shape splitter with width 5μm, arm angle 5˚, the incident light is 1.55μm wavelength, TE mode: left shows a schematic of the splitter and color map of the power distribution; the center is the monitor value along the right arm; the right is a color scale bar of the power strength.

5.2.1 TE and TM oscillations

Both TE and TM modes behave similarly with periodic power oscillating along the arms. However, their associated periods are different, which makes the multimode Y-shape splitter to be able to perform polarization selections. Fig 5.2 shows the power oscillations of TE and TM modes along the angled arm. In the beginning, the two modes oscillations are almost synchronized. Then they become separate as they progress further along the arm since their oscillating periods are slightly different. From the figure, we can see that the TE mode has a slight bigger period than the TM mode. Hence we can choose a different arm length to give a TE or TM output through that arm. For example, we can choose Z_1 and Z_3 arm lengths to give out TM mode outputs, or Z_2 and

Z_4 to give out TE mode outputs. Actually, we can see that there are many arm lengths to choose to give TE or TM outputs with different polarization ratio. At Z_5 and Z_6, we can even obtain totally TE or TM polarized outputs.

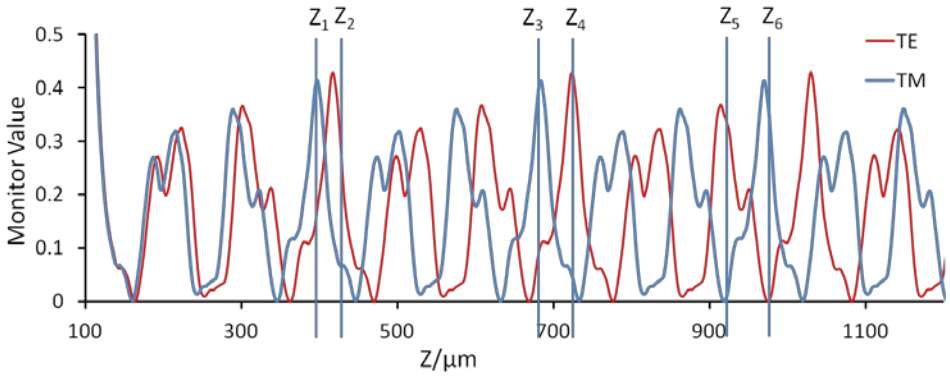

Fig 5. 2 Simulation results of a Y-shape splitter with width 5μm, arm angle 5°, the incident light is 1.55μm wavelength, red for TE mode, blue for TM mode.

5.2.2 Different wavelengths

Different polarizations have different oscillating periods. Similarly, different wavelengths also have different oscillating periods. For example, as shown in Fig 5.3, the arm length

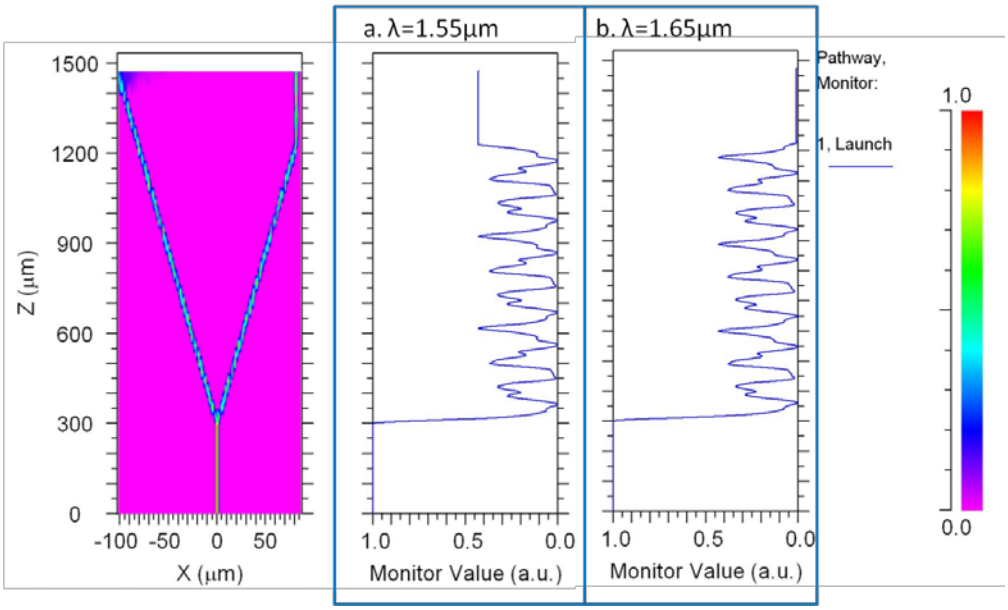

Fig 5. 3 Simulation results of a Y-shape splitter with width 5μm, arm angle 5°, length 930μm, the incident light is TE mode, (a) 1.55μm wavelength gives a maximum output; (b) 1.65μm wavelength gives a minimum output.

is 930 μm along the Z axis. With the same arm angle and length, while an incident light gives out a maximum output with 1.55 μm wavelength, it gives out a minimum with a 1.65 μm wavelength.

We studied a series of incident light with different wavelengths into a 5° Y-shape splitter with waveguide width of 5μm. The results are shown in Fig 5.4. The splitting starts from

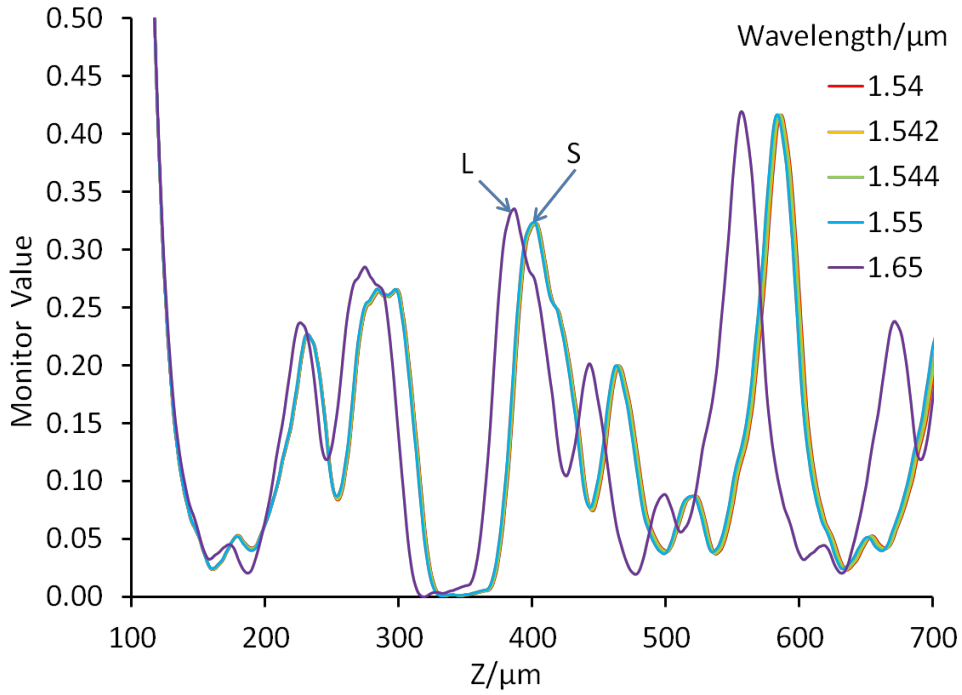

Fig 5. 4 Simulation results of a Y-shape splitter with width 5μm, arm angle 5°, within a length of 100-700 μm, the incident light is TE mode, with a series of wavelengths: 1.54, 1.542, 1.544, 1.55, 1.65 μm. The splitting starts at Z=100 μm.

Z=100 μm. We can see that, within the beginning 600 μm length, the oscillations of λ=1.54, 1.542, 1.544, 1.55 μm incident light are almost synchronized. From 1.54 μm to 1.55 μm, it is a 10 nm band width. If the wavelength changes a lot, from 1.55 μm to 1.65 μm, with a 100 nm variation, the oscillations along such a length would differ significantly as shown in the figure. Incident light with longer wavelengths have shorter power oscillating period along the Z axis. For example, the third peak of 1.65 μm wavelength is at Z=385 μm (L), and that of 1.55 μm wavelength is at Z=402 μm (S). They have a difference in distance of ~17 μm along Z axis. Higher order peaks

would differ even more. For example, if it goes further to a length of ~4 mm, the oscillation of 1.65 μm wavelength is totally out of the step of that of 1.55 μm wavelength, as shown in Fig 5.5.

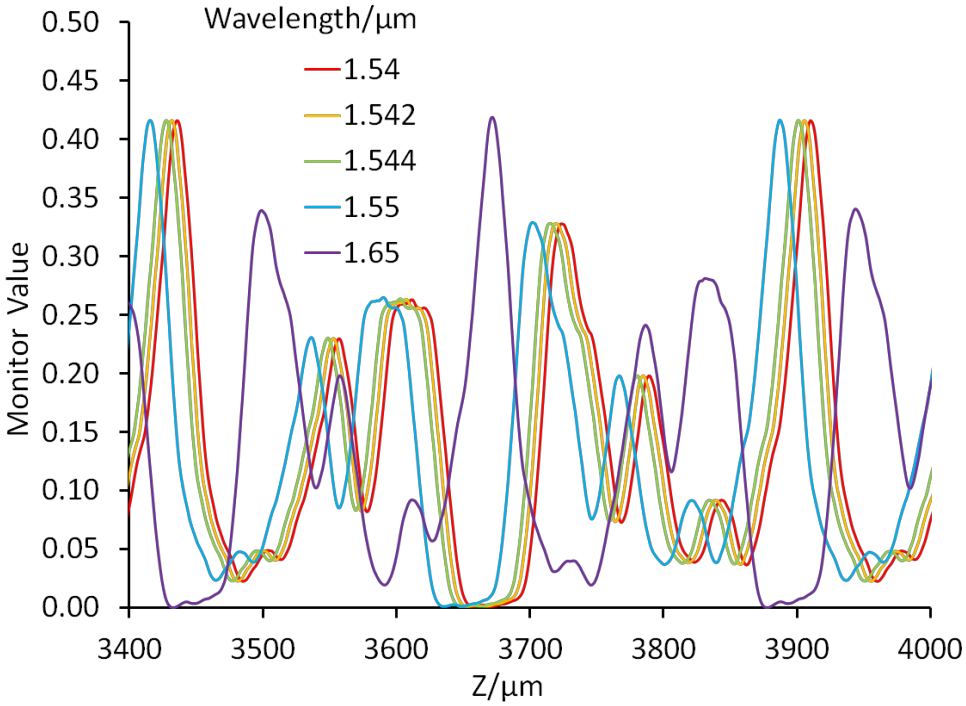

Fig 5. 5 Simulation results of a Y-shape splitter with the same settings as in last figure, showing Z axis from 3300-4000 μm.

Even with a small wavelength variation of 10 nm, from 1.54 to 1.55 μm, the oscillation shift becomes significant. The labeled peak of 1.55 μm wavelength (L) is at Z=3887 μm, while the same peak of 1.54 μm wavelength (S) is at Z=3910 μm, with a distance of ~13 μm.

5.2.3 Different waveguide widths and arm angles

Similarly, when the waveguide widths of the Y-shape splitters are different, the power oscillation period along the arm would be different. Fig 5.6 shows the simulation results of the Y-shape splitters with an arm angle 5˚, and width 5 μm which is in blue, and 5.15 μm in red. The incident light has a wavelength of 1.55 μm, TE mode. We can see that a wider waveguide would give out longer period along the Z axis. Around Z=600 μm position, the red third

maximum peak shift ~28 μm to the right side of red peak, as marked in the figure. This may suggest a tolerance of the width during fabrications.

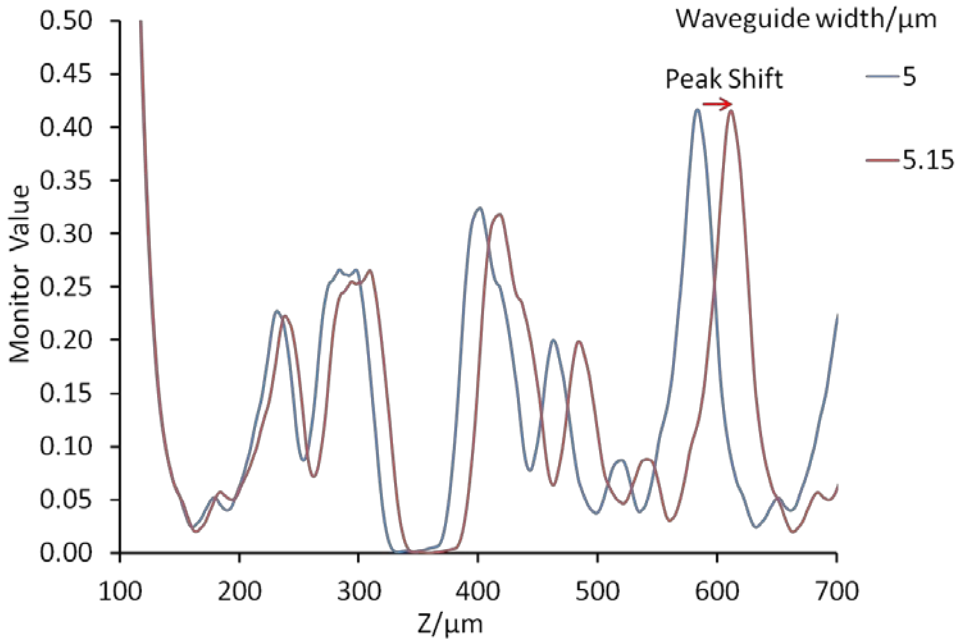

Fig 5. 6 Simulation results of a Y-shape splitter with width 5 μm in blue, 5.15 μm in red, arm angle 5˚, the incident light is 1.55μm wavelength, TE mode.

According to the simulations above, to achieve totally polarized outputs at a wavelength of ~1.55 μm, the length of the arms should be at least about 250 μm, when the widths of the waveguides are ~5μm. This is quite long, because the oscillation period is long in this case.

To further reduce this limit, we can use reduce the width of the waveguides to obtain a shorter power oscillation period. As shown in Fig 5.7, such a Y-shape splitter would give out a smoothly oscillating behavior with a much shorter period than that of a 5 μm width. However, it is not able to perform a fully polarized output with an arm angle of 5˚. With a waveguide width of 2 μm, the arm angle should be at least ~10˚ to achieve a fully polarized output. Furthermore, when the width of the waveguide is reduced down to 1 μm, the angle should be ~20˚ to achieve full polarization. The period is also reduced a lot. In this case, the arm length could be only ~10 μm to achieve full polarization, Fig 5.8.

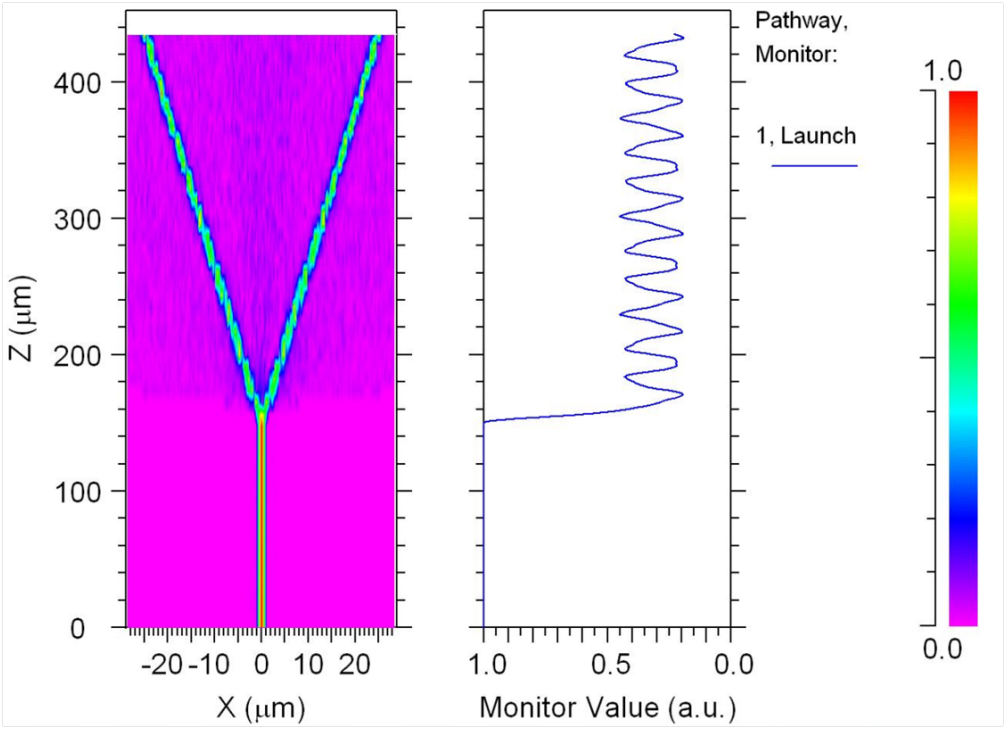

Fig 5. 7 Simulation results of a Y-shape splitter with width 2μm, arm angle 5˚, the incident light is 1.55μm wavelength, TE mode.

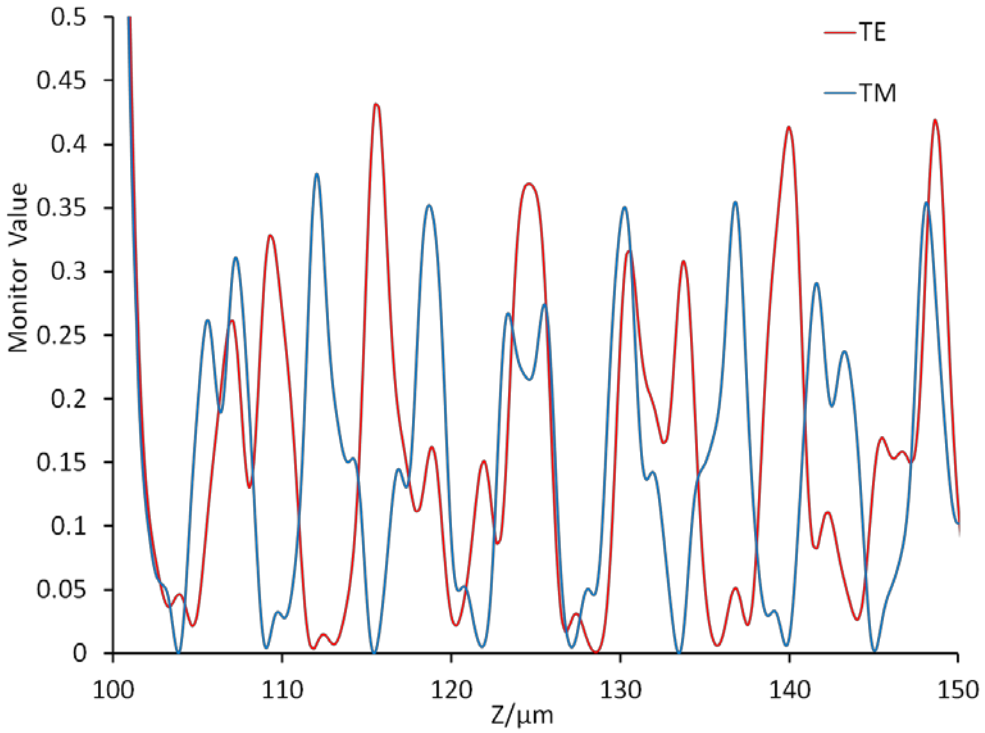

Fig 5. 8 Simulation results of a Y-shape splitter with width 1 μm, arm angle 20˚, the incident light is 1.55μm wavelength, TE mode in red, TM in blue.

5.2.4 Summary

To summarize, there is a power oscillation based on multimode-interference along the arms of multimode Y-shape splitters. The oscillation is periodic, and the period depends on the polarization mode and wavelength of the incident light, and the width of the waveguides:

1. TE mode has longer period than TM;
2. Shorter wavelength gives a longer period;
3. Smaller waveguide width gives a shorter period.

According to these, Y-shape splitters could be either polarization or wavelength selective by making the arm with a certain width and length. TE and TM modes differ significantly at the beginning of the power oscillations. Thus we can choose a short arm length to achieve a polarization selective splitter. Small variations of incident light wavelength would not shift the power oscillations significantly. They stay almost synchronized at the beginning of the oscillations. So Y-shape splitter with short arms could be a relatively broad band polarization splitter. And to achieve a sensitive wavelength selective splitter, the splitter arms should be long enough to release a significant output power difference for wavelengths with small deviations. To reduce the length of the polarization splitters, smaller width of the waveguides could be applied.

Furthermore, to achieve full polarization, the arm angle should be big enough. This angle limitation mainly depends on the width of the waveguides. For example, while a waveguide width of 5 μm would require a minimum arm angle to be ~5˚, a width of 1 μm would require ~20˚ to achieve fully polarized outputs.

5.3 Fabrication of Y-shape splitters

The fabrication of Y-shape splitters on bulk silicon wafer is very straight forward. A schematic of the fabrication process is shown in Fig 5.9. Firstly, the Y-shape splitter pattern was patterned using standard UV lithography on a ~6 μm thick AZ 9260 photoresist spin coated on 0.3 Ω·cm p-type silicon wafer,

Fig 5.9 (a). The wafer surface was then irradiated with a large area beam of 200 keV protons, which have a range of ~2.1 μm in silicon. And the photoresist is thick enough to stop the beam going through it 3

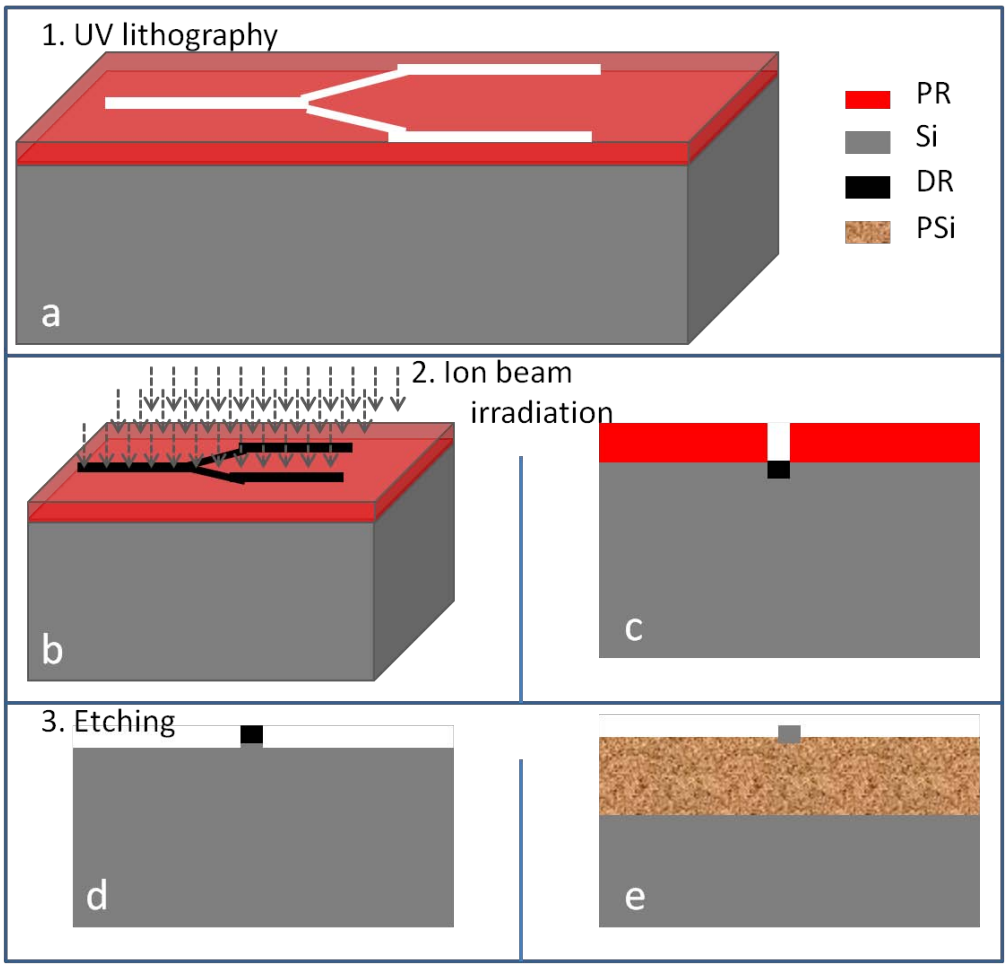

Fig 5. 9 Schematic of the fabrication process: (a) the first UV lithography step to make the splitter pattern on photoresist (PR); (b,c) the second ion beam irradiation step to transfer the pattern in PR into silicon wafer, (c) is the cross section view cut from the yellow dashed line in (b); (d,e) cross section view of the last etching step, (d) the first etching step with porous Si (PSi) removed, (e) the second etching step with PSi remaining as the support, and the defects annealed.

into the silicon wafer at the regions covered by it. So defects were only created at the Y-shape region where it was exposed to the ion beam. The irradiation fluence was ~2×10^{16} ions/cm^2, high enough to stop PSi formation. After removing the photoresist, the wafer was electrochemically etched in 24% HF with a current density of 60 mA/cm^2 for ~1 minute to make a porous silicon layer of ~ 2.4 μm thickness. Then the porous silicon layer was removed in a

KOH solution, and the wafer was electrochemically etched for the second step with a current density of 40 mA/cm^2 for 4-5 minutes to make a porous silicon layer of 6-8 μm thickness. A lower current density was used in the second etching step because it could produce smaller pores which make the porous silicon layer more stable. Finally, the wafer was annealed and thermal oxidized in air at 1000˚C for 10 hours. The width of the splitter waveguides was designed as 5 μm, and the arm angle was 5˚.

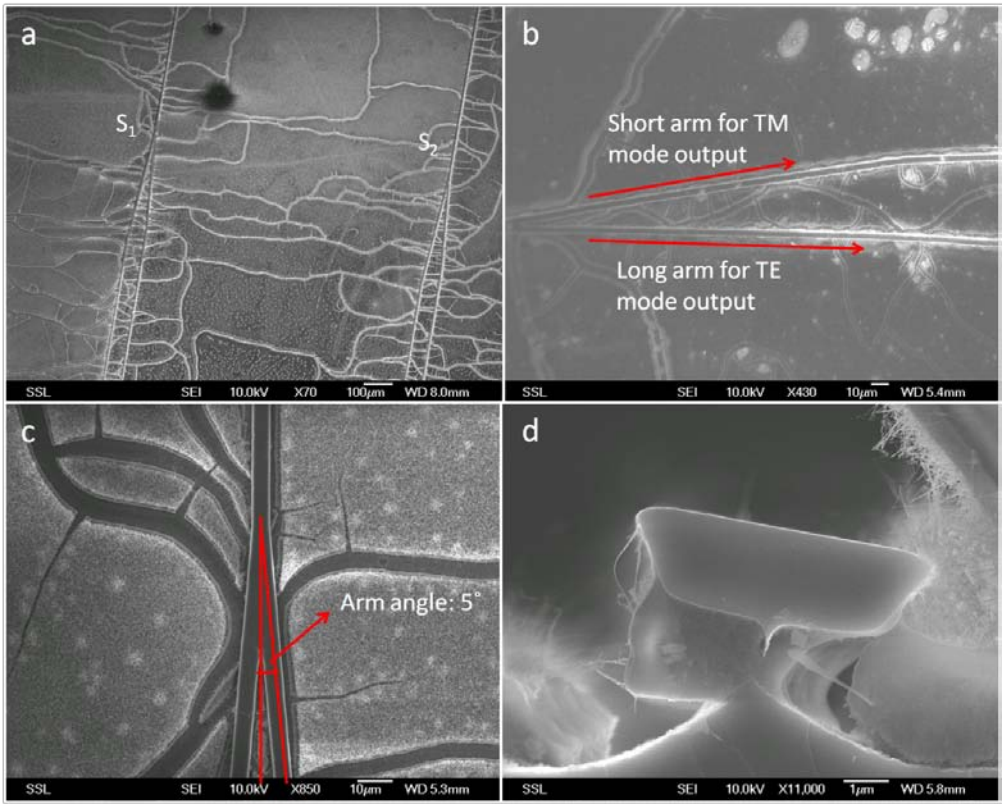

Fig 5. 10 SEMs of the Y-shape splitters: (a) overview of two splitters; (b) the two arms, shorter for TM mode output, longer for TE mode; (c) the splitting point; (d) cross section of the input waveguide.

Fig 5.10 shows SEM images of the fabricated Y-shape splitters on bulk silicon. A series of 9 splitters with a step arm length of 5 μm were fabricated on one wafer. The differences of the short and long arms were set as 50 μm. We numbered the 9 splitters from S_1 to S_9. Fig 5.10 (a) shows S_1 (short arm: 293 μm, long arm: 343 μm) and S_2 (short arm: 298 μm, long arm: 348 μm). We set the two arms of each splitter with a difference of 50 μm, because with

such a waveguide width, the splitting of TE and TM maximums is with a length difference of ~50 μm and the first splitting starts at a length of ~300 μm according to simulations. Fig 5.10 (b) is a slightly magnified image of the two splitters of S4. We were supposed to obtain a TM mode output from the short arm and TE from the long. Fig 5.10 (c) shows a further magnified image at the splitting point. The splitting angle was 5° as shown in the figure. A cross section view of the input waveguide is also shown is Fig 5.10 (d). The width is ~5 μm, and the thickness is ~2 μm. The sample was etched to a depth of ~2 μm at the first etch step, and porous silicon was removed in KOH. Then the sample was etched again to a depth of ~5 μm, and porous silicon was left in place as a support of the waveguides. However, during drying after etching, the porous silicon cracked a little. And during thermal annealing afterwards, the porous silicon layer cracked even more. So the waveguide was tilted a little by the cracked porous silicon layer as shown in the figure.

5.4 Characterization of Y-shape splitters

Optical characterization was carried out with a tunable diode laser with the tunable range from 1530nm to 1570nm. The setup is shown in Fig 5.11. The light could be coupled from the laser into an optical fiber, then through the half waveplate to select either TE or TM mode. An optical focused lens was used to couple the light into the waveguide in

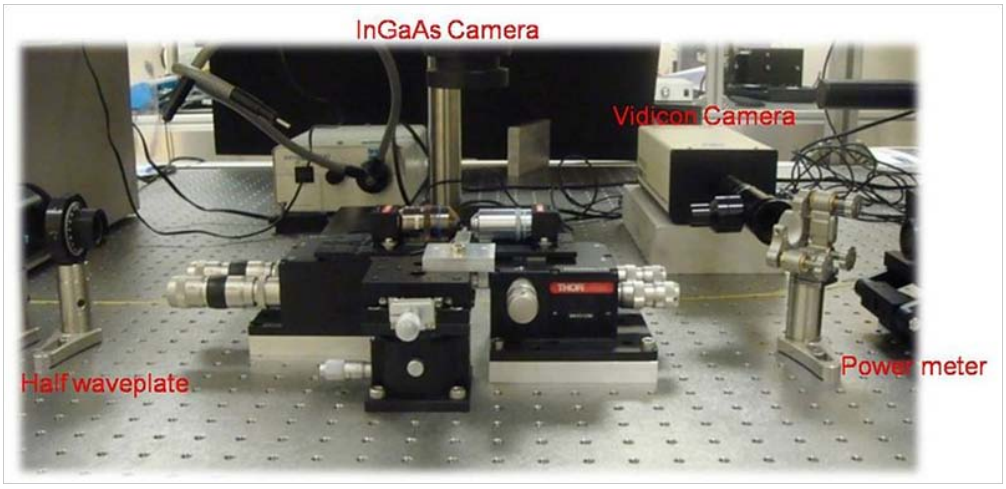

Fig 5. 11 Characterization setup.

the sample. The sample was assembled on a tunable stage, which could move the sample in three directions. Another optical lens was used after the sample to collect the output. Both lenses were also assembled on tunable stages. A InGaAs camera was used on top of the sample to monitor the light coupling in it. A Vidicon camera at the side could monitor the outputs of the sample. The power meter could measure the outputs.

5.4.1 Characterization of Y-shape splitters with short arms

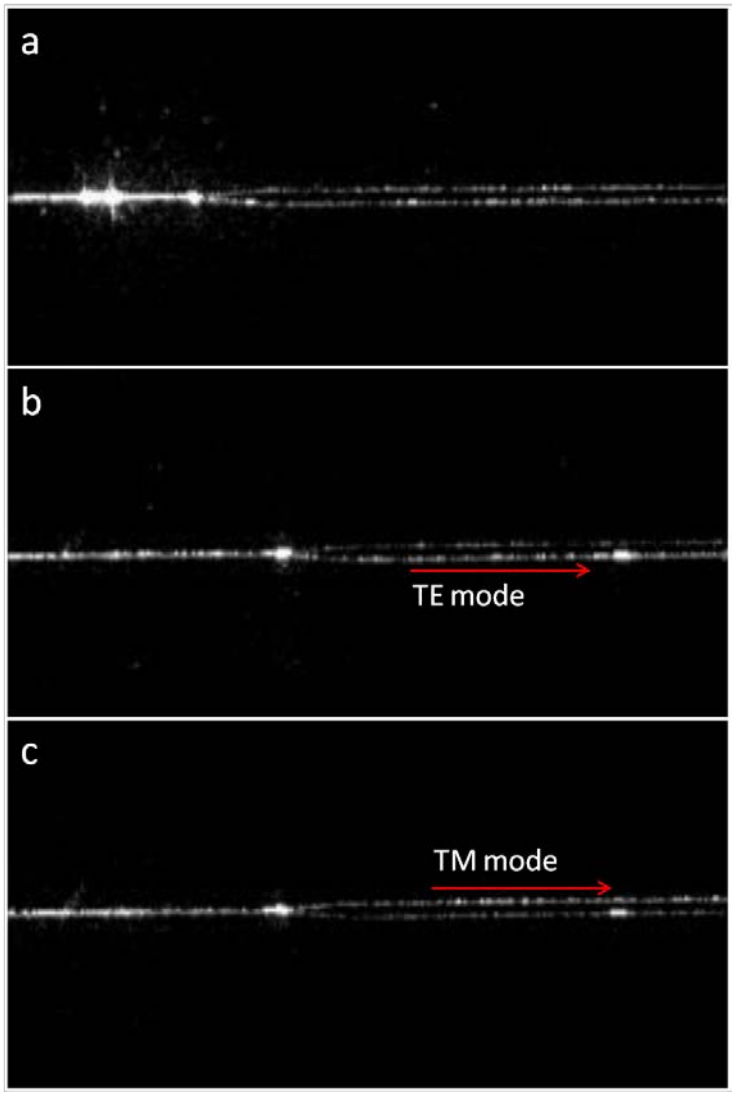

Fig 5. 12 IR images of the splitters from the top: (a) equally splitting with a normal light input without polarization; (b) TE mode input gives a stronger splitting into the lower arm; (c) TM mode gives a stronger splitting into the upper arm.

From the InGaAs IR camera on the top, we have top-view images of the splitters with light coupled in, as shown in Fig 5.12. In this splitter, when the input light was randomly polarized, as shown Fig 5.12 (a), the two arms give almost the same amount of output light. If the input light has a TE polarization, the splitting into the lower arm is stronger than the upper one, Fig 5.12 (b). When the polarization of input light was changed to TM mode, the stronger output port is now the upper one, Fig 5.12 (c).

To better study the splitting ratio, we used another IR camera at the side to capture the output images. Fig 5.13 shows the IR images of the outputs and the scans of light density from the second splitter S_2. As stated in last section, S_2 had a short arm length of 298 μm and a long arm length of 348 μm. The waveguide widths were measured to be ~5.1 μm, and the arm angle was 5˚. In this case, the incident light wavelength was 1.55 μm, we achieved significantly polarized outputs as shown in Fig 5.13. From the IR images of the outputs taken with TE (Fig 5.13 (a)) and TM mode (Fig 5.13 (b)) inputs, we can clearly see that while the left arm was TE polarized, the right was TM polarized. The left arm in the images was the long arm, and the right was the short.

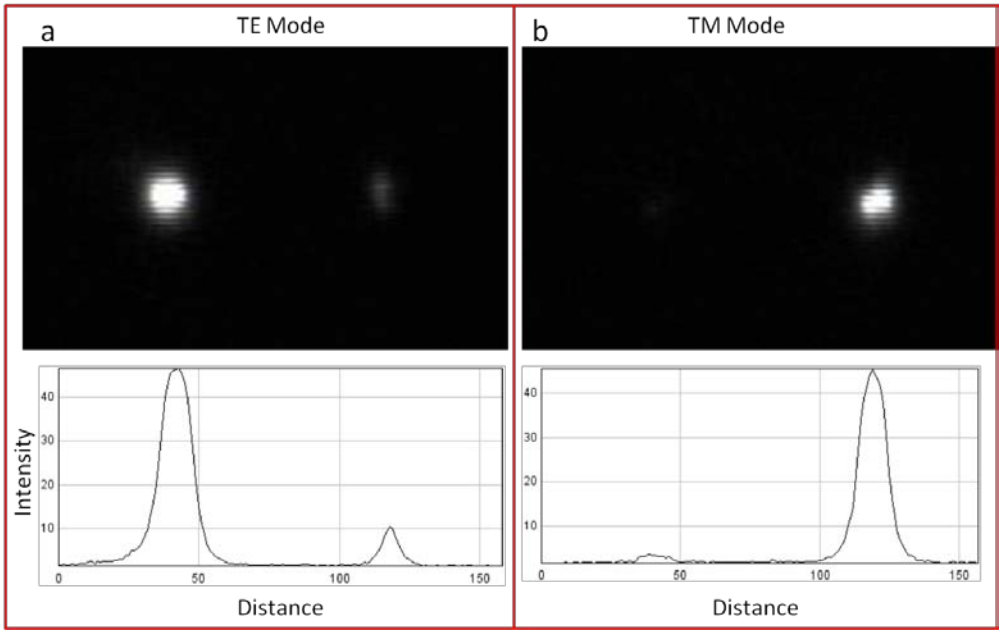

Fig 5. 13 IR images of the outputs from the side (top) and scans of light density: (a) with TE mode input; (b) with TM mode input.

To obtain the polarization ratio, we performed a square scan over the two outputs to measure the light densities, as shown in the bottom of Fig 5.13. According the measurements, in this case, the ratio of the two outputs was 9.9:1 at TE mode, and 1:27.3 at TM mode. So the TE polarization ratio was 10.0 dB, and the TM polarization ratio was 14.4 dB.

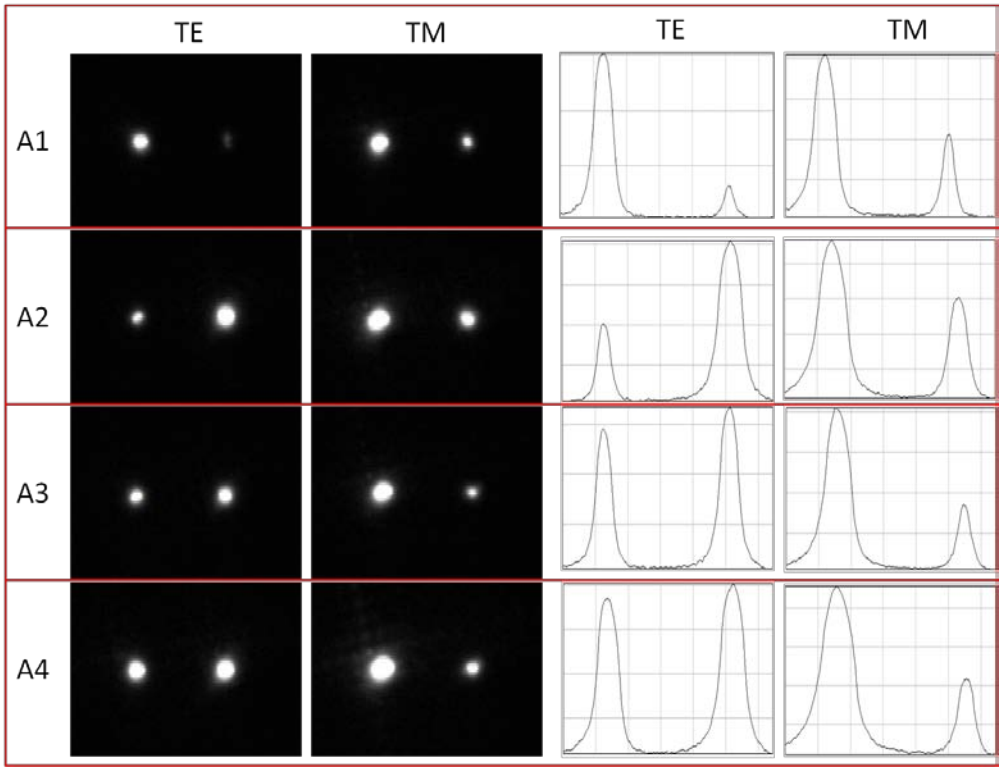

Fig 5. 14 Incident angle variation changes the polarization ratio: four different incident angles (A1, A2, A3, A4) gives different outputs at TE and TM modes.

When we slightly varied the incident angle, then the outputs were changed a lot. Fig 5.14 shows an example of this. These results were from the 7^{th} splitter S_7, with arm lengths of 323 μm and 373 μm. With four different incident angles, the TE polarization ratio differed from 9.7:1 to 1:4.5, and the TM polarization ratio differed from 2.3:1 to 4.7:1. So in this case, by varying the incident angle, the TE polarization could be reversed. Similar measurements from the 8^{th} splitter S_8 showed a result that TE polarization differed from 10.7:1 to 1:5.7, and TM polarization ratio differed from 7.1:1 to 1:4.2, in which case, both TE and TM polarizations could be reversed. This

effect was not studied in the simulations, since this mainly happened in 3D situations, while the simulations were limited in 2D cases.

5.4.2 Characterization of Y-shape splitters with long arms

As discussed in the last simulation section, if the arm length of the Y-shape splitter is long, the outputs would be sensitive to wavelength variations. In experiments, we made such splitters with long arm lengths of ~4mm.

Using the same optical characterization setup, we varied the incident light wavelength from 1535 nm to 1570 nm, and obtained an output spectrum of one of the arms, as shown in Fig 5.15. According to the plot in the figure, the polarization could be reversed by varying the wavelength of the incident light. While the output was TM polarized at the beginning of the wavelength variation (~1535 nm), it was tuned to TE polarization as the incident light wavelength increased. In this case, the maximum polarization ratio was ~5:1.

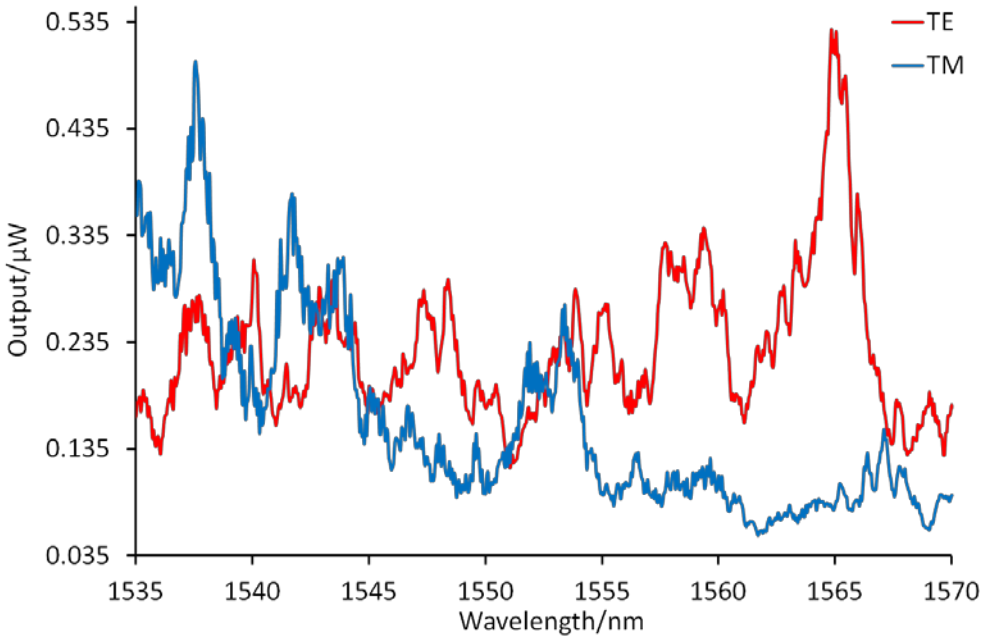

Fig 5. 15 The output oscillation along the wavelength of the incident light.

An interesting observation is that the output power oscillating behavior with incident wavelength was similar to the oscillation along the arm length

obtained in the simulation. Fig 5.16 shows a comparison of the two oscillations. Fig 5.16 (a) shows a period of the simulated output power oscillation along the arm length of a Y-shape splitter with an arm angle of 5˚ and waveguide width of 5 μm. We can see that within a big period, there are three main maxima and minima. In the experiment, from a long splitting arm, we achieved an oscillating output power with variation of incident light wavelength. And similarly, there were also a big period with three main maxima and minima, as shown in Fig 5.16 (b).

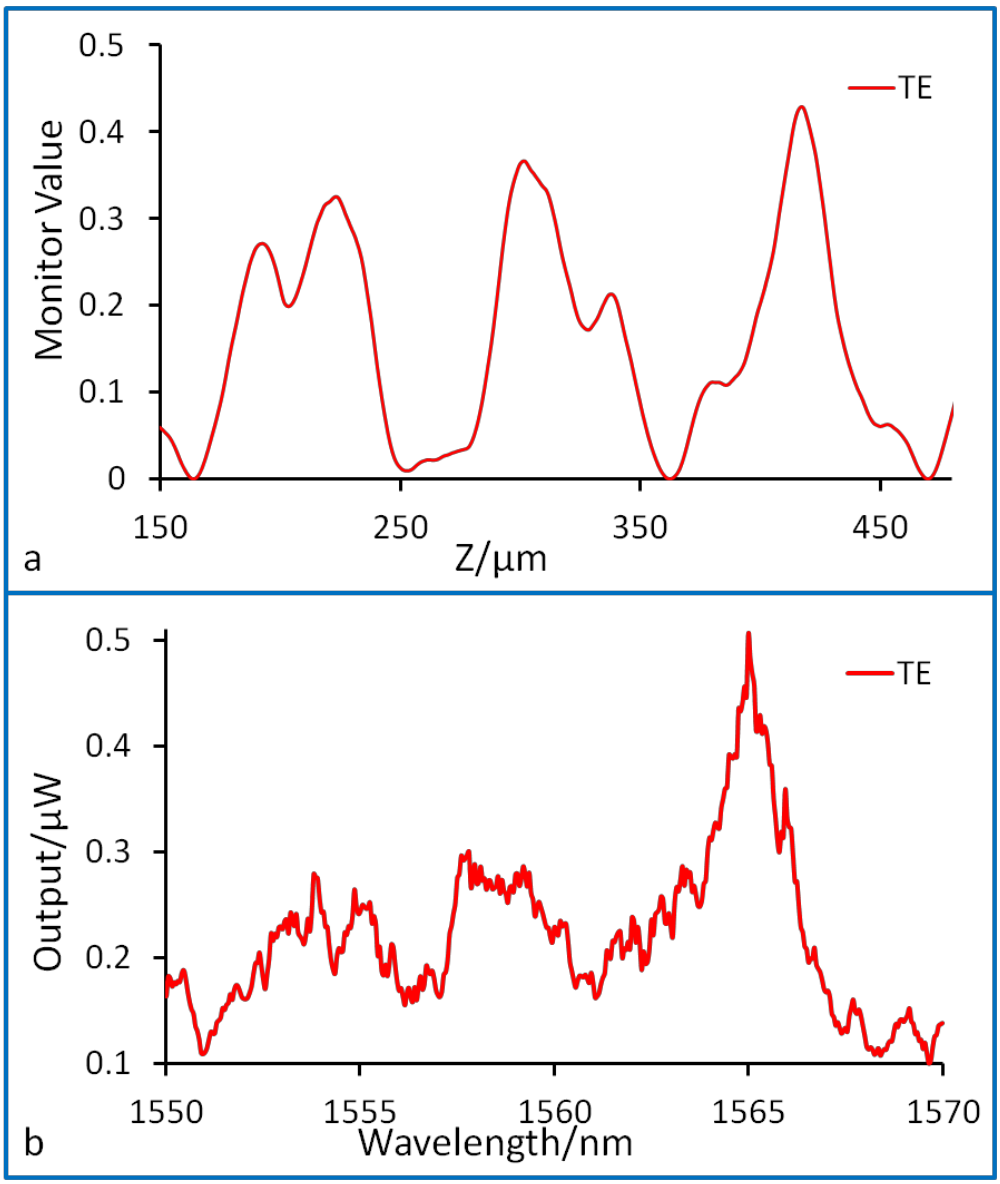

Fig 5. 16 A comparison of (a) output power oscillation along the arm length in simulation with (b) that along the incident light wavelength in experiment.

We can refer to the previous Fig 5.15. The shapes of different oscillation trends of different wavelengths are almost the same. A small variation of incident light wavelength only slightly changes the period of the oscillation, and then shifts the output power up or down a little at a certain arm length. Thus when we gradually and continuously varied the incident light wavelength, we could obtain an oscillating output which was similar to the oscillation along the arm length. The oscillation could be so significant, because the arm length was long, thus sensitive to the variation of wavelength.

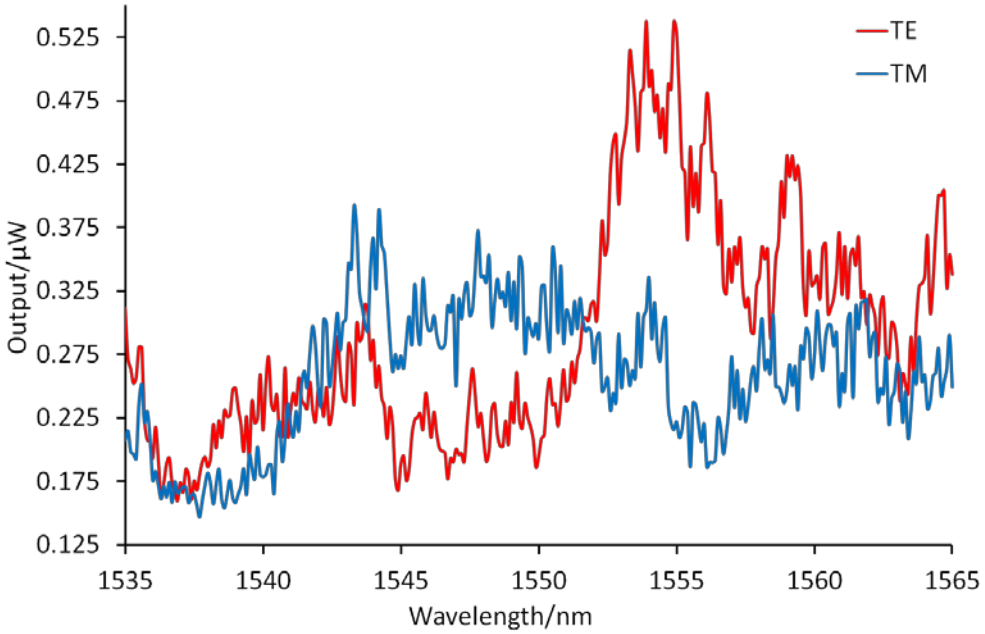

Fig 5. 17 The output oscillation along the wavelength of the incident light, with waveguide width of ~ 7.5 μm.

The oscillation with wavelength is similar to that along the arm length which is with the same conditions of arm angle and waveguide width. So if the waveguide width of the splitter changes, the oscillation along the arm length, and hence along the incident light wavelength, would change. Fig 5.17 shows a different oscillation along the wavelength from a splitter with a waveguide width of ~ 7.5 μm.

5.5 3D beam splitters

Ion beams with different energies can penetrate different depth of silicon, and create high defect regions at different depth in the silicon wafer to pattern 3D structures in bulk silicon. Using this 3D silicon machining process, we extended the study to fabrications of 3D optical beam splitters.

Fig 5.18 shows a SEM image of the splitter, and a schematic of the two irradiation steps to pattern two layers of splitting arms with two different ion energies.

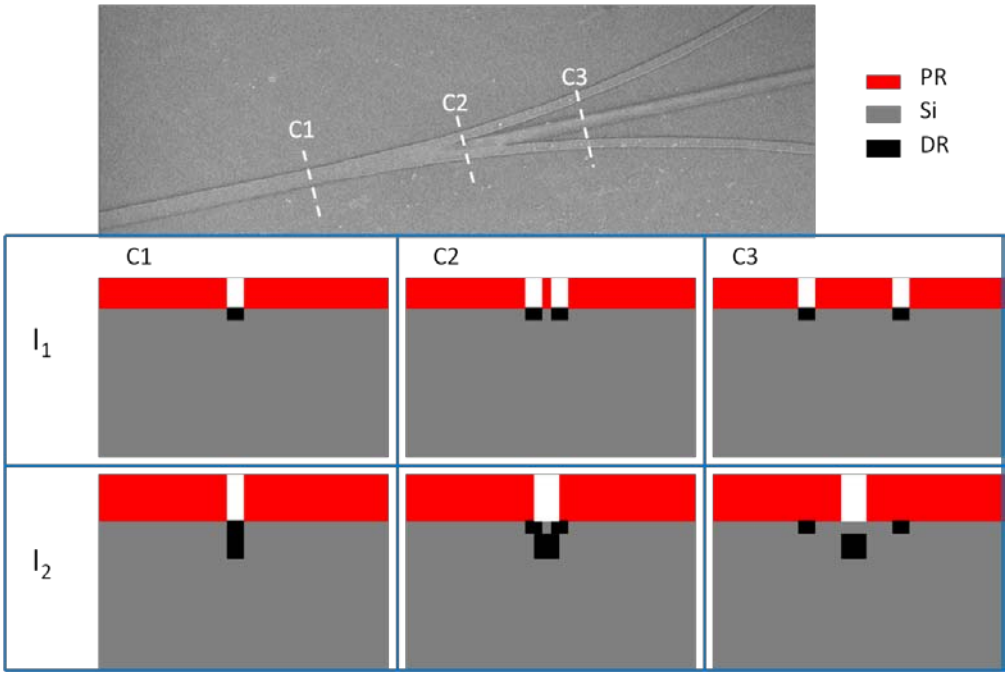

Fig 5. 18 SEM image of the splitter on top, and schematic of the ion beam irradiation patterning process: I_1, the first irradiation to pattern the two upper arms; I_2, the second irradiation to pattern the lower arm.

The first irradiation step is similar to that for the 2D Y-shape splitters. The splitter pattern was patterned using standard UV lithography on a ~2 μm thick AZ 1518 photoresist spin coated on 0.3 Ω·cm p-type silicon wafer. The wafer surface was then irradiated with a large area beam of 50 keV protons, which have a range of ~0.5 μm in silicon. The photoresist is thick enough to stop the beam going through into the silicon wafer at the regions covered by it, so defects are only created at the splitter region where it is exposed to the ion beam. The irradiation fluence was ~2×10^{16} ions/cm^2, high enough to stop PSi formation. After first irradiation, we used physical vapor deposition (PVD) to

deposit a layer of 30 nm thick gold on the surface, and then removed the photoresist. Gold deposition on the surface was used to make an alignment mark for the second irradiation step. When the first step photoresist was removed, a gold pattern of the splitter would remain on the silicon surface. Another layer of ~ 6 µm thick AZ 9260 was spin coated, and then an aligned UV lithography was carried out for the second layer pattern. A higher energy of 200 keV ion beam was large-area irradiated to the sample. The second high energy ion irradiation should be with lower fluence to only create high defect region at the end of range. The fluences were varied from 5×10^{13} to 5×10^{14} ions/cm^2. After removing the second step photoresist, the wafer was electrochemical etched in 24% HF with a current density of 60 mA/cm^2 for ~1 minute to make a porous silicon layer of ~ 2.4 µm thick. Then the porous silicon layer was removed in KOH solution, and the wafer was electrochemically etched for the second step with a current density of 40 mA/cm^2 for 5-6 minutes to make a porous silicon layer of ~10 µm thickness. Finally, the wafer was annealed and thermal oxidized in air at 1000˚C for 10 hours. The width of the splitter waveguides was designed as 4 µm.

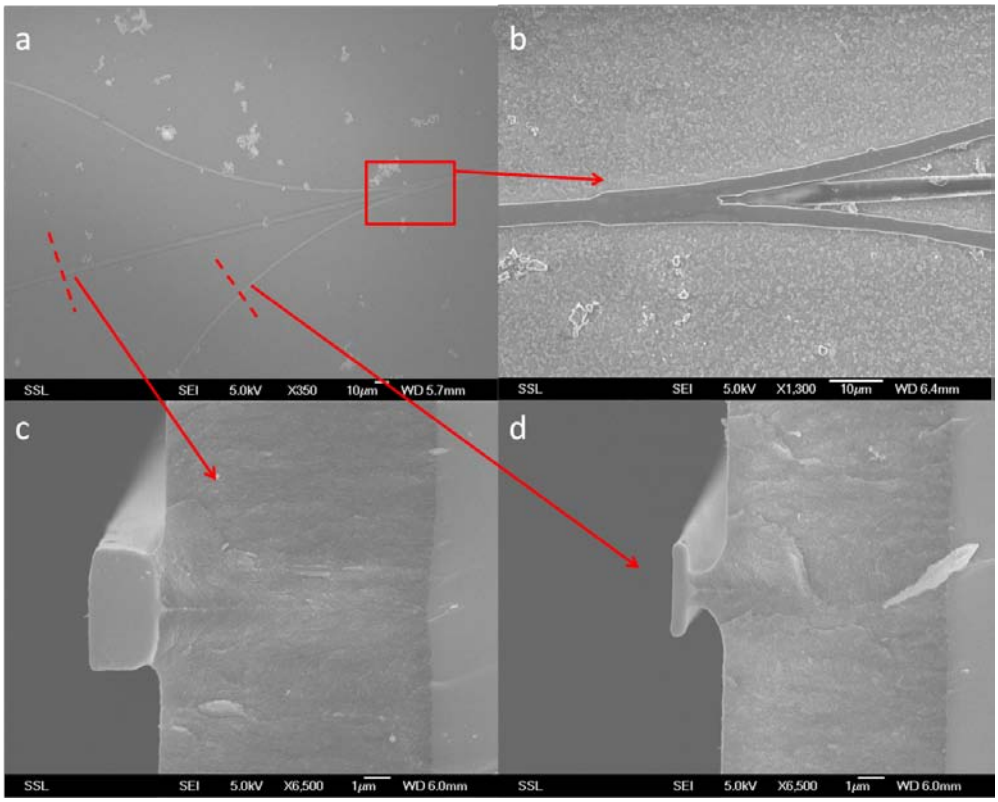

Fig 5. 19 SEM images of the splitter: (a) an over view, (b) magnified splitting region, (c) high magnification cross section of the lower waveguide, (d) cross section of the upper waveguide.

Fig 5.19 shows SEM images of the 3D splitter structures. We made two different shapes of the two upper splitting arms: straight angled arms and curved arms. The figure shows curved upper arms. The lower arm was designed to be straight forward from the main waveguide input. From the magnified image of the splitter region, Fig 5.19 (b), we can clearly see that the three arms are at different layers on the substrate. The cross sections show that the lower arms are much thicker (1.8 μm) than the upper one (0.5 μm). The width of them were designed the same. However, after etching they were slightly different. In this case, the lower arms were quite thick as the second irradiation fluence was high (5 $\times 10^{14}$ ions/cm^2).

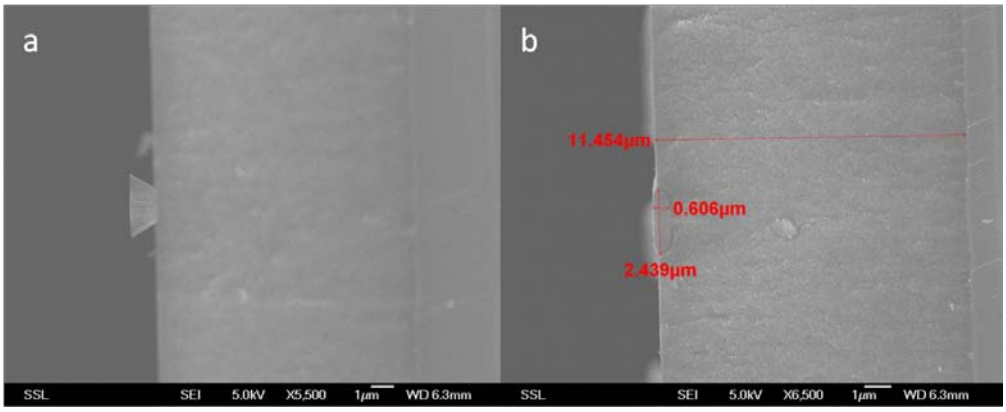

Fig 5. 20 SEM images of the cross section of the lower waveguides with fluence : (a) 2×10^{14} ions/cm^2, (b) 5×10^{13} ions/cm^2.

The reduced second irradiation fluence was aimed at giving thinner lower arms. When the fluence was 2×10^{14} ions/cm^2, the lower arms were reduced to ~1.3 μm, as shown is Fig 5.20. They were further reduced to ~0.6 μm with an irradiation fluence of 5×10^{13} ions/cm^2.

Characterization was carried out with similar setup as used for 2D splitters. IR images of the light coupling in the 3D splitter are shown in Fig 5.21. We can see that the light is coupled into the main waveguide. When there is another light source shining on the sample from the side, we can see

the two curved upper arms, Fig 5.21(a). However, without the side light source, we can not see any light coupled from the main waveguide into the two upper arms, Fig 5.21(b), which means there is too little or no light coupled into them.

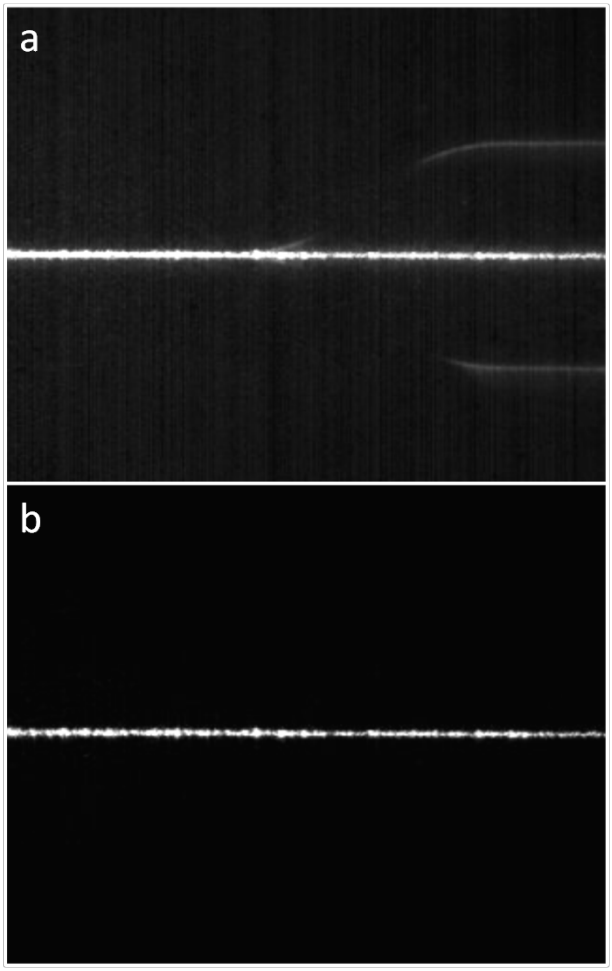

Fig 5. 21 IR images of the light coupling into the 3D splitter from the top: (a) with , and (b) without a side light shining on the sample. The background is dark, because the light is confined in the waveguide.

While most light was coupled from the main waveguide into the lower straight arm along the main waveguide, little light was coupled into the two curved upper arms. This is caused by the geometry of the structure. The lower arm had a similar thickness and same direction with the main waveguide, thus light modes would be mainly confined within it. The two upper arms were too thin compared to the main waveguide and not in the same direction, so few light modes would be coupled into them.

Acording to RSoft simulations, to make the light from the main waveguide split equivalently into different arms at different layers, the arms should have same thicknesses and same angles with the main waveguide. This could be carried out in the future works.

Chapter 6

Vertical Coupling Photonics

6.1 Introduction

At present, most photonic devices still are two dimensional, using lateral coupling. These devices are mainly fabricated within the device layer of SOI platforms. The typical thickness of the device layer is 200-300 nm. With such a small thickness, it is difficult to couple an incident light from optical fibers or lenses into the waveguide from its side. So, grating couplers are widely used to make the coupling of light easier.

To achieve 3D integration, vertical coupling becomes necessary. Besides, vertical coupling makes the fabrication process more flexible. For example, the waveguide and the resonator layers can be designed and controlled independently, as they are separated in different layers. Furthermore, the control over critical dimensions, especially the gap between them, can be easier and more precise.

Traditional semiconductor machining processes mainly use UV lithography to pattern a photoresist, followed by reactive ion etching (RIE) to transfer the pattern on to silicon surface. To achieve vertical coupling of structures, either wafer bonding[10, 11] or chemical vapor deposition (CVD)[12] or epitaxial growth[13] is needed. In wafer bonding, devices are fabricated on two separated chips, and then the two chips are aligned and attached. CVD is mainly for deposition of organics to fabricate polymer devices. While epitaxial growth can help to fabricate heterostructure devices using semiconductors like SiGe and GaAs.

As discussed before, high energy ion beams can penetrate many micrometers into semiconductor materials, such as Si and GaAs. In p-type silicon, we have developed a process to combine ion irradiation with subsequent electrochemical anodization to machine in 3D.[85, 130, 131] The flow of anodization current is deflected away from irradiated regions, leaving them unetched, and surrounded by porous silicon. Most of the ion induced defects are located close to the end-of-range of the ions, so for low fluences only the end-of-range region remains unetched while regions closer to the surface become anodized. Thus by varying the ion energy it is possible to directly fabricate 3D structures in Si and other semiconductors. In this chapter, we apply this process to fabricate vertical coupling structures on SOI platforms.

6.2 Vertical coupling waveguide-resonators

Our ion beam silicon machining process is unique that it can penetrate into the sub-surface layer of materials and change the material properties more than at the surface. Normally, after machining the device layer of SOI wafers, nothing can be done to the underlying substrate layer. However, if we apply ion beam irradiation, we can pattern the underlying substrate layer after patterning the device layer. Thus, we are able to use a single SOI wafer to obtain vertical coupling structures without any wafer bonding or CVD or epitaxial growth, and achieve an all-silicon device.

Fig 6.1 shows a schematic of the main fabrication process. Firstly, we use UV lithography and RIE to define the microdisk on the device layer. We then use an aligned proton beam irradiation step, Fig. 6.1 (c), to make the waveguide pattern in the Si substrate layer, forming an ion induced defect region with a certain width and thickness. The width is determined by the design, while the thickness is determined by the proton beam energy. [85, 130, 131] After removing the photoresist, the wafer was placed in a 24% HF solution for 1 minute to etch away the BOX layer to expose the substrate, followed by two electrochemical anodization steps, Fig. 6. 1 (d,e). Finally, the sample is annealed in low ambient pressure (~1 mbar) at 500℃ for 10 hours,

to anneal out the ion induced defects while providing a small amount of oxidation-induced surface smoothening[25, 132].

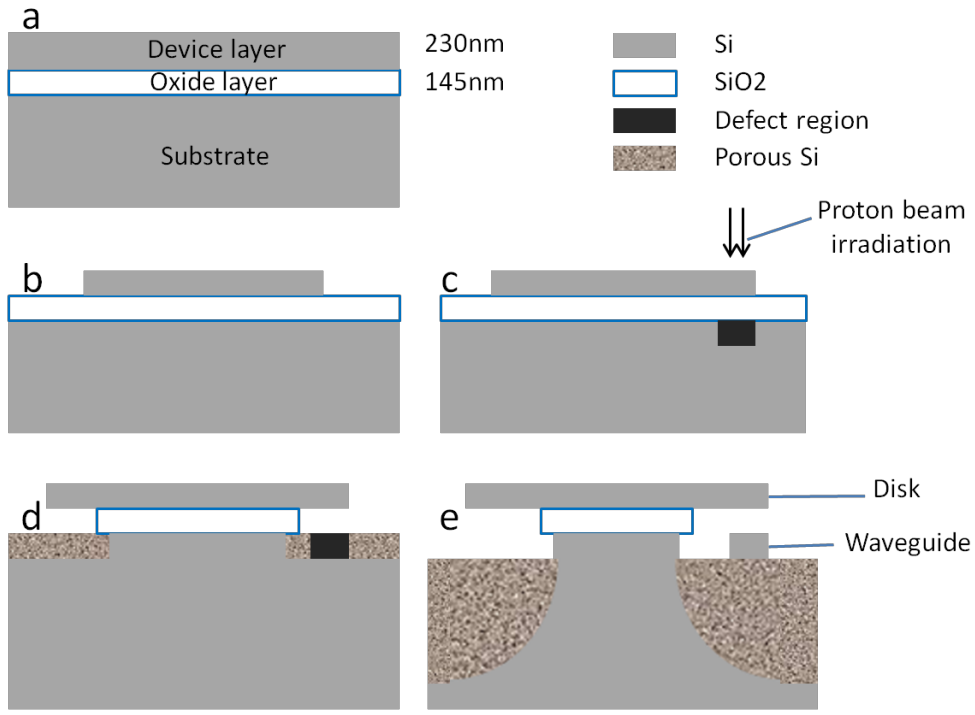

Fig 6. 1 Schematic of the fabrication process. (a) SOI wafer; (b) RIE to fabricate the microdisk, (c) aligned proton beam irradiation to make the defect region for the waveguide in the substrate layer, (d) oxide layer removing and Porous Si formation, (e) another etching step to undercut the bottom waveguide.

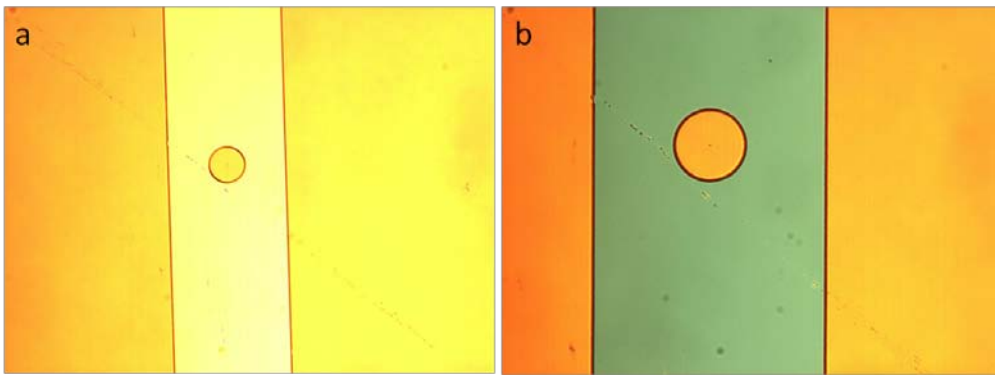

Fig 6. 2 Optical micrographs of the disk pattern, (a) before and (b) after RIE.

Fig 6.2 shows the color difference of the SOI surface with and without the device layer on top, before and after the RIE. When there is a 55 nm thick silicon device layer on top, it looks yellow, Fig 6.2 (a). After RIE etching off the device layer, the 145 nm thick oxide layer on silicon substrate looks green, Fig 6.2 (b). During the development of the whole process, this first step for the device layer patterning is fixed like this.

6.2.1 Development of the fabrication process with a thin device layer

In the schematic process figure, the SOI wafer has a device layer of 230 nm thickness. However, at the beginning, we only had access to SOI wafers with a 55 nm thick device layer. To achieve aligned ion beam irradiation, there are two ways: one is to use direct proton beam writing to find the position and write the waveguide; the other is to use an aligned UV lithography to make the waveguide pattern on the photoresist and then use a large area ion irradiation to transfer the pattern into silicon substrate layer.

At the beginning of this project, we used direct proton beam writing to do the alignment. Fig 6.3 shows the fabrication result of the first time try. After RIE to define the microdisk on the device layer, without removing the photoresist on top, we used a focused 200 keV protons to scan at the edge of the disk to find the position, and then used a line scan to make the waveguide patterned irradiation. In the figure, we can see that two layer structures were successfully fabricated on the SOI wafer, with the microdisk on top of the waveguide. However, there were some problems: the photoresist on top was not fully removed, which made the structure dirty; the scanning used for positioning affected the patterning of the waveguide.

So we further optimized the process by improving the positioning step. We made two additional microdisks to either side of the central one with same dimensions. The two additional disks were used as alignment marks during positioning. As we found the position of P_1 and P_2, Fig 6.4, we could easily know the position of P_0. This allowed us to find the position without scanning around the central disk, and to achieve an unaffected waveguide.

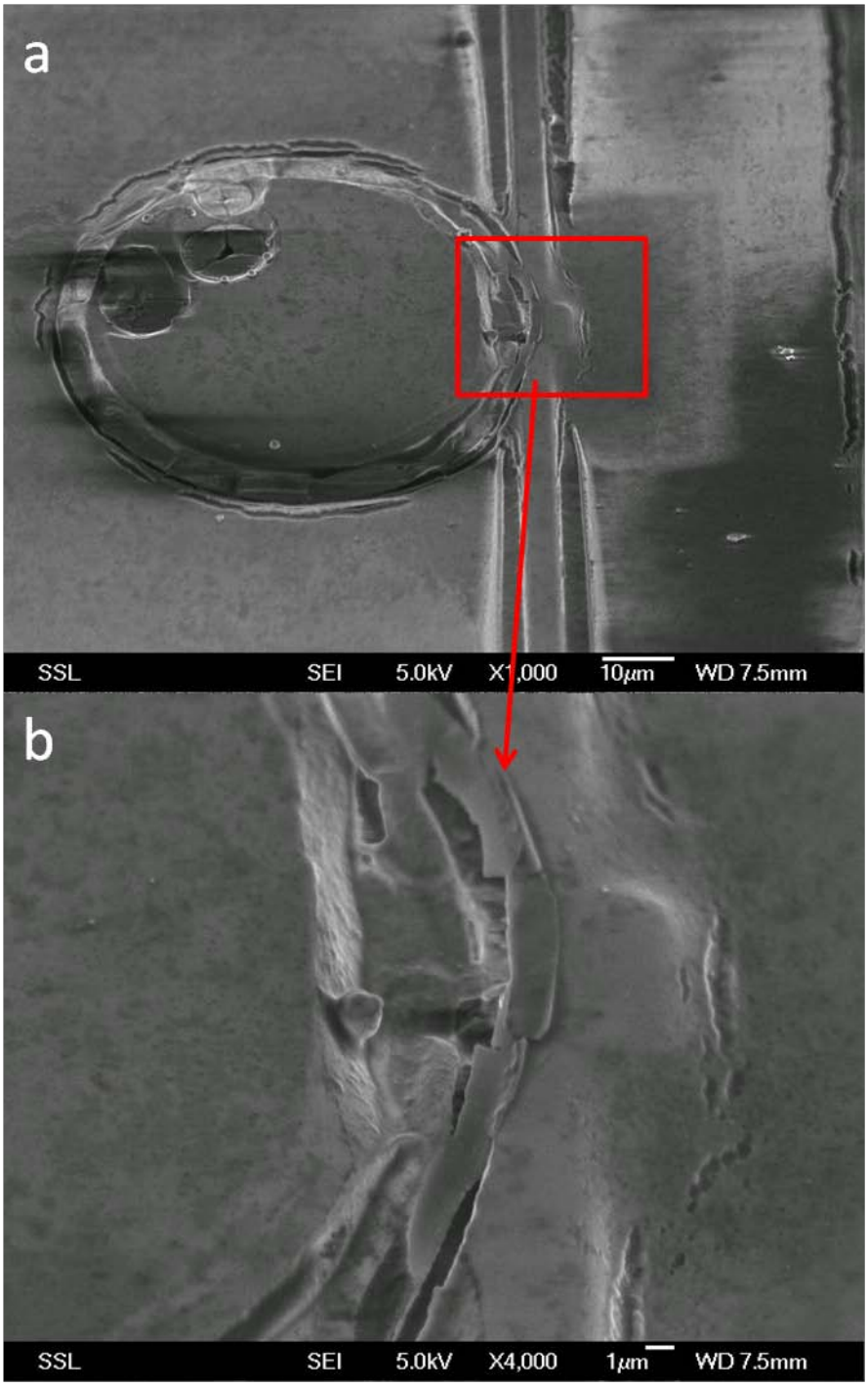

Fig 6. 3 SEM images of the first attempt, (a) overview of the vertically coupled waveguide and microdisk, (b) a magnified view at the coupling region.

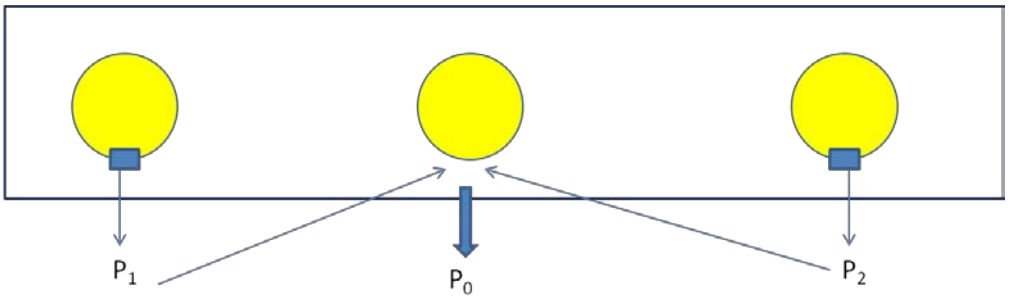

Fig 6. 4 Schematic of the positioning process.

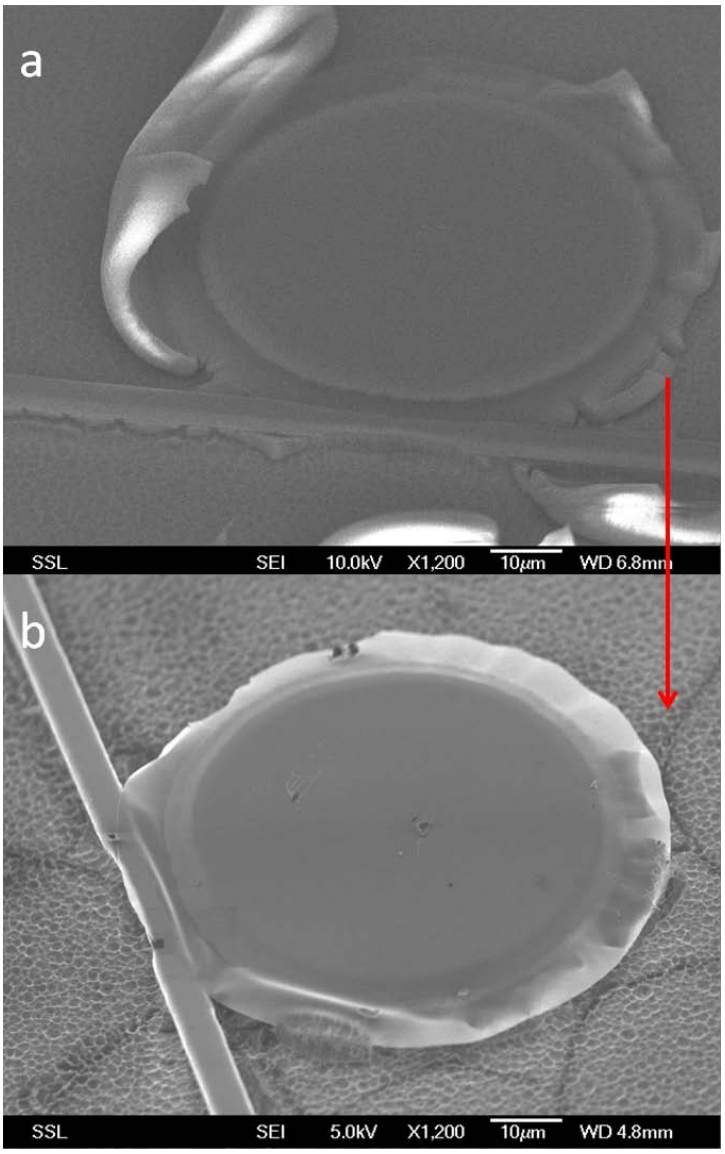

Fig 6. 5 SEM images of the first time result, (a) before and (b) after annealing.

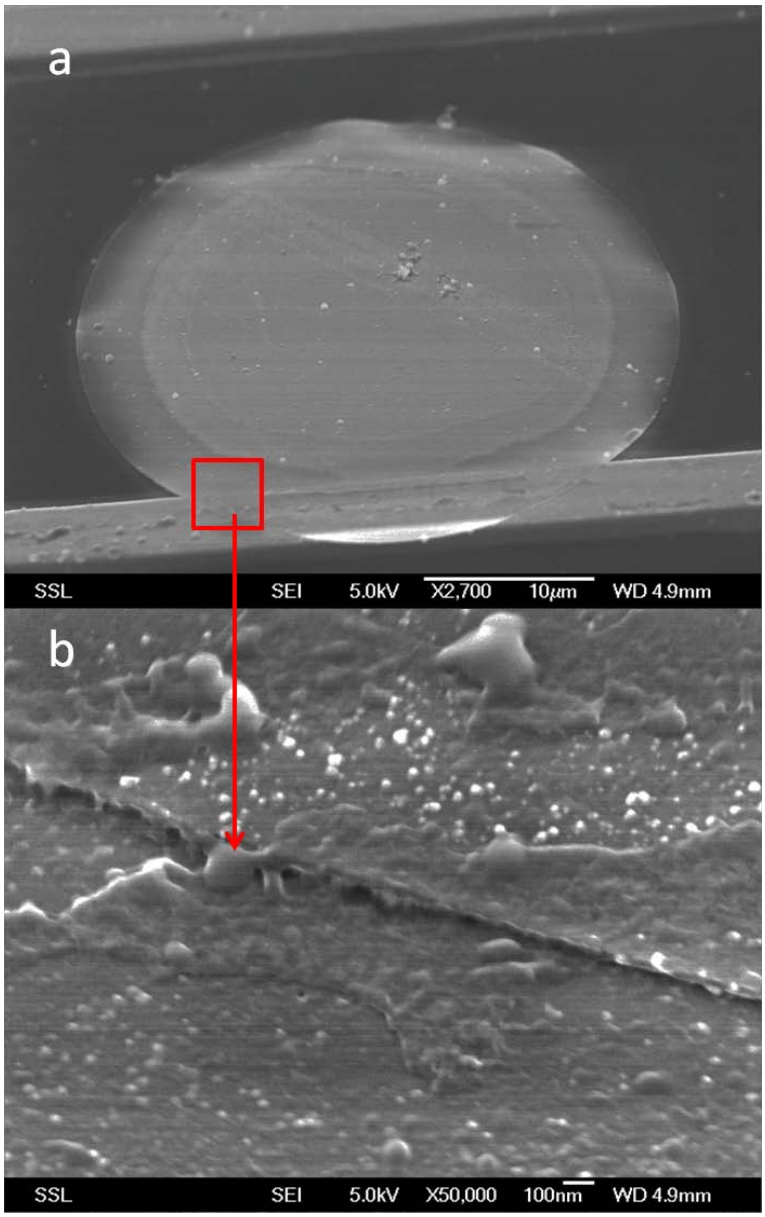

Fig 6. 6 SEM images of the result using UV alignment followed by a large area irradiation, (a) overview and (b) high magnification of the coupling region.

Fig 6.5 shows the improved results with direct proton beam writing. We obtained a much better result in the figure, with a well-defined microdisk and waveguide sitting at different layers. The problem this time was the remaining porous silicon layer cracked and broke off some part of the disk during thermal annealing because of the deformation.

Direct proton beam writing using a focused ion beam is able to carry out the aligned patterning of the waveguide in the substrate layer. However,

the efficiency of this process was very low; it took a lot of time to find the positions and a much longer time for writing the waveguides as the current of a focused beam could not be high. In view of these limitations, we attempted to first use UV alignment to make an aligned waveguide pattern on the photoresist, and then transfer it into substrate silicon layer.

Fig 6.6 shows the result using UV alignment and large area irradiation. This method is able to achieve the same result, with the advantage that it makes mass production possible since many structures can be created at the same time. We could pattern any number of sets within an area of ~1.5 × 1.5 cm^2 by only one ion beam irradiation with a fluence of 1×10^{15} ions/cm^2 within 30 minutes. In comparison, using direct proton beam writing, it would take a whole day to only finish writing 5 sets of vertically coupled waveguide-microdisks. The substrate layer of the SOI wafer was high resistivity, so a fluence of 1×10^{15} ions/cm^2 was high enough to fully stop the etching. Now the only problem remaining was that the device layer was too thin for the light coupling into it, and makes the disk easily bent and distorted.

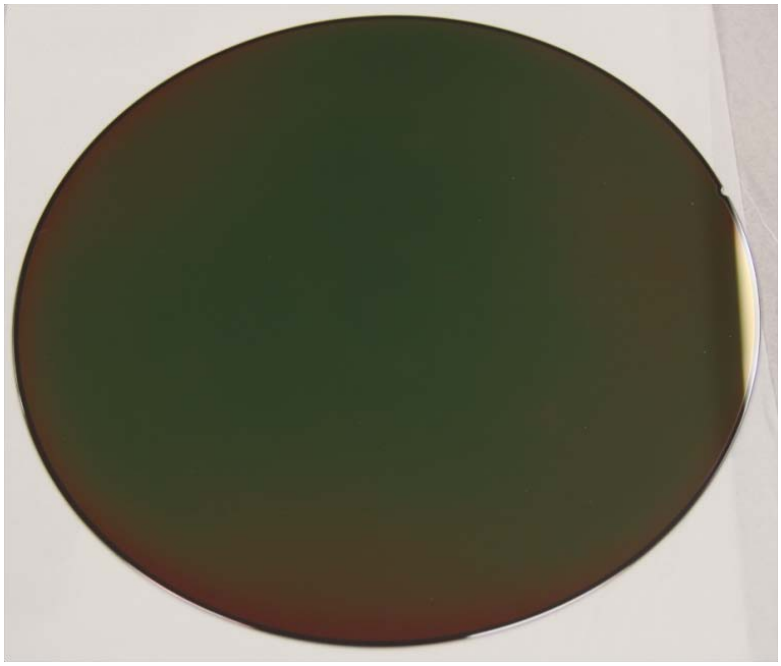

Fig 6. 7 8 inch SOI wafer after epitaxial growth, device layer from 55 nm to 230 nm.

Typical SOI wafers used for silicon photonics usually have a device layer thickness of 200-300 nm. [4, 6, 7] To make the SOI wafer suitable for light coupling and also compatible with typically used 2D photonic structures, the device layer was epitaxially grown to a thickness of 230 nm. Fig 6.7 shows the epitaxial grown SOI wafer, device layer from 55 nm to 230 nm. However, we can see that the growth was not uniform, since the color of the wafer surface was not uniform after growth, especially at the edges. A profilometer was used to measure the device layer thicknesses at different locations of the wafer. The result showed a thickness variation from 200 nm to 245 nm. The lack of uniformity can affect the optical properties of the device layer.

6.2.2 Details of the fabrication process with an epitaxially grown device layer

We used the re-grown SOI wafer and followed the same fabrication process as described above. The first UV lithography for the microdisks and microrings used AZ 1505, 1518 or 9260. Before spin coating, a HMDS treatment was necessary for better adhesion of the photoresist with the SOI substrate. AZ 1505 has a typical thickness from 0.4 to 0.8 μm, 1518 from 1.3 to 2.4 μm, while AZ 9260 has a typical thickness around 5 μm. In this case, AZ 1518 was a better choice, as it was thick enough to fully stop the RIE, and also had a better resolution than thick AZ 9260. We made series of microdisks and microrings with diameter varying from 20 μm to 100 μm. Microrings had inner circles and outer rings, with six supports connecting them, as shown in Fig 6.8. The supports and outer rings were designed with a width of 4 μm on the UV masks, but usually they were reduced to ~ 2.5 μm after UV lithography and RIE on the silicon device layer. The UV conditions were set following the typical data sheets with slight variations according to the results in the experiment. For example, with AZ 1518, we used a spin coating speed of 6000 rpm and soft bake time of 1 minutes at 95 ˚C for a thickness ~ 1.4 μm, with an exposure fluence of ~ 90 mJ/cm^2 (wavelength 405 nm), and a developing time of 1 minute.

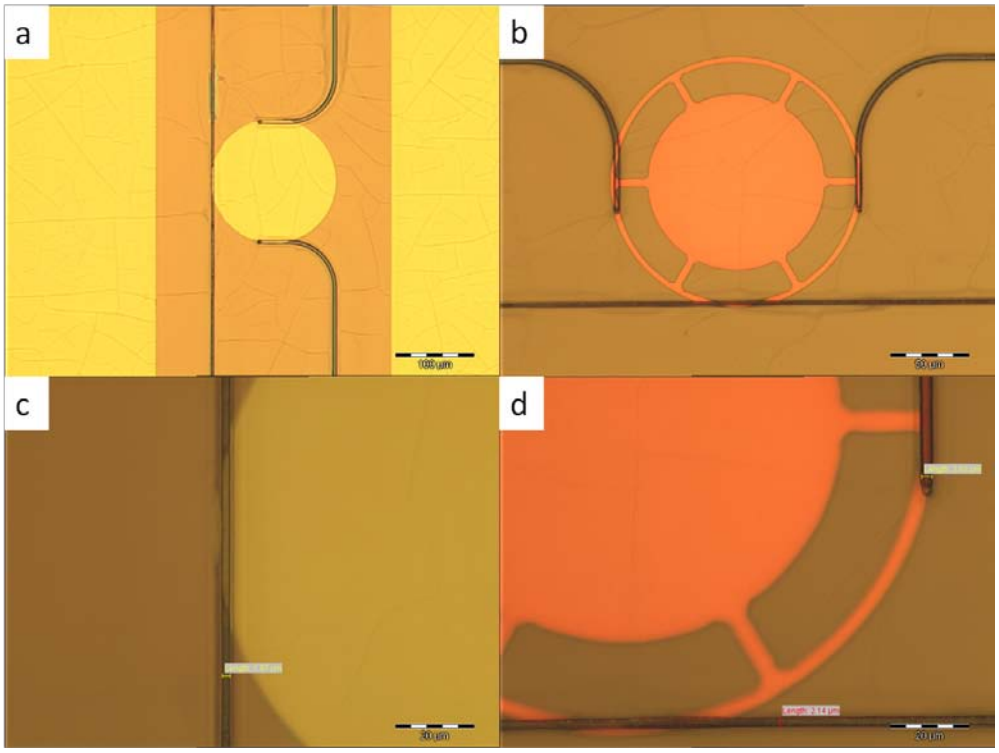

Fig 6. 8 Microscope images of the UV alignment: (a) waveguides with a microdisk, (b) with a microring, (c,d) magnified images at the coupling region.

After RIE, we removed the first layer AZ photoresist and spin coated a layer of SU8 on the wafer. We chose negative photoresist SU8, because it was easier to use it for the UV alignment, with a bigger transparent blank area on the mask. Two different series of SU8 were used in this process: SU8 2000.5 with a typical thickness of ~0.7 µm, which is thin and could achieve smaller structures, but only applicable for low energy ion beams, and SU8 2005 ~5 µm, thick for bigger structures and applicable for higher energy ion beams. At the beginning of this work, we mainly used SU8 2005, as it was thick enough to stop a higher energy ion beam. Fig 6.8 shows some images of the UV alignment after RIE for the structures on the device layer and before the large area ion beam irradiation. For SU8 2005, we typically used a spin coating speed of 4000 rpm for a thickness ~5 µm, a soft bake time of 2 minute at 95 ˚C, an exposure fluence of 80 – 120 mJ/cm^2 (365 nm), a post exposure bake time of 2.5 minutes, and a developing time of 1-2 minutes. On the second layer pattern, there were three waveguides aligned to each microdisk or microring, with a straight one as the input and transmission out port, and two

curved ones for the reflections from either direction of the straight waveguide. The straight waveguides were designed to be a tapered shape with a central width 2.5 μm, and 4 μm at the ends. The curved ones were designed with a uniform width of 4 μm, and the curve diameter of 200 μm. As the photoresist was ~5 μm thick, the 4 μm wide lines were easy to be fully developed, but the 2.5 μm ones were difficult. In the figure, we can see that some central part of the straight waveguides was not fully developed, since the photoresist was thick and the waveguides were thin at the central part. The central part was designed to be thin so as to achieve single mode. In our experiments, the exposure fluence should be 110 – 120 mJ/cm^2 to make the central part of the straight waveguide fully developed. With such a high exposure fluence, the waveguide would be slightly wider (~1 μm wider) than designed.

The ion beam irradiation was carried out after the aligned UV lithography with 400 keV H_2^+, which was equivalent with 200 keV protons, to make waveguides with a thickness of ~2.5 μm in the substrate layer. The irradiation fluence was ~1×10^{15} protons/cm^2 or more, which was high enough to fully stop the etching. If the photoresist

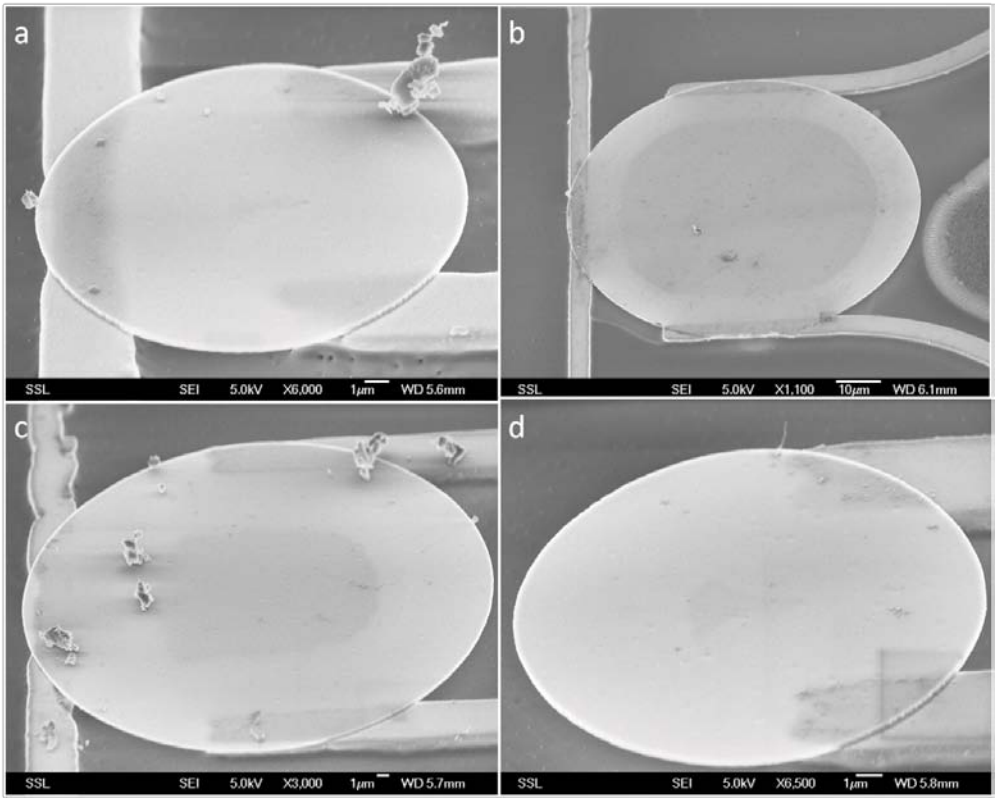

Fig 6. 9 SEM images of the structures: with (a-d) fully developed waveguides to undeveloped central part.

waveguide pattern was fully developed, then ion irradiation would produce a fully patterned waveguide region which would result in a well-defined waveguide after etching, as shown in Fig 6.9 (a). If not, there would not be a full waveguide patterned defect region, and it would come out with a waveguide with some defects, as shown in Fig 6.9 (b, c). If the photoresist waveguide pattern was developed so little that no ion could penetrate through that part, the straight waveguide would break at the central part, as shown in Fig 6.9 (d). In the figure, (a) and (d) had disks with diameter of 20 μm, (c) with 40 μm, and (b) with 60 μm. We see that the disks were without any significant bending in this case, with a thicker device layer (~230 nm).

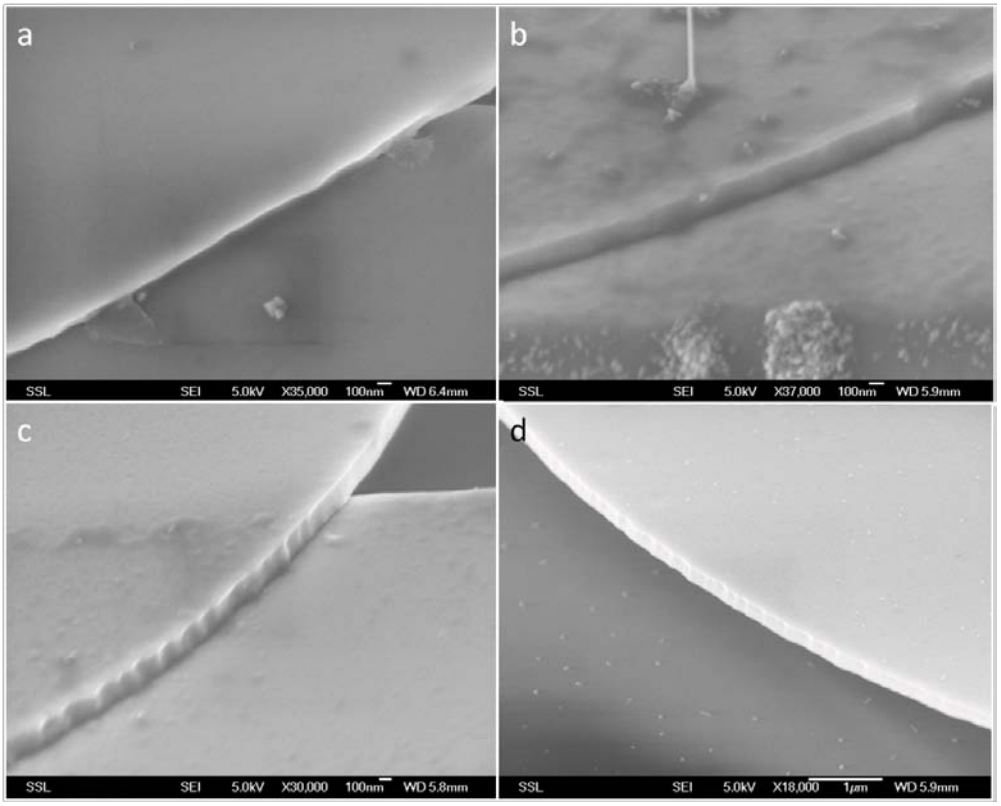

Fig 6. 10 High magnification of SEM images of the structures: (a-c) at the coupling region; (d) out of the coupling region.

Some detailed views of the structures at the coupling regions are shown in Fig 6.10. The one in Fig 6.10 (b) had a rough and dirty disk surface, probably because of photoresist residuals during the process. Even if the surface was clean, without any photoresist residuals, the part over the lower waveguide could be rough, Fig 6.10 (c), possibly due to it being slightly electrochemical etched since the gap between the two layers was too small, leading to it not being fully insulated. If the two layers were well separated and insulated, the surface of the disk would be smooth, Fig 6.10 (a). Out of the coupling region, the disk surface was also smooth, Fig 6.10 (d). The edges of the disks on the device layer were not smooth, resulting from the UV lithography and RIE steps.

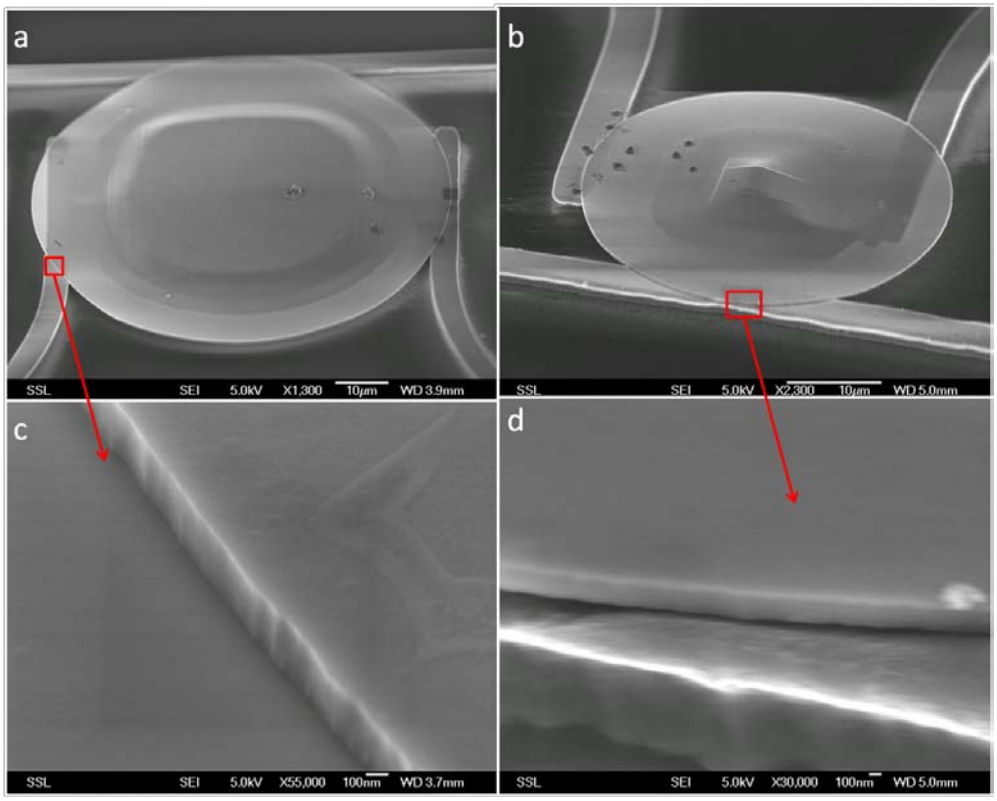

Fig 6. 11 Reduced surface and edge roughness: (a,b) over view, (c,d) fine view at the coupling regions.

Further optimization of UV lithography and RIE, an additional reflow process after lithography and shorter silicon etching time during RIE, could reduce the roughness of the edges of the disks. Another way to reduce the

surface roughness is to use thermal reflow for silicon, which could be carried out at ~1100 ˚C in hydrogen flow,[133] but this facility was not available for safety reasons**.** Instead we annealed the sample at 500 ˚C in low ambient pressure (~1 mbar) for 10 hours to anneal out the ion induced defects and also to provide a small amount of oxidation-induced surface smoothening. The results are shown in Fig 6.11. The disks had clean and smooth surface. The edge roughness was also reduced by lithography optimization and thermal annealing. However, thermal annealing created another problem, that the disks were bent. This was probably because of the deformation of the porous silicon layer during thermal annealing process.

Optical characterization was carried out using a similar setup as that previous used for the splitters. A tunable laser with a wavelength from 1530 nm to 1570 nm was used to test the resonance of the microdisks and microrings. However, to date we have not obtained any resonance in the measurements, probably because that the waveguides were too thick for single mode and efficient coupling.

6.3 Vertical coupling waveguide-to-waveguide

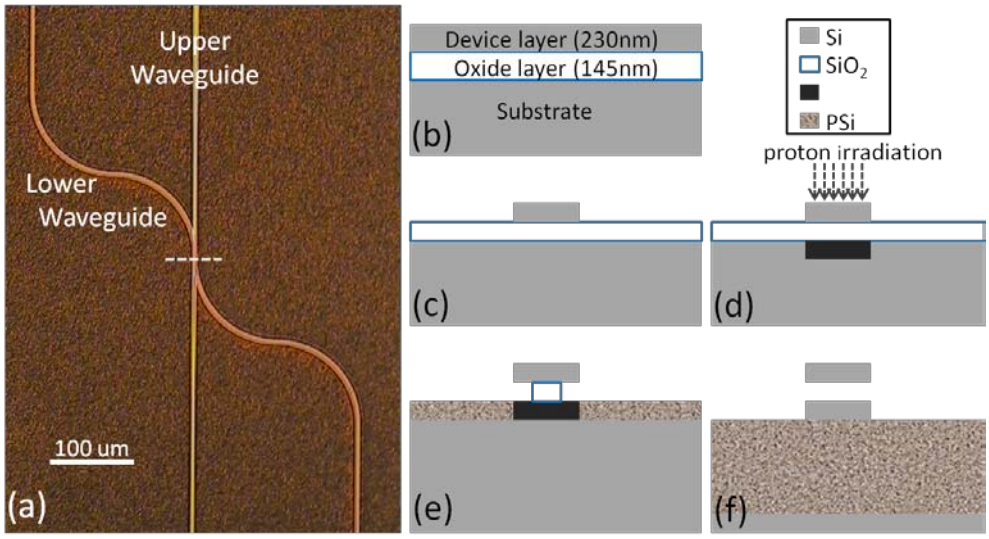

Fig 6. 12 (a) Optical micrograph showing an overview of the structure. (b-f) show a schematic of the fabrication process viewed along a cross section at the dashed white line in (a). (b) SOI wafer dimensions, (c) RIE to fabricate the top Si waveguide (WG), (d) proton beam irradiation to create a high defect density (HDD) region for the lower waveguide in the substrate, (e) anodization resulting in oxide layer partial removal and PSi formation, (f) final

anodization step to undercut the lower waveguide, followed by annealing to remove the lattice damage.

A simpler but more fundamental vertical coupling case in photonics is vertical coupling waveguide-to-waveguide. Using a similar fabrication process as described in the last section, we easily fabricated vertically coupled waveguides. An optical micrograph of the structure and the fabrication process viewing from the cross section are shown in Fig 6.12. A similar process using UV lithography, RIE, ion beam irradiation and electrochemical etching is described in the figure and its caption. Since a similar process was already described in detail in last section, we do not go into the details here again.

6.3.1 First attempt

The straight upper waveguides on the device layer were designed with width of 2.5 μm and 4 μm at the central coupling portion, and 10 μm at the ends, away from the coupling region. The curved lower waveguides on the substrate layer had a designed width of 4 μm, and a curved diameter of 200 μm. However, the upper waveguides were usually thinned during the UV lithography and RIE, while the lower were usually broadened because of the scattering of the ion beam making a wider defect waveguide pattern. So the result was usually a smaller width than designed for the upper waveguides, and a larger for the lower waveguides. SEM images in Fig 6.13 show one of the results. In the over view of the structure in Fig 6.13 (a), there are some bright part around the waveguides. This is because of charging of the insulated oxide porous silicon during SEM image collection. In Fig 6.13 (b), we can clearly see that the lower waveguide (~4.3 μm) was wider than the upper one (~3.8 μm), although they were designed with the same width. A cross section image at the end of the waveguides, Fig 6.13 (c), shows that we had a thick lower waveguide port and a thin but wide upper waveguide port. A big width at the ends of the upper waveguides was to ensure that they were not fully undercut, so able to stand on the substrate. A thick lower waveguide port at the ends makes the coupling of incident light from an optical fiber or lens easier.

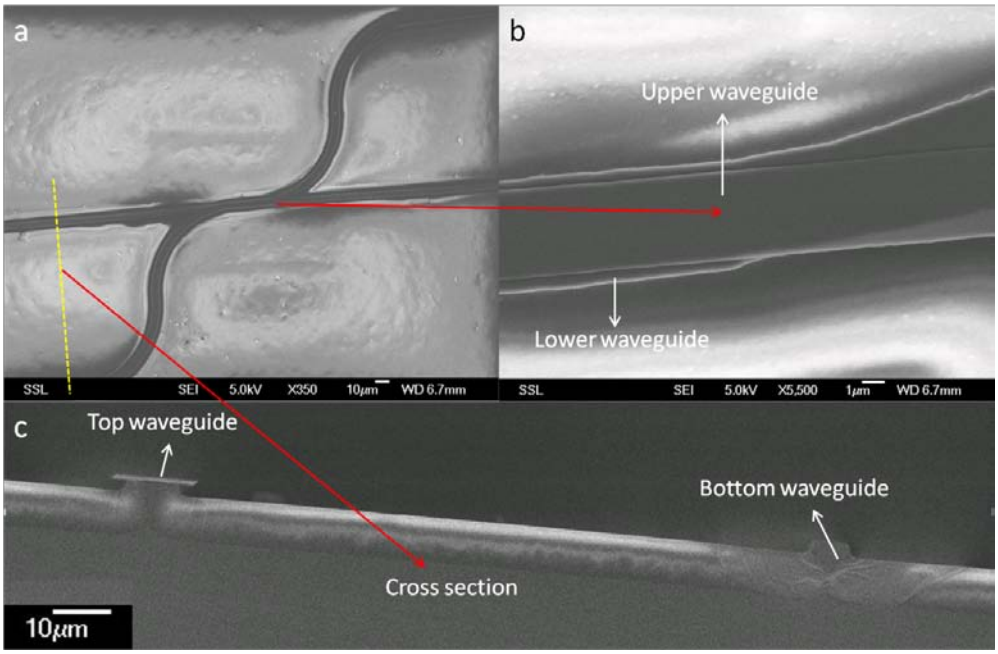

Fig 6. 13 SEM images of the first attempt of vertical coupling waveguides (a) over view of the structures, (b) high magnification view of the coupling region, (c) cross section view of the two waveguides.

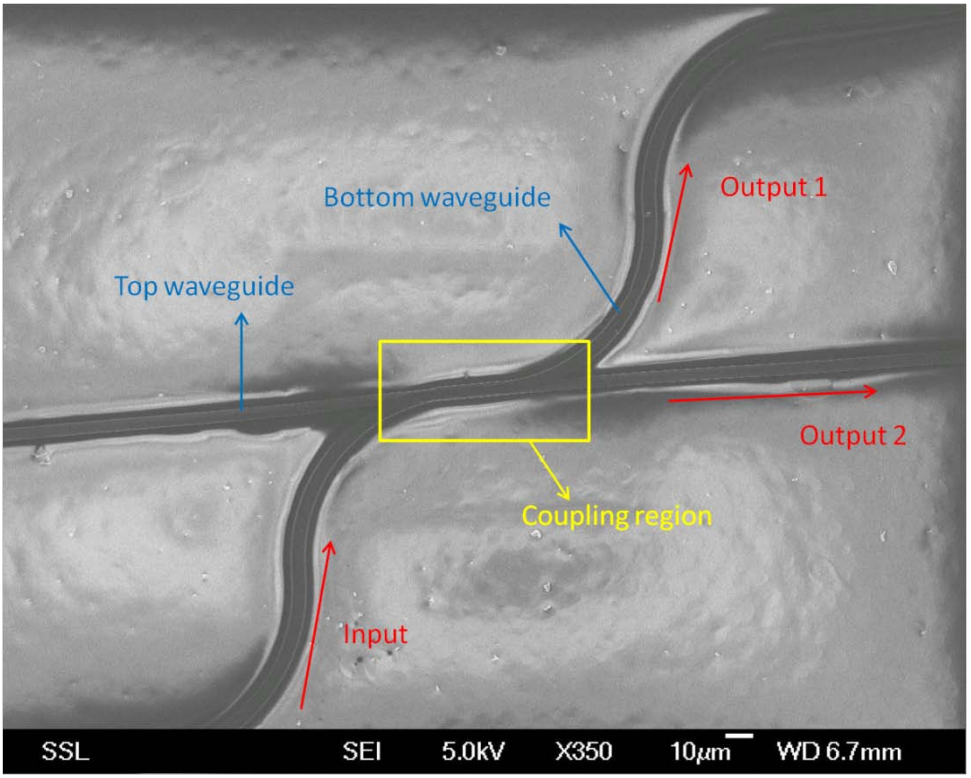

Fig 6. 14 Schematic of the light coupling between the two layer waveguides.

The coupling lengths were designed as 20 μm, 40 μm, 80 μm, 160 μm, 320 μm, 400 μm 500 μm, and 600 μm. Such a big range and maximum length were to make sure there is enough coupling to be obtained. Four energies (50 keV, 55 keV, 100 keV and 200 keV) of protons were used for patterning the lower waveguides at the coupling region, to test the affect of the thickness of the lower waveguides on the coupling efficiency. We can vary the ion energies along the waveguides to make them with vertically tapered profiles, thin at the central coupling region and thick at the ends. The thickness of the upper waveguides was fixed by the device layer thickness, as 230 nm.

The schematic of the light coupling between the two layer waveguides is shown in Fig 6.14. First, incident light was coupled from an optical fiber or lens into the lower waveguide. When the light through the waveguide arrived at the coupling region, some of it was coupled into the upper waveguide, and remained in the lower waveguide. So after the coupling region, we obtained two outputs, one from the lower waveguide from transmission, Output 1, one from the upper waveguide from coupling, Output 2.

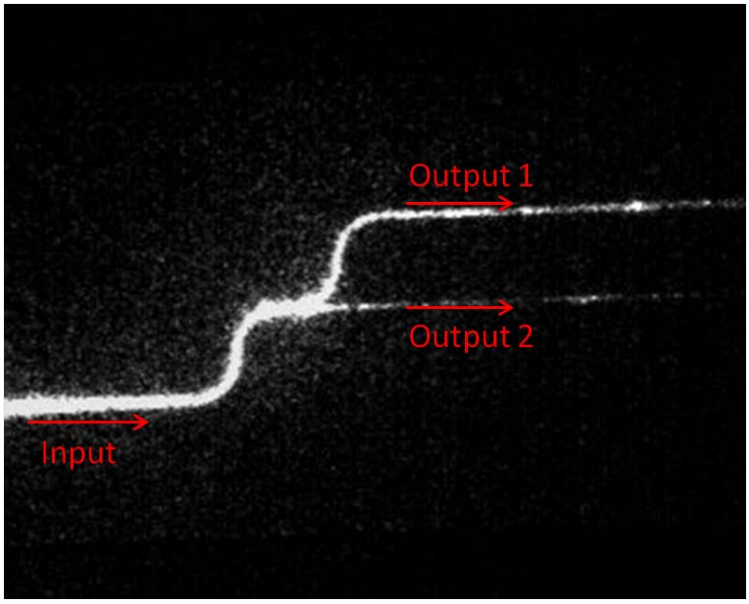

Fig 6. 15 IR images of the light coupling from the lower waveguide to the upper waveguide.

Optical characterization was carried out with a tunable laser with wavelength range from 1530 nm to 1570 nm. The laser was coupled into the waveguide using a 60× objective lens. A InGaAs IR camera was used to monitor the scattered light from the top of the sample. Fig. 6.15 shows light coupling between the two layers of waveguides, viewing the scattered light from the top of the structure. The incident light was with wavelength 1.55 μm and TE mode. And the coupling length in this case was set as 20 μm. Light was successfully coupled from the lower waveguide into the upper waveguide, and the efficiency seemed to be quite high, but the propagation loss of the upper waveguide was significant.

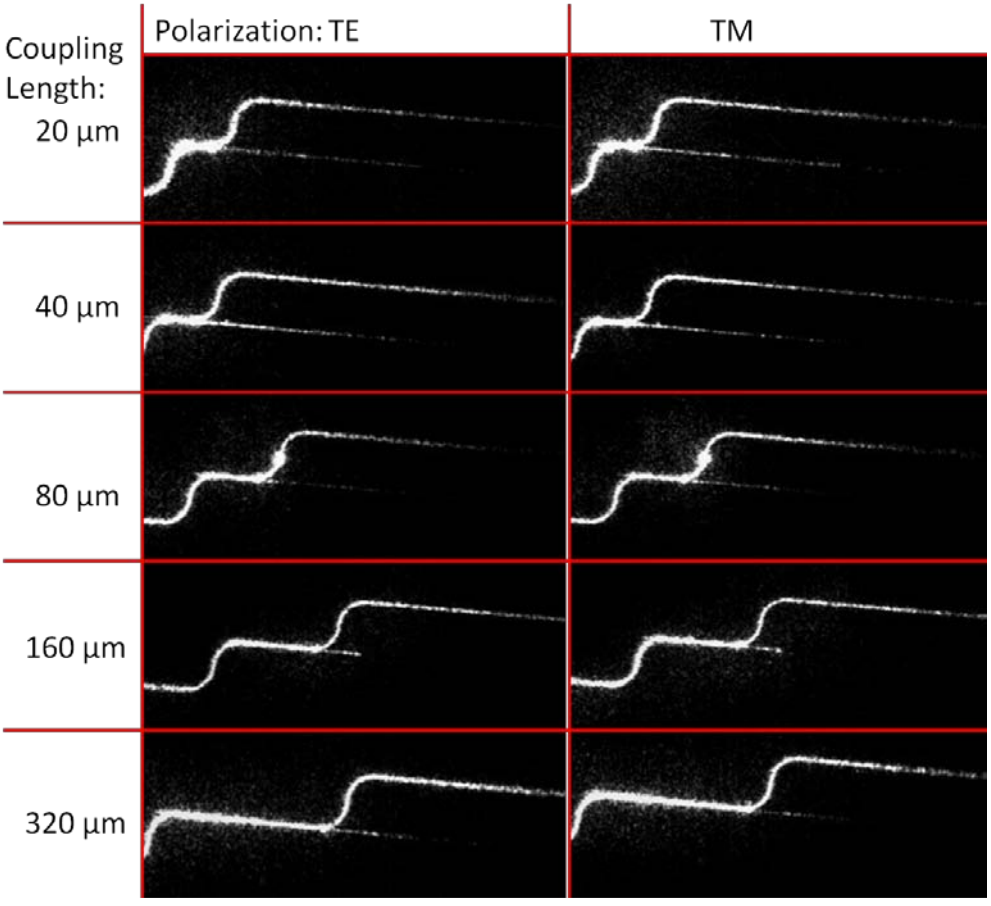

Fig 6. 16 IR images of the light coupling for different coupling lengths and incident light polarizations.

Different coupling lengths would result in different coupling efficiencies. According to Fig 6.16, a coupling length of 20 μm was long

enough to give us an efficient coupling between the two layer waveguides. When the coupling length increased beyond 20 μm, the coupling efficiency was not increased, it even decreased as the coupling length extended beyond 80 μm. So an efficient coupling length should be within 20 μm. Different polarization of the incident light would result in slight different coupling efficiency, but not significant.

6.3.2 Simulations

To better understand the light coupling between the two layer waveguides, and to optimize the designs, simulations were carried out using the Rsoft, BeamPROP software. The structure was simplified in the simulation for easy run of the software. A schematic of the simulation structure is shown in Fig 6.17. The wafer plane is in XZ plane, the waveguides go through Z direction. Between the silicon substrate and the waveguides, there is a layer of 5 μm thick oxidized porous silicon. The lower waveguide lies on the porous silicon layer, and the upper waveguide suspends over the lower waveguide.

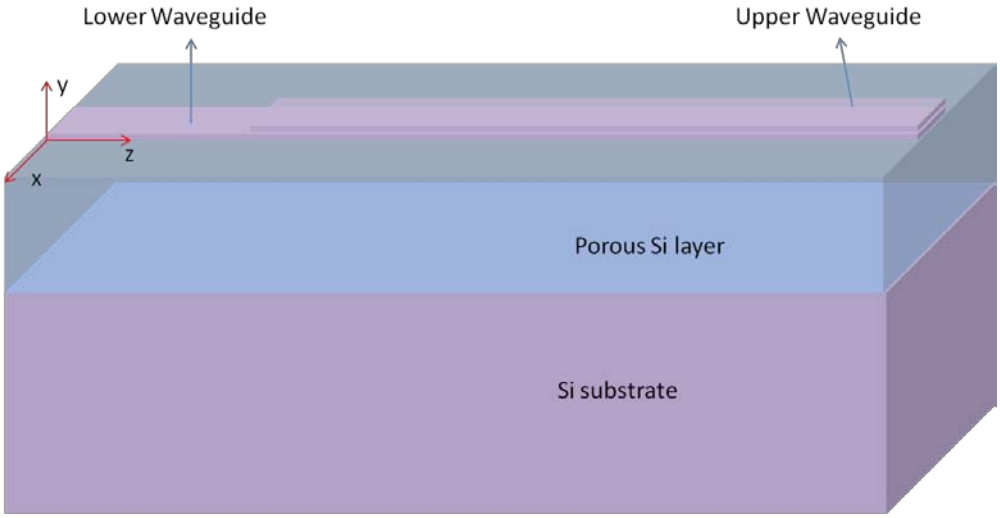

Fig 6. 17 Schematic of the simulation structures. The substrate width and thickness: 10um, porous Si thickness: 5um, waveguides width: 5um. The thicknesses of the two waveguides and the gap varied.

The width and thickness of the waveguides and the gap between them can be varied. Since the SOI wafer had fixed device and oxide layer thicknesses, we set the upper waveguide thickness as 230 nm, and the gap as 145 nm. The width of the waveguides was also set as 5 μm. As we varied the thickness of the lower waveguide, the coupling efficiency varied, as shown in Fig 6.18. When the lower waveguide had an equivalent thickness with the upper, 230 nm, the light could be fully coupled from the lower into the upper. The light would be coupled back and forth between the two layer waveguides periodically. As the lower waveguide thickness increases, the maximum coupling efficiency would decrease significantly. For example, with a lower waveguide thickness 400 nm, the maximum coupling efficiency is reduced to only ~30%.

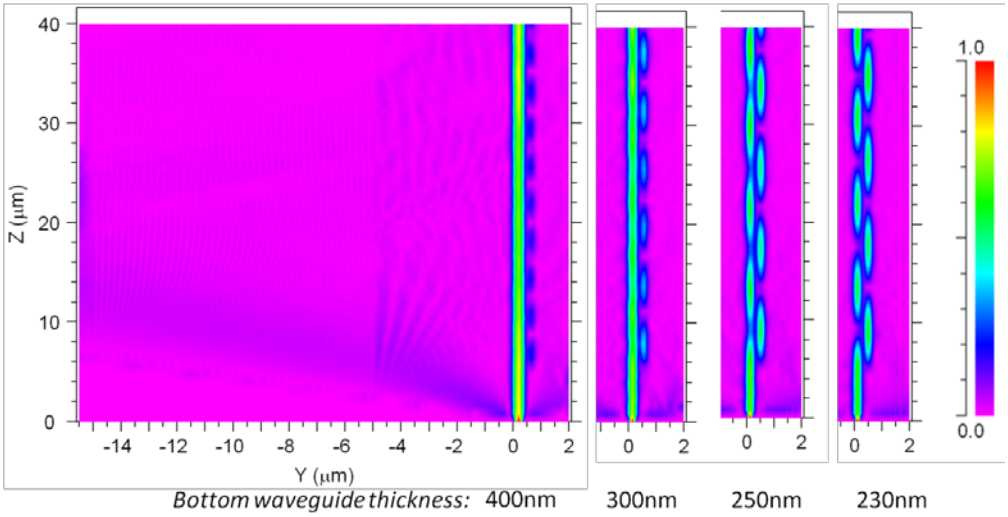

Fig 6. 18 Different lower waveguide thicknesses result in different coupling efficiencies.

In the experiments, the upper waveguides were usually bent down to attach on the lower waveguides. So we further simplify the structures like shown on the top of Fig. 6.19. The incoming light wavelength is set as 1550 nm, on changing it between 1530 nm to 1570 nm the results are almost constant for a coupling length of 20 μm. As the device layer of the SOI wafer is fixed, the thickness of the upper waveguide is fixed at T_U = 230 nm. As discussed above, the two waveguides are almost in contact, so the gap between

them is set as zero. Their width is designed as 4.5 μm. Experimentally the proton beam energy which is used to define the lower waveguide can be varied in order to change its thickness T_L, in the simulations, we studied

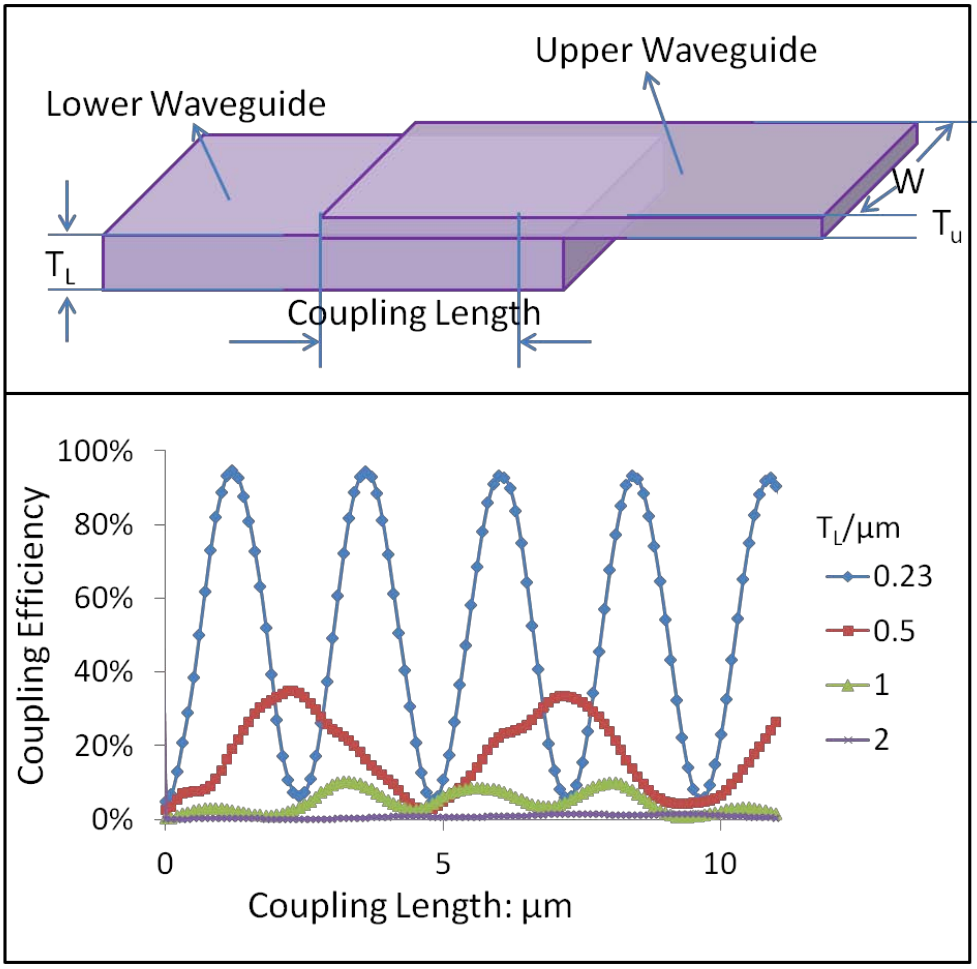

Fig 6. 19 Simulation results: upper shows a schematic of the simulated structure, the waveguides width W and the upper waveguide thickness T_U are fixed. The two waveguides are attached, the lower waveguide thickness T_L is varied; lower: plots the coupling efficiency for different T_L along a coupling length of 11μm.

thicknesses from 0.1 μm to 2 μm. Fig. 6.19 shows the coupling efficiency of four different thicknesses (T_L = 0.23 μm, 0.5 μm, 1 μm, 2 μm) along a coupling length of 11 μm. With T_L = 0.23 μm, the simulated maximum coupling efficiency is over 90% within a coupling length of 1.2 μm. However, very accurate control over the dimensions is required to utilize such high coupling efficiency. For T_L = 0.5 μm, the maximum coupling efficiency decreases to ~35%, but the tolerance of the required dimensions increases. For

T_L = 1 μm and 2 μm, the coupling efficiency is below 10% and 2% respectively. To summarize, when two waveguides are of a similar thickness, the maximum coupling efficiency is very high, and the maximum coupling efficiency rapidly decreases with increasing T_L. In simulations, a gap of 0.2 μm between the two layers of waveguides was found to produce strongly polarization-dependent results, whereas when the gap is close to zero, the polarization dependence is very weak.

6.3.3 Further optimization and simulations

According to the simulations, thinner lower waveguides could give out higher coupling efficiency, and efficient coupling length could be only within several microns. So we made the new designs with coupling lengths as 2 μm, 5 μm. However, because of the curved tails of the lower waveguides, the actual coupling length was much more than those. For example, the one in Fig 6.20 was designed with a coupling length of 2 μm, but had a coupling length of ~21 μm in the final structure. This is because that the waveguides width was big, and so they should have a large curving radius to minimize

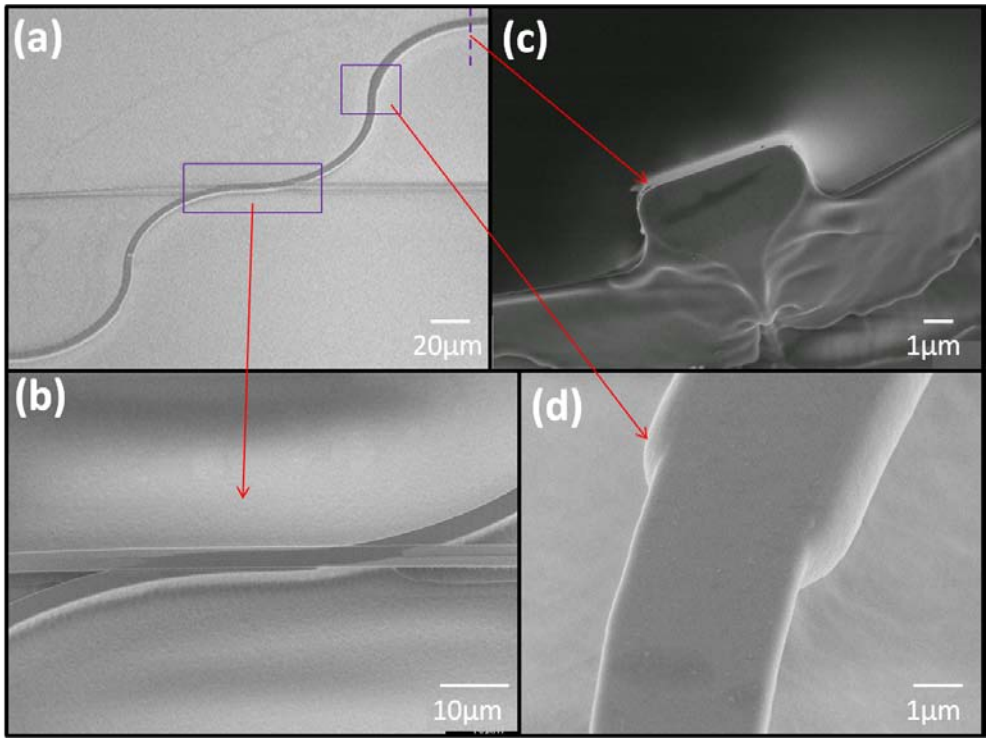

Fig 6. 20 SEM images of the structure, showing low magnification views of (a) the full structure and (b) the coupling region, (c) high magnification cross

section of the thick lower waveguide (~5.4 μm×2.5 μm), (d) plan view of the tapered portion of the lower waveguide.

the propagation loss at the curved part which made the actual coupling length much bigger than designed. The big width of the waveguides was mainly limited by the UV lithography. If using thinner waveguides made by Ebeam or deep UV lithography, the radius of the curve could be reduced, and hence the coupling length could be really reduced to several microns.

In Fig 6.20 (d), we can see there is a tapered portion along the lower waveguide. That is the conjunction of the thick and thin portions of the lower waveguide. On the one hand, we used a low energy (50 keV) proton beam to irradiate the coupling region of the lower waveguide to obtain a thin lower waveguide at that region, and finally to achieve a high coupling efficiency. On the other hand, for easily coupling light from an optical fiber of lens into the waveguide, a thick waveguide port is necessary. So we used a higher energy (200 keV) proton beam to irradiate other portion at the ends of the waveguide that was away from the coupling region, to obtain thick input and output ports of the waveguide for easy light coupling.

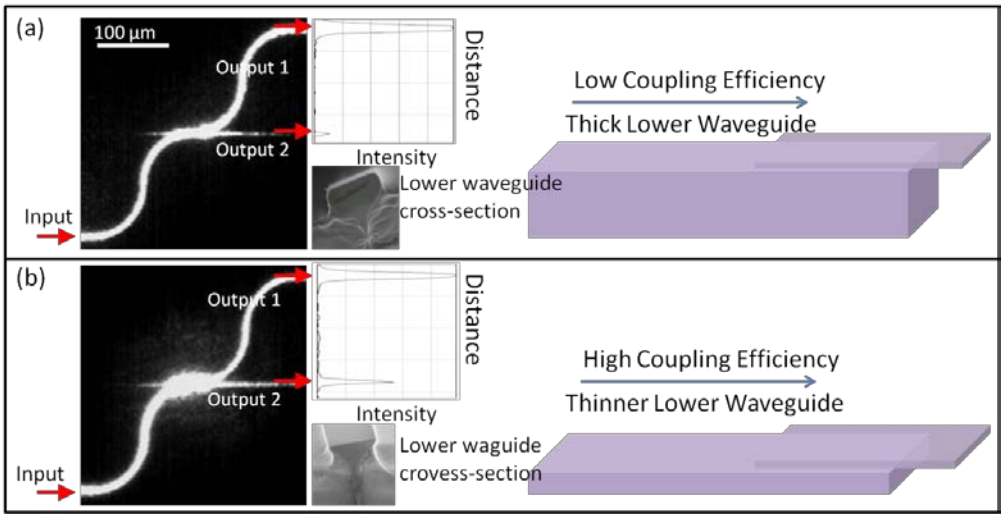

Fig 6. 21 Thinner lower waveguide gives out higher coupling efficiency.

To study the dependence of the coupling efficiency on the lower waveguide thickness, we had both lower waveguides with and without tapering at the coupling region. Simple line scans of the two outputs scattered light could easy show the different coupling efficiencies of the two cases, lower waveguides with and without tapering, Fig 6.21. When the lower waveguide was without tapering at the coupling region, so was thick at that region, the coupling efficiency was quite low, Fig 6.21 (a). If there was a tapering portion, so the lower waveguide was thin at the coupling efficiency, it resulted in a much higher coupling efficiency, Fig 6.21 (b). This agreed well with the simulations.

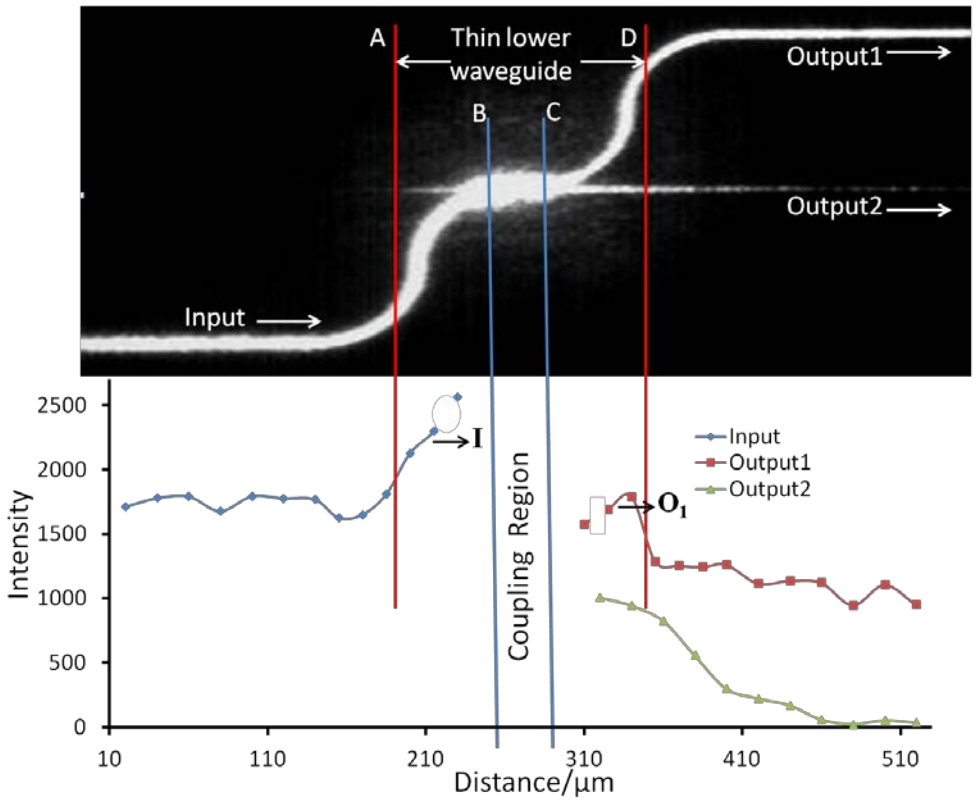

Fig 6. 22 IR image and scan of the scattering light intensity along the waveguides.

When the lower waveguide has a sub-micron thickness at the coupling region, Fig. 6.22 shows light coupling between the two layers of waveguides, viewing the scattered light from the top of the device, and scattered light intensity measurements along the waveguides. Along the thin portion of the

lower waveguide (A to B, and C to D), there is more scattered light, in keeping with a thinner, curved geometry. However, measurement of scattered light from this portion is also influenced by its proximity to the coupling region, where a high background intensity of scattered light surrounding this region is observed. Because of this, the closest data points on either side of the coupling region are deemed to be not valid for the purpose of measuring the coupling efficiency, so are not joined to the main curve. The measured coupling efficiency of 26% ±10%, defined as the (Input-Output1)/Input, with the values of I (Input) and O_1 (Output1) chosen as the average of the two valid data points in Fig. 6.22 which are close to the coupling region, within the zones A to B, and C to D. For other similarly-fabricated samples, we measured coupling efficiencies ranging from 16 to 35% with single wavelengths or broad band light, compared to only ~3% measured in a sample where the lower waveguide was much thicker (~2.5 μm) at the coupling region. We believe that the measured variations of the coupling efficiency largely arise from limitations of the normal UV lithography and UV alignment. The coupling efficiency is similar to that achieved using a typical grating coupler[134, 135]. The loss from the upper waveguide could be reduced with a shorter free-standing length and optimization of the UV lithography and RIE steps.

From SRIM, a lower proton energy of 50 keV can produce a lower waveguide thickness of about 200 nm at the coupling region. However, usually there is a 'tail' remaining after electrochemical anodization, inset of Fig. 6.21(b) which results in an almost triangular profile of the lower waveguide. In the simulations in Fig. 6.23, we incorporated a more realistic triangular profile of the lower waveguide, having a width of 4.5μm and a maximum thickness of 1μm. With such a triangular profile, the coupling efficiency reaches around 27% at a coupling length of 22 μm, which is higher than what would typically be achieved for a uniform thickness of T_L = 1 μm in Fig. 6.19. And this result also agreed well with the experiment. If necessary, this tail portion may be removed by reducing the width of the lower waveguide from its present value to ~1 μm, based on our previous experience [136].

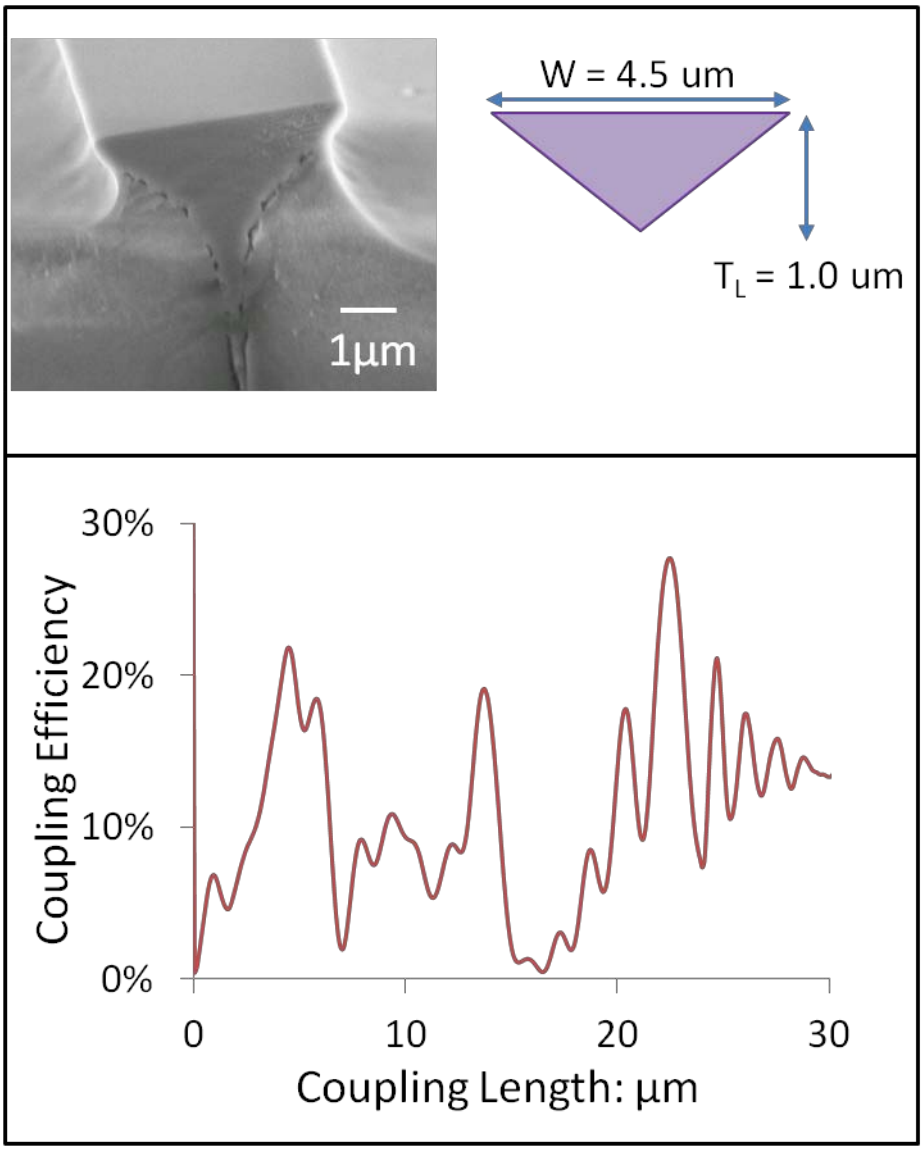

Fig 6. 23 Simulation results: upper shows the actual triangular profile of the lower waveguide and simplified triangular profile used in the simulation; lower: plots the coupling efficiency of this profile.

The propagation loss is measured by measuring the scattered light along a 3 mm length for the lower waveguide and a 1 mm length for the upper waveguide. Light was injected into each one in turn, with the coupling region playing no part in the measurements. From the measurements, losses of ~3dB/cm for the thick lower waveguide and ~60dB/cm for the upper waveguide were recorded. The loss of ~60dB/cm through the upper waveguide is significant, presumably arising from its high roughness. Along the lower waveguide, there are two different parts: the thin coupling region

and the thick portion away from the coupling region. The measured loss is that of the thick portion as the thin portion is short, curved and some portion of it interacts with the upper waveguide at the coupling region, making a meaningful loss measurement very difficult. However, from the straight end of Input to the straight beginning of Output1, a total loss of ~32% was measured, so apart from a 26% coupling, it suggests a total loss of 6%, including the tapering loss, bending loss and propagation loss through the whole thin part.

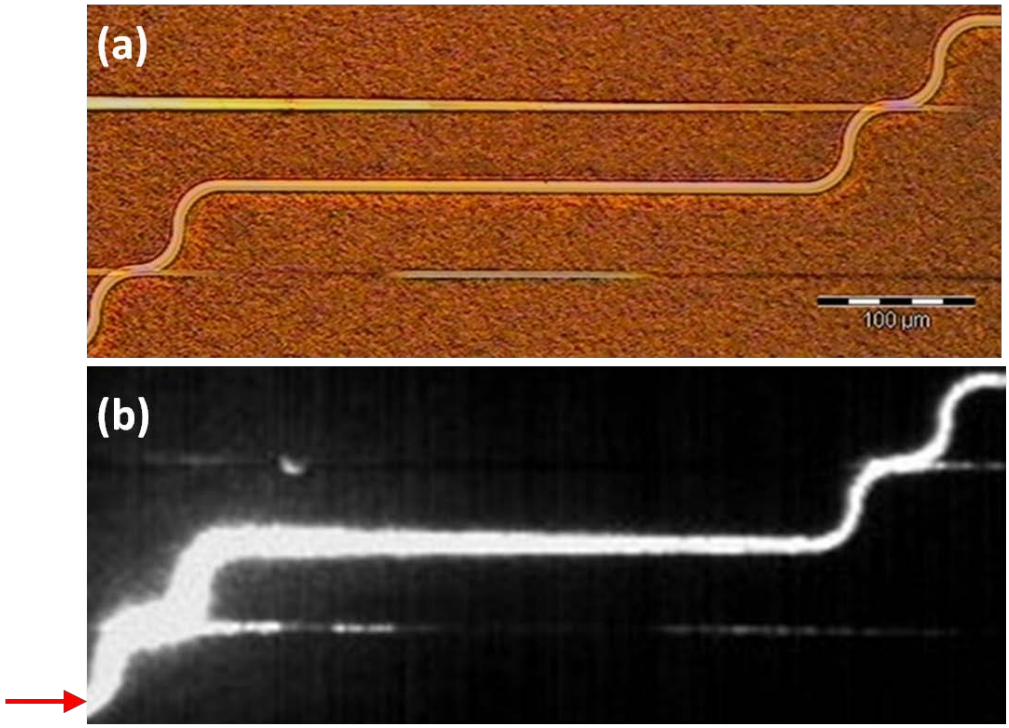

Fig 6. 24 One lower waveguide coupling light into two upper waveguides. Arrow shows location of incident light in the lower waveguide.

According to simulation results using Rsoft, the coupling efficiency mainly depends on the gap between the two layer waveguides, the coupling length and the waveguide thicknesses. When waveguide thicknesses are small, 200 nm-300 nm, and identical, with a small gap of <300nm, the coupling efficiency can be over 90% within a very short coupling length (<3um). In our experiment, the gap depends on the thickness of the oxide layer of the SOI wafer and the bending of the top waveguide; the coupling length can be

defined by the design; the top waveguide thickness depends on the thickness of the device layer, while the bottom waveguide thickness depends on the energy of the proton beam. With a fixed kind of SOI wafer, we can tune the gap by the natural bending of the free standing part of the top waveguide, and tune the thickness of the bottom waveguide with different proton beam energy to get different coupling efficiency for different purposes. For example, while we can reduce the bottom waveguide thickness to improve the coupling efficiency, as shown in Fig. 6.21, we can also use a thick bottom waveguide which gives a lower coupling efficiency but to couple the light from one bottom waveguide to several different top waveguides as shown in Fig. 6.24.

6.4 Summary

To summarize, a vertical coupling structure fabrication process using a combination of RIE and proton beam irradiation followed by an electrochemical etching on an SOI wafer is demonstrated. In the vertically coupled waveguides, reasonably efficient light coupling of ~16 to 35% between the two layers of waveguides was obtained. Such vertically-coupled waveguides could work as vertical-coupling directional splitters or as simple, high-efficiency vertical-couplers and the same fabrication process can be further applied to fabricate other vertical coupling structures such as waveguide-to-microresonators.

Further work is aimed at optimizing the fabrication process to improve the repeatability of the coupling efficiency using deep UV or Ebeam alignment.

Chapter 7

Conclusion and Discussions

This study has further developed the silicon micro- and nano-machining process via ion beam irradiation in two aspects: studying different etching behaviors after irradiation with high and low energy ion beams; and studying the effect of a forced current to produce high resolution structures. While the results showed a reduction of etching rate after high energy ion beams irradiation, there was an undercutting limit during electrochemical etching after irradiation by low energy ion beams. High energy ion beams have a deep trajectory and form a thick defect layer with a distribution of lower density near the surface and a high density peak at the end of range. This results in a continuous and gradual progress with a reduced etching rate. The shallow defect layer induced by low energy ion beams is too thin to have any significant longitudinal distribution, and unable to give out any gradual process, but result in an abrupt effect with an undercutting limit. This result gives us a better understanding of the ion beam irradiation effect on the electrochemical etching of p-type silicon, and provides a general guide on all other related works. Force current study was carried out in the fabrication of integrated 2D microresonator-waveguides section to achieve the small gaps. The forced current approach improved the structure resolution very little. It seems that the resolution limit is more likely to be caused by the overlap of the two adjacent line irradiations, which is because of the scattering of the beam in the material.

Fabrication of 2D photonic structures such as waveguides, splitters, microdisk and microring resonators on bulk silicon were demonstrated in this thesis. All these photonic devices can be fabricated with a single etching step on bulk silicon wafers. This provides a novel solution to obtaining photonic structures on bulk silicon other than SOI platforms, and so reduces the cost. Fabrication of integrated 2D microresonator-waveguides were also carried out. However, we failed to obtain an effective integrated structure, as there was a limitation of the gap between the waveguide and resonator during the fabrication process. To achieve an efficient coupling between the waveguide and resonator, the gap should be down to ~100 nm, but the smallest gap obtained by this process was 400 - 500 nm. This is a limitation of the fabrication process as there is a significant ion beam scattering at the end of range, and a deflection of the electric field at two close defect regions. This limitation could be solved by either improving the fabrication process or using a MEMs approach to further reduce the gap after fabrication process.

3D beam splitters were also fabricated on bulk silicon. This demonstrated the ability of achieving 3D photonic structures on bulk silicon using multiple energies of ion beam irradiation and then all produced by a single etching step.

Optical characterization was performed for 2D and 3D beam splitters. The results of 2D Y-shape splitters showed a polarization difference between the two arms: with TE modes propagating through one arm, and with TM modes through the other. It was also simulated with Rsoft which showed the same result as the characterization. Moreover, the polarization of the two arms was tunable as we varied the lengths of the arms and wavelength of the input light. This could be used as a practical tunable polarization dependence splitter. 3D splitters have shown weak light coupling to the two upper arms. This is probably because that they were too thin compared to the lower arm. This could be improved by making the arm with same dimensions in future work.

This ion beam irradiation induced silicon machining process was also applied on SOI platforms. Vertically coupled waveguide-waveguides and waveguide-resonators were fabricated using a combination of RIE to fabricate

the upper layer structures on the device layer and ion beam irradiation followed by electrochemical etching to pattern the substrate on SOI wafers. Compared to CVD, epitaxial growth, and wafer bonding, this process is easier and more straightforward, and it has a specific advantage in achieving an all-silicon 3D photonic structures. The process is also compatible with mainly used 2D photonics at present. It provides a novel way of achieving vertically coupled silicon photonic structures on a single SOI wafer.

A typical coupling efficiency of ~26% has been achieved in vertically coupled waveguides. In simulations, the coupling efficiency depends on the widths, thicknesses of the two waveguides and especially the gap between them, and also the coupling length. A small change of these parameters could vary the coupling efficiency a lot. A main limitation at present is that it is difficult to obtain very small size and accurate coupling between the two layers using normal UV lithography. This makes the control over the structure dimensions weak, so the repeatability is also weak. A possible solution to this in the future is to utilize deep UV alignment or e-beam lithography, which could help to achieve smaller structures and more accurate alignment.

In conclusion, ion beam irradiation induced silicon machining process may provide a new way of fabricating 2D and 3D photonic structures on bulk silicon. It is cheaper and easier compared to other techniques. And this process can also be applied to SOI platforms to achieve vertically coupled all-silicon photonic structures, which is also compatible with present 2D photonics on SOI. However, further work is still necessary to improve this process, especially on achieving small sizes and accurate alignment between different layers of structures.

References:

1. Hiruma, T. Photonics. in Proceedings of SPIE. 04/1993.
2. Technical Insights, I., Photonics. Emerging technologies. Vol. no. 51. 1994, NJ.
3. Baba, T., Si photonic wire waveguides. 2004: p. 150-157.
4. Reed, G.T.a.K., Andrew P Silicon photonics: an introduction2004.
5. Hirohito Yamada, T.C., Satomi Ishida, and Yasuhiko Arakawa, Si Photonic Wire Waveguide Devices. IEEE JOURNAL OF SELECTED TOPICS IN QUANTUM ELECTRONICS, 2006. 12(6).
6. Celler, G.K. and S. Cristoloveanu, Frontiers of silicon-on-insulator. Journal of Applied Physics, 2003. 93(9): p. 4955.
7. Marshall, A.N.S. SOI design analog, memory and digital techniques. 2002; Available from: http://site.ebrary.com/id/10067505.
8. Alexe, M.a.G., U, Wafer bonding: applications and technology. Springer series in materials science. Vol. 75. 2004.
9. Grover, R., et al., Vertically coupled GaInAsP--InP microring resonators. Opt. Lett., 2001. 26(8): p. 506-508.
10. Tishinin, D.V., et al., Vertical resonant couplers with precise coupling efficiency control fabricated by wafer bonding. Photonics Technology Letters, IEEE, 1999. 11(8): p. 1003-1005.
11. Lee, M.-C.M. and M.C. Wu, Tunable coupling regimes of silicon microdisk resonators using MEMS actuators. Opt. Express, 2006. 14(11): p. 4703-4712.
12. Worhoff, K., P.V. Lambeck, and A. Driessen, Design, tolerance analysis, and fabrication of silicon oxynitride based planar optical waveguides for communication devices. Lightwave Technology, Journal of, 1999. 17(8): p. 1401-1407.
13. Choi, S.J., et al., Microring resonators vertically coupled to buried heterostructure bus waveguides. Photonics Technology Letters, IEEE, 2004. 16(3): p. 828-830.

14. Dapkus, P.D., et al. Microresonators for Photonic Integrated Circuits. in Optical Fiber communication/National Fiber Optic Engineers Conference, 2008. OFC/NFOEC 2008. Conference on. 2008.
15. Ann Arbor Conference on Optical Pumping, U.o.M.F.P.A.S.R.H. The Ann Arbor conference on optical pumping : the University of Michigan, June 15 through June 18, 1959. Ann Arbor: [s.n.
16. Voumard, C., External-cavity-controlled 32-MHz narrow-band cw GaA1As-diode lasers. Opt. Lett., 1977. 1(2): p. 61-63.
17. Fleming, M. and A. Mooradian, Spectral characteristics of external-cavity controlled semiconductor lasers. Quantum Electronics, IEEE Journal of, 1981. 17(1): p. 44-59.
18. Love, A.W.S.a.J.D., Optical Waveguide Theory1983, London: Chapman and Hall.
19. Lorenzo, R.A.S.a.J.P., Single-crystal silicon: a new material for 1.3 and 1.6 μm integrated-optical components. Electron. Lett., 1985. 21(21): p. 953.
20. Soref, R.A. and J. Larenzo, All-silicon active and passive guided-wave components for λ = 1.3 and 1.6 µm. Quantum Electronics, IEEE Journal of, 1986. 22(6): p. 873-879.
21. Vlasov, Y. and S. McNab, Losses in single-mode silicon-on-insulator strip waveguides and bends. Opt. Express, 2004. 12(8): p. 1622-1631.
22. al., P.D.e., Low-Loss SOI Photonic Wires and Ring Resonators Fabricated With Deep UV Lithography. IEEE PHOTONICS TECHNOLOGY LETTERS, 2004. 16(5): p. 3.
23. al., S.K.S.e., in Leos Annual Meeting2007: Lake Buena Vista, USA.
24. Xia, F., L. Sekaric, and Y. Vlasov, Ultracompact optical buffers on a silicon chip. Nat Photon, 2007. 1(1): p. 65-71.
25. Lee, K.K., et al., Fabrication of ultralow-loss Si/SiO2 waveguides by roughness reduction. Opt. Lett., 2001. 26(23): p. 1888-1890.
26. e.a., H.Y., Optical directional coupler based on Si-wire waveguides. Photonics Technology Letters, IEEE, 2005. 17(3): p. 585 - 587.
27. Fukuda, H., et al., Ultrasmall polarization splitter based on silicon wire waveguides. Opt. Express, 2006. 14(25): p. 12401-12408.

28. Wim Bogaerts, S.K.S., Pieter Dumon, Joost Brouckaert, Katrien De Vos, Dries Van Thourhout, and Roel Baets, Silicon-on-Insulator Spectral Filters Fabricated With CMOS Technology. IEEE JOURNAL OF SELECTED TOPICS IN QUANTUM ELECTRONICS, 2010. 16(1): p. 33-44.
29. Song, J., et al., Effective thermo-optical enhanced cross-ring resonator MZI interleavers on SOI. Opt. Express, 2008. 16(26): p. 21476-21482.
30. Tatsuhiko FUKAZAWA, A.S.a.T.B., H-Tree-Type Optical Clock Signal Distribution Circuit Using a Si Photonic Wire Waveguide. Jpn. J. Appl. Phys., 2002. 41: p. L 1461–L 1463.
31. Morand, A., et al., Ultra-compact microdisk resonator filters on SOI substrate. Opt. Express, 2006. 14(26): p. 12814-12821.
32. Xia, F., et al., Coupled resonator optical waveguides based on silicon-on-insulator photonic wires. Applied Physics Letters, 2006. 89(4): p. 041122-3.
33. Letartre, X., et al., Group velocity and propagation losses measurement in a single-line photonic-crystal waveguide on InP membranes. Applied Physics Letters, 2001. 79(15): p. 2312-2314.
34. Notomi, M., et al., Extremely Large Group-Velocity Dispersion of Line-Defect Waveguides in Photonic Crystal Slabs. Physical Review Letters, 2001. 87(25): p. 253902.
35. A, A.D.J.a.S.R., in Proc. SPIE1987.
36. Soref, R.A., and J.P. Lorenzo, Light-by-Light Modulation in Silicon-on-Insulator Waveguides. OSA Integrated Guided Wave Optics '89, 1989: p. 86-89.
37. Ogura, A., Method of fabricating SOI substrate, 1999: US.
38. Fujioka, H., Method of manufacturing semiconductor on insulator, 1991: US.
39. Gösele, Q.-Y.T.U., SemiConductor Wafer Bonding: Science and Technology1998: Wiley-Interscience.
40. George Bajor, J.S.R., Using a rapid thermal process for manufacturing a wafer bonded soi semiconductor, 1988: US.
41. Nakamura, T., Method for forming SOI structure, 1995: US.

42. R. Pafchek, R.T., J. Li, M. A. Webster, E. Chen, and T. L. Koch, Low-loss silicon-on-insulator shallowridge TE and TM waveguides formed using thermal oxidation. Appl. Opt., 2009. 48(5): p. 958–963.
43. J. Cardenas, C.B.P., J. T. Robinson, K. Preston, L. Chen, and M. Lipson, Low loss etchless silicon photonic waveguides. Opt. Express, 2009. 17(6): p. 4752–4757.
44. F. Y. Gardes, G.T.R., A. P. Knights and G. Mashanovich, Evolution of optical modulators in silicon and novel ways of fabrication, in Photonics West2008: San Jose, CA, USA.
45. Uhlir, A., Electrolytic shaping of germanium and silicon. Bell System Tech. J., 1956. 35: p. 333.
46. N. J. Thomas, J.R.D., J. M. Keen, J. G. Castledine, D. Brumhead, M. Goulding, J. Alderman, J. P. G. Farr, L. G. Earwaker, J. L. Ecuyer, S. I. M, and J. M. Cole, High-performance thin-film silicon-on-insulator cmos transistors in porous anodized silicon. IEEE Electron device letters, 1989. 10: p. 129-131.
47. Partridge, S.L., Silicon-on-insulator technology. IEE Proceedings E, 1986. 133: p. 107-116.
48. Canham, A.C.a.L.T., Visible light emission due to quantum size effects in highly porous crystalline silicon. Nature, 1991. 353: p. 335.
49. A. Halimaoui, C.O., G. Bomchil, A. Bsiesy, F. Gaspard, R. Herinoand, M. Ligeon, and F. Muller, Electroluminescence in the visible range during anodic oxidation of porous silicon films. Appl. Phys. Lett, 1991. 57: p. 1046.
50. Pavesi, L., Porous silicon: a route towards a si-based photonics? Microelectronics Journal, 1996. 27(4-5): p. 437-448.
51. H. Wong, V.F., C. K. Wong, and P. S. Chung, Silicon integrated photonics begins to revolutionize. Microelectronics and Reliability, 2007. 47(1): p. 1-10.
52. T. E. Bell, P.T.J.G., D. DeMunter, and M. Kuhl, Porous silicon as a sacrificial material. Journal of Micromechanics and Microengineering, 1996. 6(4): p. 361-369.

53. M. Navarro, J.M.L., J. Samitier, J. R. Morante, J. Bausells, and A. Merlos, Electrochemical etching of porous silicon sacrificial layers for micromachining applications. Journal of Micromechanics and Microengineering, 1996. 7: p. 131-132.
54. A. Benilov, M.C., V. Skryshevsky, and J. R. Martin, Porous silicon localization for implementation in matrix biosensors. Materials Science and Engineering: B, 2007. 139(2-3): p. 221-225.
55. V. Lysenko, P.R., G. Delhomme, V. Rossokhaty, V. Strikha, A. Dittmar, D. Barbier, N. Jaffrezic-Renault, and C. Martelet, Oxidized porous silicon: a new approach in support thermal isolation of thermopile-based biosensors. Sensors and Actuators A: Physical, 1998. 67(1-3): p. 205-210.
56. Rendina, I., Rea, Ilaria, Rotiroti, Lucia, D. Stefano, and Luca, Porous silicon-based optical biosensors and biochips. Physica E: Low-dimensional Systems and Nanostructures, 2007. 38(1-2): p. 188-192.
57. Lehmann, V., Electrochemistry of silicon: Instrumentation, science, materials and applications2002: Wiley-VCH.
58. L. Jia, S.L.Z., S. P. Wong, I. H. Wilson, S. K. Hark, Z. F. Liu, and S. M. Cai, Further evidence for the quantum confined electrochemistry model of the formation mechanism of p(-)-type porous silicon. Applied Physics Letters, 1996. 69(22): p. 3399-3401.
59. Gosele, V.L.a.U., Porous silicon formation - a quantum wire effect. Applied Physics Letters, 1991. 58(8): p. 856-858.
60. E. Teo, M.B., A. Bettiol, D. Mangaiyarkarasi, F. Champeauz, F. Watt, and D. Blackwood, Multicolour photoluminescence from porous silicon using focused high-energy helium ions. Advanced Materials, 2006. 18: p. 51-55.
61. JF, Z., Srim-2003. Nuclear Instruments and Methods in Physics Research Chapterion B-Beam Interactions with Materials and Atoms, 2004. 219: p. 1027-1036.
62. M. B. H. Breese, F.J.T.C., E. J. Teo, A. A. Bettiol, and D. J. Blackwood, Hole transport through proton-irradiated p-type silicon

wafers during electrochemical anodization. Physical Review B, 2006. 73: p. 035428.

63. F. Watt, J.A.v.K., I. Rajta, A. A. Bettiol, T. F. Choo, M. B. H. Breese, and T. Osipowicz, The national university of singapore high energy ion nano-probe facility: Performance tests. Nuclear Instruments and Methods in Physics Research Chapterion B: Beam Interactions with Materials and Atoms, 2003. 210: p. 14-20.
64. D. J. W. Mous, R.G.H., T. Butz, R. H. Flagmeyer, D. Lehmann, and J. Vogt, The novel ultrastable hvee 3.5 mv singletron(tm) accelerator for nanoprobe applications. Nuclear Instruments and Methods in Physics Research Chapterion B: Beam Interactions with Materials and Atoms, 1997. 130(1-4): p. 31-36.
65. F. Watt, M.B.H.B., A. A. Bettiol, and J. A. van Kan, Proton beam writing. Materials Today, 2007. 10(6): p. 20-29.
66. P. G. Shao, J.A.v.K., K. Ansari, A. A. Bettiol, and F. Watt, Poly (dimethyl siloxane) micro/nanostructure replication using proton beam written masters. Nuclear Instruments and Methods in Physics Research Chapterion B-Beam Interactions with Materials and Atoms, 2007. 260(1): p. 479-482.
67. P. G. Shao, J.A.v.K., L. P. Wang, K. Ansari, A. A. Bettiol, and F. Watt, Rapid prototyping of micro/nano poly (methyl methacrylate) fluidic systems using proton beam writing. Nuclear Instruments and Methods in Physics Research Chapterion B-Beam Interactions with Materials and Atoms, 2007. 260(1): p. 362-365.
68. T. C. Sum, A.A.B., H. L. Seng, I. Rajta, J. A. van Kan, and F. Watt, Proton beam writing of passive waveguides in pmma. Nuclear Instruments and Methods in Physics Research Chapterion B-Beam Interactions with Materials and Atoms, 2003. 210: p. 266-271.
69. J. A. van Kan, P.G.S., K. Ansari, A. A. Bettiol, T. Sipowicz, and F. Watt, Proton beam writing: a tool for high-aspect ratio mask production. Microsystem Technologies-Micro-and Nanosystems-Information Storage and Processing Systems, 2007. 13(5-6): p. 431-434.

70. W. S. Yue, S.Y.C., Y. P. Ren, J. A. van Kan, T. Osipowicz, L. K. Jian, H. O. Moser, and F. Watt, The fabrication of x-ray masks using proton beam writing. Journal of Micromechanics and Microengineering, 2008. 18(8).
71. S. Gorelick, F.Z., P.G. Shao, J.A. van Kan, Harry J. Whitlow, F. Watt, Adhesion of proton beam written high aspect ratio hydrogen silsesquioxane (HSQ) nanostructures on different metallic substrates. Nuclear Instruments & Methods in Physics Research Section B, 2009. 267: p. 3314-3318.
72. Shao Peige, J.A.v.K., Frank Watt, Sub Micron Poly-Dimethyl Siloxane (PDMS) Replication Using Proton Beam Fabricated Nickel Moulds. Sub Micron Poly-Dimethyl Siloxane (PDMS) Replication Using Proton Beam Fabricated Nickel Moulds, 2010(447-448): p. 452-455.
73. J. A. van Kan, P.M., and Armin Baysic de Vera, The second generation Singapore high resolution proton beam writing facility. Review of Scientific Instrumnets, 2012. 83(02B902).
74. Harry J. Whitlow, M.R., Jeroen A. van Kan, Thomas Osipowicz, Frank Watt, Angular and lateral spreading of ion beams in biomedical nuclear microscopy. Nuclear Instruments & Methods in Physics Research B, 2009. 267: p. 2153-2156.
75. M.D. Ynsa, M.Q.R., R. Rajendran, J.N. Sidhapuriwala, J.A. van Kan, M. Bhatia, and F. Watt, Zinc Mapping and Density Imaging of Rabbit Pancreas Endocrine Tissue Sections Using Nuclear Microscopy. Microsc. Microanal, 2009. 15: p. 345-352.
76. Chen Xiao, C.N.U., Chen Ce-Belle, Andrew Bettiol, Daniel Pickard, T. Venkatesan and Frank Watt, Whole cell imaging using fast and slow helium ions. Biophysical Journal, 2011. 101: p. 1788-1793.
77. F. Watt, X.C., Armin Baysic De Vera, C. N. Udalagama, Ren Minqin, J. A. van Kan, A. A. Bettiol, The Singapore high resolution single cell imaging facility. Nuclear Instruments & Methods in Physics Research B, 2011. 269: p. 2168-2174.

78. D. Mangaiyarkarasi, O.Y.S., Mark B. H. Breese, Vincent L. S. Fuh, and Eric Tang Xioasong, Fabrication of large-area patterned porous silicon distributed Bragg reflectors. Optics Express, 2008. 16: p. 12757.
79. TT. Osipowicz, H.L.S., T.K. Chan and B. Ho, The CIBA high resolution RBS facility. Nuclear Instruments and Methods in Physics Research, Section B, 2006. 249: p. 915-917.
80. Breese, M.B.H., Monte carlo simulations of a magnetic quadrupole triplet as a high resolution energy spectrometer. Nuclear Instruments and Methods in Physics Research Chapterion B: Beam Interactions with Materials and Atoms, 2000. 171(4): p. 565-572.
81. Jamieson, M.B.H.B.a.D.N., The use of a magnetic quadrupole triplet as a high resolution ion energy spectrometer. Nuclear Instruments and Methods in Physics Research Chapterion B: Beam Interactions with Materials and Atoms, 1999. 155(1-2): p. 153-159.
82. Watt, G.W.G.a.F., Focusing protons and light ions to micron and submicron dimensions. Nuclear Instruments and Methods in Physics Research Chapterion B: Beam Interactions with Materials and Atoms, 1988. 30(3): p. 227-234.
83. A. A. Bettiol, C.N.B.U., J. A. v. Kan, and F. Watt, Ionscan: scanning and control software for proton beam writing. Nuclear Instruments and Methods in Physics Research Chapterion B: Beam Interactions with Materials and Atoms, 2005. 231(1-4): p. 400-406.
84. A. A. Bettiol, J.A.v.K., T. C. Sum, and F. Watt A labview(tm)-based scanning and control system for proton beam micromachining. Nuclear Instruments and Methods in Physics Research Chapterion B: Beam Interactions with Materials and Atoms, 2001. 181(1-4): p. 49-53.
85. E. J. Teo, A.A.B., B. Xiong, M. B. H. Breese, P. Yang, G. Z. Mashanovich, and G. T. Reed, Low loss silicon-on-oxidised porous silicon strip waveguides fabricated by focused proton beam irradiation. Optics Letters, 2009. 34.
86. J. Song, Z.Y.D., S. Azimi, M. B. H. Breese, J. Forneris and E. Vittone, On the formation of 50nm Diameter free-standing silicon wires

produced by ion irradiation. ECS Journal of Solid State Science and Technology, 2012. 1: p. 66-69.

87. E.J. Teo, A.A.B., B.Q. Xiong, Fabrication of smooth silicon optical devices using proton beam writing. Nuclear Instruments & Methods in Physics Research B, 2011. 269: p. 2448-2451.
88. D. K. Armani, T.J.K., S. M. Spillane & K. J. Vahala, Ultra-high-Q toroid microcavity on a chip. Nature, 2003. 421.
89. Vahala, K.J., Optical microcavities. Nature, 2003. 424.
90. McCall, S.L., Levi, A. F. J., Slusher, R. E., Pearton, S. J. & Logan, R. A, Whispering-gallery mode microdisk lasers. Appl. Phys. Lett., 1992. 60: p. 289-291.
91. Sandoghdar, V.e.a., Very low threshold whispering-gallery-mode microsphere laser. Phys. Rev. A, 1996. 54: p. R1777–R1780.
92. Lefevre-Seguin, V.H., S., Towards cavity-QED experiments with silica microspheres. Mater. Sci. Eng. B, 1997. 48: p. 53-58.
93. Vernooy, D.W., Furusawa, A., Georgiades, N. P., Ilchenko,V. S. & Kimble, H. J., Cavity QED with high-Q whispering gallery modes. Phys. Rev. A, 1998. 57: p. R2293–R2296.
94. Chang, R.K.C., A. J., Optical Processes in Microcavities, in World Scientific1996: Singapore.
95. Treussart, F.e.a., Evidence for intrinsic Kerr bistability of high-Q microsphere resonators in superfluid helium. Eur. Phys. J. D, 1998. 1: p. 235-238.
96. Spillane, S.M., Kippenberg, T. J. & Vahala, K. J, Ultralow-threshold Raman laser using a spherical dielectric microcavity. Nature, 2002. 415: p. 621-623.
97. Vollmer, F.e.a., Protein detection by optical shift of a resonant microcavity. Appl. Phys. Lett., 2002. 80: p. 4057–4059.
98. Serpenguzel, A., Arnold, S. & Griffel, G., Excitation of resonances of microspheres on an optical fiber. Opt. Lett., 1995. 20: p. 654-656.
99. Gerard, J.M.e.a., Quantum boxes as active probes for photonic microstructures: The pillar microcavity case. Appl. Phys. Lett., 1996. 69: p. 449-451.

100. Painter, O.e.a., Two-dimensional photonic band-gap defect mode laser. Science, 1999. 284: p. 1819-1821.
101. Xu, Q., et al., Experimental Realization of an On-Chip All-Optical Analogue to Electromagnetically Induced Transparency. Physical Review Letters, 2006. 96(12).
102. Eichenfield, M., et al., A picogram- and nanometre-scale photonic-crystal optomechanical cavity. Nature, 2009. 459(7246): p. 550-5.
103. Wiederhecker, G.S., et al., Controlling photonic structures using optical forces. Nature, 2009. 462(7273): p. 633-6.
104. Van Thourhout, D. and J. Roels, Optomechanical device actuation through the optical gradient force. Nat Photon, 2010. 4(4): p. 211-217.
105. Lin, Q., et al., Coherent mixing of mechanical excitations in nano-optomechanical structures. Nat Photon, 2010. 4(4): p. 236-242.
106. Witzany, M., et al., Strong mode coupling in InP quantum dot-based GaInP microdisk cavity dimers. New Journal of Physics, 2013. 15(1): p. 013060.
107. Lu, X., et al., Silicon carbide microdisk resonator. Opt. Lett., 2013. 38(8): p. 1304-1306.
108. Ikehara, H., et al., Hitless wavelength-selective switch based on quantum well second-order series-coupled microring resonators. Opt. Express, 2013. 21(5): p. 6377-6390.
109. Werquin, S., S. Verstuyft, and P. Bienstman, Integrated interferometric approach to solve microring resonance splitting in biosensor applications. Opt. Express, 2013. 21(14): p. 16955-16963.
110. Breese, M., et al., Hole transport through proton-irradiated p-type silicon wafers during electrochemical anodization. Physical Review B, 2006. 73(3).
111. Zhang, X. and A.M. Armani, Suspended bridge-like silica 2×2 beam splitter on silicon. Opt. Lett., 2011. 36(15): p. 3012-3014.
112. Jia, W., et al., Design and fabrication of high-efficiency photonic crystal power beam splitters. Opt. Lett., 2011. 36(20): p. 4077-4079.
113. Hosseini, A., et al., Ultracompact and fabrication-tolerant integrated polarization splitter. Opt. Lett., 2011. 36(20): p. 4047-4049.

114. Luc M. Augustin, J.J.G.M.v.d.T., Rabah Hanfoug, Wim J. M. de Laat, Michael J. E. van de Moosdijk, Paul W. L. van Dijk, Yok-Siang Oei, and Meint K. Smit, A Single Etch-Step Fabrication-Tolerant Polarization Splitter. JOURNAL OF LIGHTWAVE TECHNOLOGY, 2007. 25(3): p. 740-746.
115. Isa Kiyat, A.A., Member, and Nadir Dagli, A Compact Silicon-on-Insulator Polarization Splitter. IEEE PHOTONICS TECHNOLOGY LETTERS, 2005. 17(1): p. 100-102.
116. Lin, S., J. Hu, and K.B. Crozier, Ultracompact, broadband slot waveguide polarization splitter. Applied Physics Letters, 2011. 98(15): p. 151101.
117. Lin, S.Y., et al., Low-loss, wide-angle Y splitter at approximately ~1.6- ?m wavelengths built with a two-dimensional photonic crystal. Opt. Lett., 2002. 27(16): p. 1400-1402.
118. Y. Murakami, M.I., and T. Izawa, IEEE J. Quantum Electron, 1981. 17.
119. Wang, Q. and J. Yao, A high speed 2×2 electro-optic switch using a polarization modulator. Opt. Express, 2007. 15(25): p. 16500-16505.
120. Sun, K.-X., et al., Balanced heterodyne signal extraction in a postmodulated Sagnac interferometer at low frequency. Opt. Lett., 1997. 22(19): p. 1485-1487.
121. M. R. Amersfoort, J.B.D.S., H. P. LeBlanc, N. C. Andreadakis, A. Rajhel, and C. Caneau, Electron. Lett., 1996. 32.
122. S. Corzine, P.E., M. Fisher, J. Gheorma, M. Kato, V. Dominic, P. Samra, A. Nilsson, J. Rahn, I. Lyubomirsky, A. Dentai, P. Studenkov, M. Missey, D. Lambert, A. Spannagel, S. Murthy, E. Strzelecka, J. Pleumeekers, A. Chen, R. Schneider, R. Nagarajan, M. Ziari, J. Stewart, C. Joyner, F. Kish, and D. Welch, IEEE Photon. Technol. Lett., 2010. 22.
123. J. J. G. M. van der Tol, J.W.P., E. G. Metaal, Y. S. Oei, H. van Brug, and I. Moerman, Mode evolution type polarization splitter on InGaAsP/InP. IEEE Photon. Technol. Lett., 1993. 5(12): p. 1412–1414.

124. L. M. Augustin, J.J.G.M.v.d.T., R. Hanfoug, W. J. M. de Laat, M. J. E. van de Moosdijk, P. W. L. van Dijk, Y.-S. Oei, and M. K. Smit, J. Lightwave Technol., 2007. 25.
125. I. Kiyat, A.A., and N. Dagli, IEEE Photon. Technol. Lett., 2005. 17.
126. D. M. Mackie, T.J.T., and T. E. Batchman, Opt. Eng., 2001. 40.
127. J. M. Hong, H.H.R., S. R. Park, J. W. Jeong, S. G. Lee, E.-H. Lee, S.-G. Park, D. W. Woo, S. Kim, and B.-H. O, IEEE Photon. Technol. Lett., 2003. 15.
128. B.-K. Yang, S.-Y.S., and D. Zhang, IEEE Photon. Technol. Lett., 2009. 21(7).
129. Chan, S.P., et al., Single-Mode and Polarization-Independent Silicon-on-Insulator Waveguides With Small Cross Section. J. Lightwave Technol., 2005. 23(6): p. 2103.
130. Breese, M.B.H., et al., Hole transport through proton-irradiated p-type silicon wafers during electrochemical anodization. Physical Review B, 2006. 73(3): p. 035428.
131. Azimi, S., et al., Fabrication of complex curved three-dimensional silicon microstructures using ion irradiation. Journal of Micromechanics and Microengineering, 2012. 22(1): p. 015015.
132. Teo, E.J., et al., Effects of oxide formation around core circumference of silicon-on-oxidized-porous-silicon strip waveguides. Opt. Lett., 2009. 34(20): p. 3142-3144.
133. Lee, M.-C.M. and M.C. Wu, Thermal annealing in hydrogen for 3-D profile transformation on silicon-on-insulator and sidewall roughness reduction. Microelectromechanical Systems, Journal of, 2006. 15(2): p. 338-343.
134. Scheerlinck, S., et al., Flexible metal grating based optical fiber probe for photonic integrated circuits. Applied Physics Letters, 2008. 92(3): p. 031104.
135. Taillaert, D., et al., Grating Couplers for Coupling between Optical Fibers and Nanophotonic Waveguides. Japanese Journal of Applied Physics, 2006. 45(8A): p. 6071-6077.

136. Teo, E.J., et al., Fabrication of low-loss silicon-on-oxidized-porous-silicon strip waveguide using focused proton-beam irradiation. Opt. Lett., 2009. 34(5): p. 659-661.